Dissolution and Vaporization of Superheated Droplets and Capsules

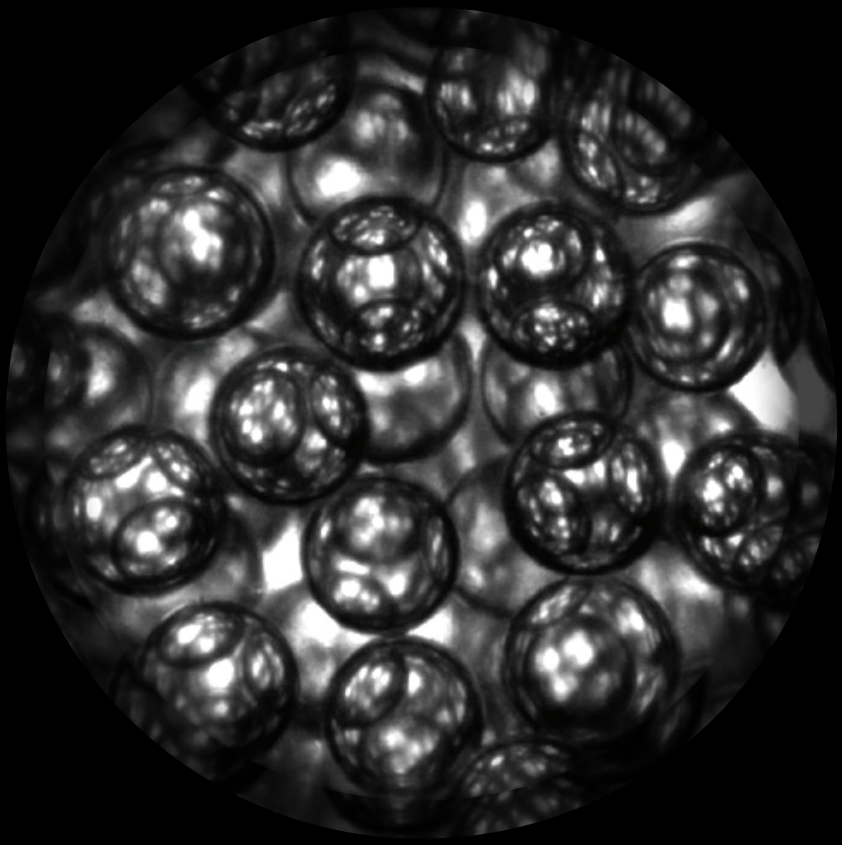

Muhammad Saeed Saleem

Dissolution and Vaporization of Superheated Droplets and Capsules

Muhammad Saeed Saleem

This dissertation has been approved by:
Promotor:
prof. dr. M. Versluis

Co-promotors:
dr. G.P.R. Lajoinie

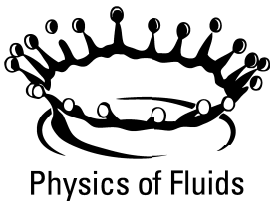

The work in this thesis was carried out at the Physics of Fluids group of the Faculty of Science and Technology of the University of Twente. This work is funded by the Dutch Research Council (NWO) grant (Veni AES 2018 - 16879) in collaboration with PPG Industries.

Dutch title:
Oplossen en Verdampen van Oververhitte Druppels en Capsules

Publisher:
Muahmmad Saeed Saleem, Physics of Fluids, University of Twente,
P.O. Box 217, 7500 AE Enschede, The Netherlands

ISBN (print): 978-90-365-6164-8
ISBN (digital): 978-90-365-6165-5
URL: https://doi.org/10.3990/1.9789036561655

Dissolution and Vaporization of Superheated Droplets and Capsules

DISSERTATION

to obtain
the degree of doctor at the University of Twente,
on the authority of the rector magnificus,
prof. dr. ir. A. Veldkamp,
on account of the decision of the Doctorate Board
to be publicly defended
on Wednesday 26 June 2024 at 14.45 hours

by

Muhammad Saeed Saleem
born on the 24th of September, 1992
in Multan, Pakistan

Graduation Committee:

Chair / secretary:	prof. dr. J.L. Herek
Promotor:	prof. dr. M. Versluis University of Twente, TNW, Physics of Fluids
	dr. G.P.R. Lajoinie University of Twente, TNW, Physics of Fluids
Committee Members	prof. dr. ir. D. Fernandez Rivas University of Twente, TNW, Mesoscale Chemical Systems
	prof. em. T.H. Van Der Meer University of Twente, ET
	prof. dr. C.E. Koning University of Groningen, Faculty of Science and Engineering
	dr. ir. H. Hofmeyer Eindhoven University of Technology, Department of the Built Environment, Chair of Applied Mechanics
	dr. S. Ma PPG Industries, PFP/Passive Fire Protection

Contents

Chapter 1

Introduction

The persistent threat of fire poses a significant danger to both humans and the surrounding infrastructure, including skyscrapers, industrial complexes, and heritage buildings. In 2021 the National Fire Protection Association of the United States [1] estimated that the fire departments responded to 1.35 million fires nationwide, leading to a devastating 3,800 civilian fatalities and 14,700 injuries. The economic impact of these incidents is estimated to amount to $ 15.9 billion in damages. To mitigate the risk, two primary types of fire protection systems are commonly employed: active and passive fire protection systems. Active systems contain well-known protection measures such as sprinklers, extinguishers, and alarms, while passive methods involve embedding fire-resistant materials in the infrastructure. Despite the measures taken in fire prevention, casualties inevitably occur due to negligence and unforeseeable events.

The blazes of the London Grenfell Tower in 2017 [4] shown in Fig. 1.1A, the fire was attributed to the flammable cladding used in the building and its design, which facilitated the rapid spread of the fire along its exterior. This choice of material has been motivated by a desire to reduce construction costs. Similarly, the Notre Dame fire in 2019 [5], believed to have been ignited by a cigarette or electrical short circuit, was quickly destroyed due to its wooden structure, a highly combustible material. Implementing adequate methods to contain fires is a necessity, as saving time is critical for assuring successful intervention and evacuation. Strategies aimed at containing fires involve the integration of fire-resistant materials within buildings or so-called passive fire protection measures such as cladding or coatings. These materials improve safety by effectively delaying fire damage and restricting its spread. Intumes-

Figure 1.1: A) Grenfell Tower fire (2017), image taken from [2]. B) An example of modern architecture at MyZeil in Frankfurt, Germany, featuring intumescent coating that maintains its aesthetics, image taken from [3].

cent coatings [6] are engineered to meet these conditions, by acting as thermal insulators and preventing structural collapse. The coating is the most attractive option due to several characteristics including user-friendly, durable, lightweight, and aesthetic to modern architecture. Figure 1.1B demonstrates a typical modern architecture with intumescent paint.

1.1 Intumescent coating

An H-beam steel coated with intumescent material, subjected to fire, results in the subsequent expansion of the protective coating, which is depicted in Fig. 1.2A. To elaborate on the expansion process, we conducted a laboratory experiment aimed at visualizing the temporal and spatial progression of an

intumescent coating, as depicted in Fig. 1.2B. A glass slide was coated with intumescent material and subjected to heat from below using a heating plate, while the process was recorded with a camera in side view. When exposed to heat, intumescent coatings expand dramatically, increasing in volume by approximately 80 times their original volume. This expansion insulates the structure by reducing heat transfer. The stages involved in the expansion process behind the intumescent coating upon heat is shown in Fig. 1.2C. An intumescent coating comprises three major components: an acid source (e.g. ammonium polyphosphate) that releases acidic gases on decomposition, a blowing agent (e.g. melamine) that forms bubbles, and a carbon source (e.g. pentaerythritol) that forms a protective cellular char structure by reacting with released gases and blowing with bubbles [7]. This cellular structure enhances the insulation properties of the char, resembling a closed-cell foam and providing thermal protection to the underlying substrate. Concurrently, the European Union has classified melamine, the chemical responsible for creating these cellular structures, as a carcinogenic material, necessitating research into sustainable alternatives.

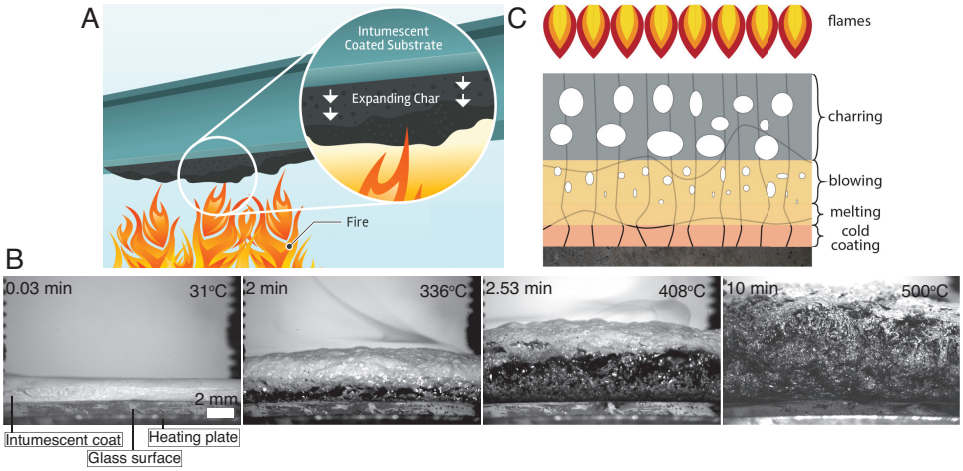

Figure 1.2: A) A steel beam coated with intumescent paint subjected to fire, causing the protective layer to expand, image taken from [8]. B) Temporal and spatial evolution of a 1 *mm* thick layer of water-based intumescent paint (STEELGUARD 701) manufactured by PPG Industries. C) The underlying process driving expansion.

Furthermore, the present technology of intumescent paint has reached its ultimate performance, exhibiting limited thermal resistance. The effectiveness of the char layer relies on its overall expansion and structural characteristics, such as porosity and homogeneity. Desired features include small cell sizes with uniform distribution within the char forming a crystalline structure. Optimal heat insulation requires a thick and homogeneous inner char structure. Therefore, the protective function of intumescence is primarily reliant on its swelling ability driven by the process of bubble generation.
These bubbles are generated in a polydisperse manner, resulting in variations in porosity throughout the structure and causing uneven heat transfer. Moreover, the inhomogeneity of the porosity leads to an irregular structure, which compromises the coating's overall strength. Zones with high porosity are more vulnerable and sensitive to collapse under minor mechanical forces. Additionally, bubble generation of different sizes can limit the overall growth of the coating. These combined factors influence the efficiency of the coating. To improve efficacy, there is a need for both, a lower heat conductivity by increasing the expansion ratio, and for an increased mechanical strength of the char structure. Furthermore, the blowing agent i.e. melamine is added to the list of carcinogenic materials by the European Union and therefore also requires research into a sustainable blowing agent.

1.2 Controlling bubble generation and challenges

Thus, ultimately improving the efficacy of these coatings necessitates controlling the bubble generation process, which drives the expansion. Figure 1.3A shows the structure of the char resulting from an uncontrolled bubble generation while with controlled bubble generation we can achieve crystalline char as sketched in Fig. 1.3B. Small and same-sized bubbles arranged in a structured pattern can reduce heat transfer by reducing the thermal conductivity that is associated with convection in large bubbles. Such configuration with crystalline bubble arrangements also supports structural stability, strengthening the char against mechanically induced damage and improving its overall strength. Moreover, a higher number of bubble layers is facilitated by systematic arrangement, leading to a high void fraction, further improving the overall expansion of the coating.
All this could be accomplished by switching from the current chemistry-based bubble generation by blowing agent to a physical approach e.g., by vaporizing small liquid precursors. Furthermore, as they vaporize, the vaporization en-

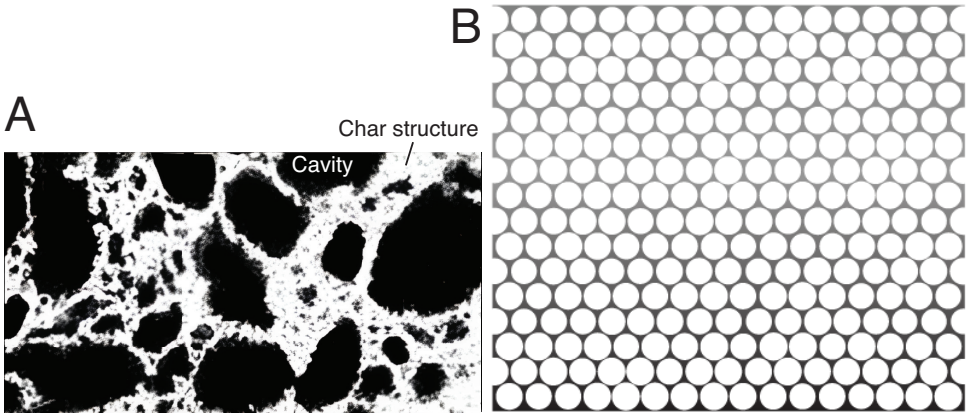

Figure 1.3: A) A cross-section of intumescent char structure with nonuniform porosity, reprinted from Ref. [9], licensed under Creative Commons CC BY. B) Concept of controlled generation of monosized bubbles.

thalpy would serve to dissipate heat, strongly reducing the heat transfer of the coating. Utilizing vaporization enthalpy as a heat sink is novel to the present concept. For stability, the precursor requires a protective polymer shell layer, i.e., a core-shell configuration known as microcapsules. The core should be of a liquid that is non-toxic, and non-flammable. A cost-effective option is water possessing a remarkable enthalpy of vaporization (2.2 MJ/kg). The shell should trigger nucleation of the core at a desired superheat. The melamine resin exhibits controlled nucleation around 300 ^oC [10], making it suitable for shell material.

In a preliminary top-down approach, we fabricated a polydisperse sample of melamine-shell and water-filled microcapsules using an in-situ polymerization method described by Sui et al. [11]. A typical microcapsule with a core-shell configuration is shown in Fig. 1.4A. These capsules were subsequently integrated into the original formulation of PPG's water-based intumescent coating, with the blowing agent (melamine) removed. A cross-section of embedded capsules is shown in Fig. 1.4B. The coating is tested similarly to that depicted in Fig. 1.2C. The images obtained from the experiments were analyzed in MATLAB; a code was employed that detects the expanding front of the coating based on a binary image thresholding algorithm. The expanding front of the coating is averaged, normalized by initial thickness, and plotted over time in Fig. 1.4C. Here, it is evident that the expansion of the new formulation

with microcapsules underperforms compared to that of the original one. The coating's opacity and the stochastic bubble generation hinder our ability to determine the behavior of the capsules within the coating. Hence, it is clear that a better understanding of the bubble generation process at the microscale is essential. A comprehensive understanding of the physical mechanisms governing bubble growth would assist in controlling the process of intumescence and enhance the insulation characteristics of the coating.

Figure 1.4: Scanning electron microscope images: A) A sliced microcapsule. B) Microcapsule embedded in the water-based intumescent coating. C) A plot of the average expanding front normalized by the initial thickness of the intumescent coat over time with different blowing agents.

1.3 A guide through the thesis

In this thesis, our focus is on investigating vapor bubble dynamics at the microscale. We simplify the system and focus on the vaporization process of a small liquid precursor within a host liquid. The second chapter of our study involves developing a model to understand the vaporization physics of a system consisting of a water droplet in oil. This model incorporates a Rayleigh-Plesset-type equation to describe bubble dynamics and incorporates thermodynamics of the phase change along with heat transfer modeled through the convection-diffusion equation. Validated with the classical boiling model, we observe that the dominant mechanism governing bubble growth varies with the size of the droplet and superheat.
In the third chapter, we experimentally study the dynamics of droplets subjected to a temperature ramp. Our findings reveal the gradual increase in temperature that leads to a drastic increase of the solubility of water in the immiscible oil phase. We establish a semi-empirical relationship based on the

Epstein-Plesset equation to quantify this effect. Additionally, we discover that the growth of vapor bubbles is limited by sheet retraction. The model was therefore adapted to incorporate the dynamic aspects of sheet retraction.
In the fourth chapter, we shield water droplets against dissolution by encapsulating them within a composite shell consisting of polylactic acid (PLA thermoplastic) and nanoparticles. We investigate the behavior of these encapsulated droplets as they are exposed to a temperature ramp. Our findings indicate that the shell effectively delays dissolution until it reaches its melting point. Afterward, dissolution is reestablished in a manner quantitatively comparable to that of an uncoated droplet. Interestingly, some capsules dissolve completely without undergoing any phase change. The resulting vapor bubble dynamics is comparable to that of the uncoated water droplets.
In the fifth chapter, we establish a microfluidic process for fabricating monodisperse water-filled microcapsules based on a melamine (thermoset) shell. This process involves a versatile microfluidic chip that can generate both single and double emulsions within the same channel and is capable of handling fluids regardless of their wetting properties. Single emulsion droplets and the encapsulating phase for double emulsions consist of curable melamine-epoxy resin, which undergoes polymerization after droplet production to form particles and capsules, respectively. We end the thesis with conclusions and a future outlook.

Chapter 2

Vaporization dynamics of a super-heated water-in-oil droplet: modeling and numerical solution [1]

The study of vapor bubble growth following droplet vaporization in a super-heated liquid involves research areas such as hydrodynamics, heat transfer, mass transfer, and thermodynamics. The interplay between these multiscale aspects is strongly dependent on the geometry, the thermodynamic response, and the local physical properties of the system. To understand the role of each aspect of this complex mechanism we model super-heated droplet vaporization by coupling the equation of motion for bubble growth with the thermodynamics of phase change and heat transfer through the convection-diffusion equation. The semi-analytical model is validated with the analytical description for vapor bubble growth dominated either by inertia (Rayleigh) or by thermal diffusion (Plesset-Zwick), depending on droplet radius and degree of superheat. The effect of a mismatch of the thermal properties between the host liquid and the droplet is shown to be relevant only for low superheating, above which an increase in thermal diffusivity leads to a reduction in the rate of vaporization. At medium to high superheating, the droplet vaporizes completely without relying on thermal diffusion. At the point of complete

[1] Submitted as: **Muhammad Saeed Saleem**, Michel Versluis, and Guillaume Lajoinie, *Vaporization dynamics of a super-heated water-in-oil droplet: modeling and numerical solution.*

vaporization, the potential energy within the system drives the bubble overshoots, which vary based on the droplet size and degree of superheat.

2.1 Introduction

In the absence of pre-existing gas nuclei, a heated droplet will enter a metastable state where the liquid temperature exceeds its boiling temperature. As temperature further increases, this metastable state ultimately breaks down and results in violent vaporization. Such superheating is commonly observed as water droplets fall into a hot oil-filled pan. There, violent vaporization caused by superheat generates a very characteristic noise and a dreaded oil splash. Industrial devices such as heat exchangers and distillation columns intentionally exploit condensation/vaporization to enhance heat transfer and phase separation. The utilization of droplets dispersed in immiscible hot fluids in a spray column heat exchanger exemplifies direct contact heat transfer, where heat is efficiently exchanged between the dispersed droplets and the hot fluid, enhancing the overall heat transfer efficiency in the system [12]. Phase separation in a distillation column occurs due to differences in boiling points where water is separated from crude oil by heating the mixture until the water superheats and separates in the form of rising vapor bubbles [13].

Two-phase systems where a vapor bubble nucleates and grows in bulk liquid or confined liquid have been well-studied through numerical simulations [14, 15], and analytical models with experimental validations [16–19]. Analytically described by the Rayleigh model [20], vaporization is initially controlled by inertia. Subsequently, thermal diffusion takes precedence, as described by the Plesset-Zwick [21] model. The recently developed semi-analytical model proposed by Chernov et al. [22] aligns well with established classical models, while accurately incorporating both growth dynamics and thermal effects. However, these models do not apply to cases where the infinite bulk medium is replaced with a droplet of finite mass immersed in an infinite immiscible medium. The presence of the host liquid affects the dynamics of the system by modifying inertia, interfacial energy, and viscous dissipation. It also affects heat transfer and limits the amount of liquid available for vaporization. Furthermore, given a spherical geometry, this impact of the host liquid depends on the initial droplet size and on time as the vapor-to-liquid ratio reduces.

Models have been devolved to approximate heat transfer coefficients. Sideman and Taitel [23] have developed an analytical model that relates the Nusselt number to the Peclet number for droplet radii within the millimeter range. In their system, the droplet vaporizes while rising due to buoyancy through a hot heat transfer fluid. Tochitani et al. [24, 25] presented a similar relation, but used the Stokes approximation instead of potential flow theory, which extends

the validity of the previous model to sub-milimeter droplets. Lajoinie et al. [26,27] have developed three-phase models to describe the vaporization of laser-heated microcapsules. These models, however, use simplified descriptions for heat transfer based on a timescale separation or a simplified thermal boundary layer. This approach may neglect various factors, including temporal and spatial dependencies, and the convective complexities, resulting in less precise representations of the associated heat transfer phenomena.

Avedisian and Suresh [28] developed a semi-analytical model to describe the vaporization process of a droplet in an infinite medium, sustained at a specific superheated temperature. It includes surface tension effects, viscous effects, the inertia of both liquids, and heat transfer. Roesle and Kulacki [29] extended the model, focusing on dynamics during and after vaporization by employing different governing equations while neglecting the viscous effects. Emery et al. [30] used conservation of mass and energy, neglecting momentum, and this simplified approach overlooks all sources of damping. The main limitation of these three models is the neglecting of acoustic re-radiation as a damping source and equating the gas temperature to boiling temperature throughout the vaporization cycle.

In existing literature, models are limited to either estimating heat transfer coefficients or applicable within specific size and temperature ranges. Consequently, they tend to overlook the role of momentum, thereby failing to capture rapid dynamics. In other instances, they are restricted to small sizes, neglecting certain widely recognized sources of damping. Furthermore, a crucial aspect overlooked by all of these studies is the incorporation of convection due to vaporization/condensation during and after vaporization. The dynamics of vapor bubbles at the micro-scale are thus still not fully understood due to numerous divergent and nonlinear effects that do not scale correctly. This is attributed to the intricate interplay of phase change, fluid mechanics, and thermal effects. Modeling and numerically solving vapor bubble growth is essential to shed light on the dominant physical mechanisms driving the vaporization and vapor bubble dynamics as a function of the thermal properties.

In this work, we aim to develop a model to systematically study the influence of droplet size, degree of superheat, and thermal properties on vaporization dynamics. The proposed semi-analytical model accounts for momentum and associated sources of damping i.e. viscous, surface energy, acoustics, and relates to its vapor temperature that drives the bubble by heat and mass transfer at the interface. We evaluate the gas temperature by accounting for time-dependent convective effects, heat flux, and gas pressure using Antoine's

law. In addition, we account for partially and fully vaporized droplets thus dealing with recondensation. Our numerical results show that the finite vaporizing mass together with the degree of superheat, describes the physical route governing droplet vaporization, i.e. inertia, and thermal diffusion. With a decrease in droplet size and an increase in temperature, the influence of the heat diffusion from the outer medium becomes insignificant. Additionally, both heat diffusion and enthalpy play a crucial role in determining the rate of bubble growth and thus are crucial in controlling bubble expansion. Post-vaporization dynamics are governed by potential energy retained within the system at the time of complete vaporization, and the resulting vapor bubble oscillations are dissipated through acoustic reradiation.

2.2 Bubble growth model

This section provides the main steps of the derivation and the details can be found in the appendix. A schematic of the system is shown in Fig. 2.1. It consists of a bubble of radius R_b nucleating in the center of a water droplet of radius R_d placed in oil used as a heat transfer fluid. The entire system is maintained at a homogeneous ambient temperature T_∞. Bubble dynamics in an infinite medium is described by the Rayleigh-Plesset equation [20, 31]. Here, the momentum equation must be integrated across both liquids in a fashion similar to Avedisian and Suresh [28] with the addition of an acoustic reradiation term. The resulting Rayleigh Plesset-type equation then takes the following form:

$$\begin{aligned}(\ddot{R}_b R_b + 2\dot{R}_b^2)\left((\rho_o - \rho_w)\frac{R_b}{R_d} + \rho_w\right) + \frac{(\rho_w - \rho_o)\dot{R}_d^2}{2} - \frac{\rho_w \dot{R}_b^2}{2} \\ = P_g + \frac{R_b}{c_o}\dot{P}_g - P_\infty - 2\left(\frac{\sigma_{wo}}{R_d} + \frac{\sigma_w}{R_b}\right) - 4\left(\frac{\dot{R}_d}{R_d}(\mu_o - \mu_w) + \frac{\dot{R}_b}{R_b}\mu_w\right),\end{aligned} \tag{2.1}$$

where r is the radius, ρ is the density, σ is the interfacial tension, μ is the viscosity, P is the pressure, and c is the speed of sound. The subscripts b, d, w, o, g, and ∞ represent the bubble, droplet, water, oil, gas, and ambient conditions far away from the bubble (at infinity), respectively. The single and double overdots indicate the first and second time derivatives, respectively. The bubble is driven by a pressure difference between the gas core and the surrounding liquid. The vapor saturation pressure is computed using the semi-empirical Antoine law [32] that describes the liquid-vapor transition:

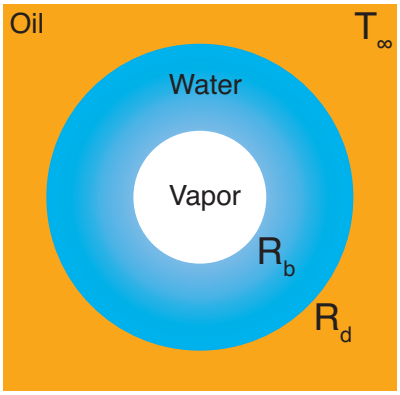

Figure 2.1: Configuration of the three-phase system of the present study. A vapor bubble of radius R_b nucleates in the center of a water droplet of radius R_d placed in oil. The system is maintained at a homogeneous temperature T_∞.

$$P_g = 10^{5+A-\frac{B}{C+T_g}}, \tag{2.2}$$

where, A, B, and C are the Antoine coefficients and T_g represents the temperature of the gas. The pressure in the bubble depends on its temperature, vapor mass, and bubble size. The bubble size is ultimately governed by the momentum conservation equation Eq. 2.1, while the mass changes through vaporization/condensation and depends on convection, specific heat of the vaporizing liquid, on the vaporization enthalpy, heat conduction across the interface, and mass available for vaporization. Taking the time derivative of the perfect gas law, eliminating the gas pressure term through Antoine's law, and considering the heat flux across the interface yields the equation that governs the evolution of the gas temperature:

$$\dot{T_g}\left[\frac{1}{T_g} - \frac{Bln(10)}{(C+T_g)^2} - \frac{C_{p_g}}{H_w}\left(1+\frac{\rho_g}{\rho_w}\right)\right] = \frac{3\dot{R}_b}{R_b} - \frac{4\pi R_b^2 k_w}{H_w m_g}\left.\frac{\partial T}{\partial r}\right|_{R_b}\left(1+\frac{\rho_g}{\rho_w}\right), \tag{2.3}$$

where, C_p is the specific heat, H is the enthalpy of vaporization, k is the thermal conductivity, m is the vaporized mass. As the bubble expands it also consumes mass at the interface through vaporization which can be expressed by writing the heat transfer across the interface:

$$\dot{m_g} = \frac{4\pi R_b^2 k_w}{H_w} \frac{\partial T}{\partial r}\bigg|_{R_b} - \frac{m_g C_{p_g} \dot{T_g}}{H_w}. \tag{2.4}$$

where, r is the spatial coordinate, T is temperature outside of bubble. When the droplet is fully vaporized, no more liquid can undergo phase change and the vapor and liquid phases no longer coexist. The vapor is then assumed to behave as an ideal gas such that:

$$\dot{P_g} = P_g\Big(\frac{\dot{T_g}}{T_g} - \frac{3\dot{R_b}}{R_b}\Big). \tag{2.5}$$

The choice of a differential form avoids the creation of an artificial discontinuity in the vapor behavior as the system transitions from a partially vaporized core to a fully vaporized one. Heat transferred to the bubble is now used only to adjust the gas temperature and its pressure through the bubble volume (see Eq. 2.5). The gas temperature is then given by:

$$\dot{T_g} = \frac{4\pi R_b^2 k_w}{C_{p_g} m_g} \frac{\partial T}{\partial r}\bigg|_{R_b}, \tag{2.6}$$

since $\dot{m_g} = 0$. The temperature outside the bubble in both cases for is determined by solving the convection-diffusion equation:

$$\dot{T}(r,t) = \frac{D}{R} \frac{\partial^2 (RT(r,t))}{\partial r^2} - \dot{R} \frac{\partial T(r,t)}{\partial r}, \tag{2.7}$$

where R corresponds to a bubble or drop. In their respective domains (water or oil) D denotes the thermal diffusivity, and r is the radial coordinate.

2.3 Numerical integration

In the vaporization regime, the momentum is governed by Eq. 2.1, and the vapor pressure is determined by Antoine's law Eq. 2.2 which requires knowing the vapor temperature. This temperature is computed using equation 2.3, and mass transfer using Eq. 2.4. The temperature profile outside of the bubble is determined by Eq. 2.7. After vaporization, Eq. 2.5 is used to calculate the vapor pressure, and the vapor temperature is computed using Eq. 2.6. This set of coupled differential equations is integrated in MATLAB using the ode 45 solver to compute the bubble radius. The convection-diffusion equation (Eq. 2.7) is solved by the method of line where the time dependency is handled by

Parameters	Initial conditions
Temperature	$T(r,0) = T_\infty$
Pressure	$P_g(0) = 10^{5+A-\frac{B}{C+T_\infty}}$,
Initial bubble	$R_b(0) = 2.5\mu m$
Bubble velocity	$\dot{R_b}(0) = 0$
Bubble mass	$m_g(0) = \frac{4}{3}\pi R_b^3(0)\frac{P_g(0)M_n}{R_i T_\infty}$
Droplet radius	$R_d(0) = (R_d(0)^3 + R_b(0)^3)^{\frac{1}{3}}$
Droplet mass	$m_w(0) = \frac{4}{3}\pi R_d^3 \rho_w$

Parameters	Boundary conditions
Droplet Radius	$R_d(t) = \left(\frac{3(m_w - mg)}{4\pi\rho_w} + R_b^3\right)^{\frac{1}{3}}$
Droplet velocity	$\dot{R_d}(t) = \frac{\dot{m_g}}{4\pi\rho_w R_d^2} + \dot{R_b}\left(\frac{R_b}{R_d}\right)^2$
Interfaces:	
Vapour-Water	$T(r = R_b, t) = T_g$
Water-Oil	$k_w \frac{\partial T}{\partial r}\big\vert_w = k_o \frac{\partial T}{\partial r}\big\vert_o$
Ambient	$T(r = r_\infty, t) = T_\infty$

Table 2.1: Initial and boundary conditions.

the solver while the spatial dependency is discretized using a re-centered finite difference scheme on the Eulerian grid. The grid vector r is defined as:

$$r = \left[0, \sum_{i=1}^{N} d_i\right], \tag{2.8}$$

where $d = (1, 2, ..., N)^{(p-1)} r_1$, $N = (\frac{r_m p}{r_1})^{1/p}$, $r_1 = 1.9 \times 10^{-21}$ m, $r_m = 0.1$ m, $p = 4$. Note that, if the pressure drops below the saturation point after full vaporization, the system can return to a partially vaporized state and resume vaporization or condensation. The initial conditions and boundary conditions are listed in Table 2.1 and values of all parameters are listed in Table 2.2. We have used octadecene (oil phase) as the heating medium. The model is solved for a range of droplet sizes (R_d) ranging from 5 to 1000 μm and degrees of superheat ($T_\infty - T_s$) ranging from 15 to 250 $^\circ C$.

Parameter	Value	Unit
Antoine coefficient A^+	5.08354	-
Antoine coefficient B^+	1663.125	-
Antoine coefficient C^+	-45.622	-
Dynamic viscosity $(\mu_w)^+$	function of temp. [33]	$Pa.s$
Dynamic viscosity $(\mu_o)^*$	function of temp. [33]	$Pa.s$
Thermal conductivity k_w^+	0.61	$W.m^{-1}.K^{-1}$
Thermal conductivity $(k_o)^*$	0.13	$W.m^{-1}.K^{-1}$
Density $(\rho_w)^+$	998	$kg.m^{-3}$
Density $(\rho_o)^*$	789	$kg.m^{-3}$
Specific heat $(C_{p_w})^+$	4216	$J.kg^{-1}.K^{-1}$
Specific heat $(C_{p_g})^\times$	2000	$J.kg^{-1}.K^{-1}$
Specific heat $(C_{p_o})^*$	2272	$J.kg^{-1}.K^{-1}$
Vaporization enthalpy $(H_w)^+$	function of temp. [33]	$J.kg^{-1}$
Surface tension $(\sigma_w)^{+\times}$	function of temp. [33]	$N.m^{-1}$
Surface tension $(\sigma_o)^*$	function of temp. [34]	$N.m^{-1}$
Interfacial tension $(\sigma_{wo})^{+*}$	$\sigma_w - \sigma_o$	$N.m^{-1}$
Atmospheric Pressure (P_∞)	101325	Pa
Speed of sound $(c_o)^*$	1067	$m.s^{-1}$
Molecular mass $(M_n)^+$	18 x 10 $^{-3}$	$kg.mol^{-1}$
Ideal gas constant (R_i)	8.314	$J.K^{-1}.mol^{-1}$
Saturation temperature (T_s)	373	K

Table 2.2: Material properties: $^+$ Water-liquid, $^\times$ Water-vapor, * Octadecene

2.4 Results

2.4.1 Model validation

To validate our model, we have compared bubble growth to analytical benchmarks describing the growth of a vapor bubble in an infinite pool of its own liquid in a free field. The system is maintained at an ambient temperature (T_∞) and atmospheric pressure (P_∞). Upon nucleation, the bubble starts to grow in an inertia-dominated regime described by the Rayleigh [20] model with $R_b \sim t$. It then transitions towards a thermal diffusion-dominated growth described by the Plesset-Zwick [21] model $R_b \sim t^{1/2}$. Mikic et al. [35] combined these two models to capture both regimes in their respective time domains:

$$R^+ = \frac{2}{3}\left[(t^+ + 1)^{3/2} - (t^+)^{3/2} - 1\right], \tag{2.9}$$

with

$$t^+ = \frac{\pi}{18}\frac{H_w(T_\infty - Ts(P_\infty))\rho_g}{T_s(P_\infty)\rho_w}\frac{t}{Ja^2 D_w}, \tag{2.10}$$

$$R^+ = \frac{\pi}{12}\sqrt{\frac{2H_w(T_\infty - Ts(P_\infty))\rho_g}{3T_s\rho_w}}\frac{R_b}{Ja^2 D_w}, \tag{2.11}$$

where $Ja = \frac{\rho_w c_{p_g}(T_\infty - Ts(P_\infty))}{\rho_g H_w}$ is the Jakob number and the subscript s rep-

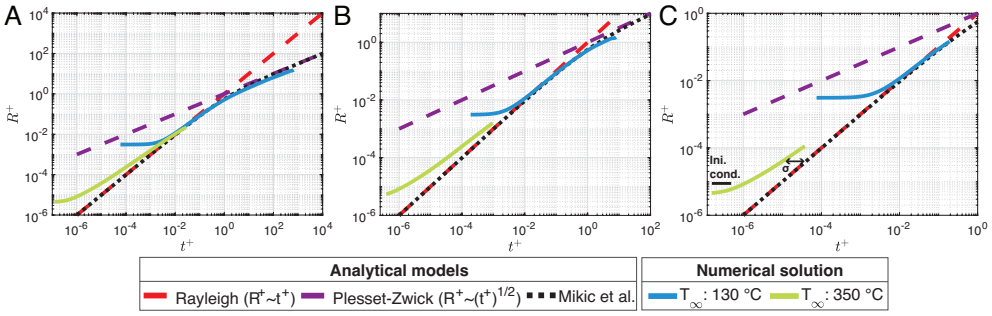

Figure 2.2: Verification of the numerical results and comparison of the proposed semi-analytical model to classic analytical models: A. R_d : 1000 μm. B. R_d : 100 μm. C. R_d : 10 μm.

resents saturation conditions. To compare our model with this classical two-phase configuration: we first consider a water droplet of radius 1 mm, (i.e., infinite with respect to the inertia and diffusive boundary layers over the simulated time-span). The drop is still theoretically immersed in oil, but its size also renders surface tension effects negligible.

The analytical result of Eq. 2.9 can be seen in Fig. 2.2 with a comparison to our model's prediction (non-dimensionalized time by Eq. 2.10 and radius by Eq. 2.11) for ambient temperatures of 130 and 350 $°C$. Our model is in excellent agreement with the analytical solutions, except for a short initial time characterized by a slow growth in the R^+ versus t^+ curves. This regime corresponds to a surface-tension-dominated growth that is not considered in the analytical models. It is also clear from Fig. 2.2 that the degree of superheat has a strong influence on the vaporization regime following the initial dynamics

dominated by surface tension: increased superheat strongly favors inertial growth.
In Fig. 2.2B and Fig. 2.2C, Eq. 2.9 and our model (plotted through Eq. 2.10) are evaluated for bubble sizes of $100\mu m$, and $10\mu m$, respectively, and ambient temperature of 130 $°C$ and 350 $°C$. The main features remain similar to the case of the 1-mm droplet, and the bubble growth still largely follows the analytical prediction even if it is evaluated beyond its area of validity i.e. for medium and small droplets. There are, however, several noteworthy consequences. First, the smaller the droplet, the more dominant inertia is: both droplets indeed vaporize almost entirely within the inertial regime. Second, the degree of superheat has a stronger influence on smaller droplets, as evidenced by the increasing separation between the blue and green curves. Finally, surface tension (not included in the analytical models) becomes important for smaller droplets, which results in a significant mismatch between the result of Eq. 2.9 and our model for high degrees of superheat.

2.4.2 Initial bubble growth

The temporal evolution of the bubble radius resulting from the vaporization of the 100 μm droplet for a range of ambient temperatures is shown in Fig. 2.3A. Initially, the growth of the nucleated bubble remains stagnant, after which it grows homogeneously inside the droplet until complete vaporization, denoted by the circle on the radius-time plot. Post-vaporization, the bubble undergoes damped oscillations with an amplitude that diminishes with a decrease in ambient temperature, as discussed in section 2.4.7. The initial growth of the bubble is governed by gas pressure and inertia:

$$\ddot{R}_b = \frac{\frac{\Delta P}{\rho_l} R_{b_0}^2 - (\dot{R}_{b_0} R_{b_0})^2}{R_{b_0}^3}, \tag{2.12}$$

where ΔP is the difference in pressure between the bubble and liquid, and the subscript 0 denotes the initial conditions. The initial velocity of the bubble is kept at zero to let the bubble expand using energy stored within the system. With $\dot{R}_{b_0} = 0$, Eq. 2.12 can be simplified to $\ddot{R}_b \sim \frac{\Delta P}{\rho_l} \frac{1}{R_{b_0}}$. The bubble is thus driven by pressure difference and maintains a constant acceleration as long as $R_b = R_{b_0}$. In Fig. 2.3B, the plot shows the evolution of the bubble wall acceleration, corresponding to the period during which initial conditions dominate bubble growth. The driving pressure can be estimated through Taylor expansion as:

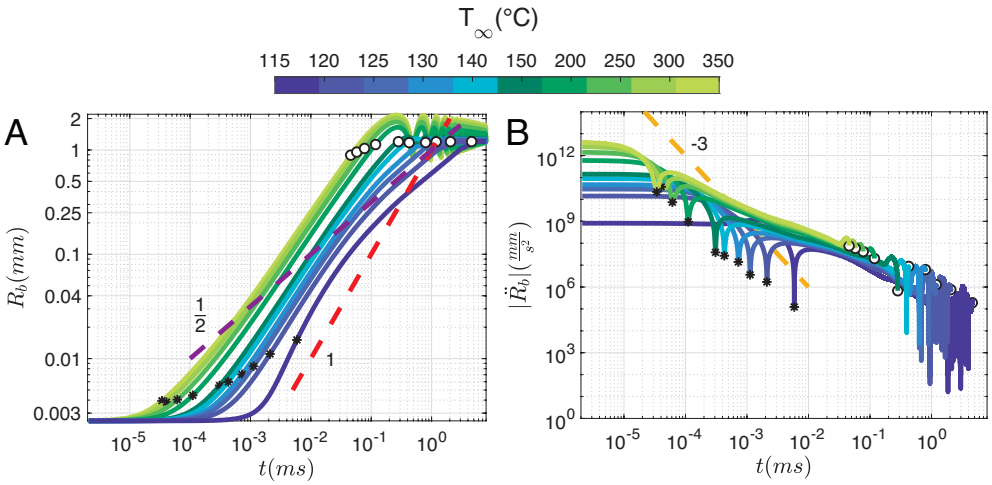

Figure 2.3: Vaporization dynamics of a 100 μm radius droplet at different ambient temperatures. Evolution of: A. bubble radius, B. bubble wall acceleration. Circles and asterisks indicate full vaporization and maximum velocity respectively.

$$\Delta P = \begin{cases} P_{sat}(T_\infty) - P_\infty, & > 10^o C \text{ superheat}, \\ (T_g - T_\infty)\frac{\partial P}{\partial T_g}(T_\infty), & \text{near boiling}. \end{cases} \tag{2.13}$$

In our simulation, we consider superheating typically exceeding $10^o C$, which drives the system through the difference between saturation pressure and ambient pressure. Integrating and substituting zero velocity in the Rayleigh-Plesset model, the initial growth follows $R_{b_0}^3 = \left(\frac{\Delta P}{\rho_l} t^2\right)^{\frac{3}{2}}$, substituted in Eq. 2.12:

$$\ddot{R}_b = \left(\frac{\rho_l}{\Delta P}\right)^{\frac{1}{2}} R_{b_0}^2 t^{-3}. \tag{2.14}$$

A short transition from the effect of initial conditions towards natural bubble growth occurs approximately around $t = R_{b_0}\sqrt{\frac{\rho_l}{\Delta P}}$, which would decrease for a higher degree of superheat. Afterward, the bubble follows either $(R \sim t)$ or $(R \sim t^{1/2})$ described by inertial or thermal growth as discussed in section 2.4.1 and shown by the dashed line in Fig. 2.3A.

2.4.3 Dominant phenomena

During vaporization heat diffuses from the surroundings towards the bubble through its thermal boundary layer, which typically follows [26]:

$$\frac{1}{\delta_{th}} = \frac{1}{\sqrt{\pi D_w t}} + \frac{1}{R_b}. \tag{2.15}$$

where δ_{th} is the thickness of the thermal boundary layer, and $\tau_{th} = \frac{R_b^2}{\pi D_w}$ denotes the corresponding time scale for the development of the boundary layer. The plot in Fig. 2.4A depicts the time scale $\frac{\tau_{th}}{t}$, where the ratio significantly exceeds one. This suggests that the entire phase change event occurs out of equilibrium, primarily due to rapid vaporization. As heat diffuses it is consumed in phase change and gas heating. The increase in the volume of gas is therefore related to both the rate of mass transfer and the rate of change in gas temperature. It could be described by the dynamic form of the ideal gas law:

$$\dot{V}_b = \frac{R_i}{M_n}\left[\dot{m}_g \frac{T_g}{P_g} + m_g \frac{\dot{T}_g}{P_g}\right]. \tag{2.16}$$

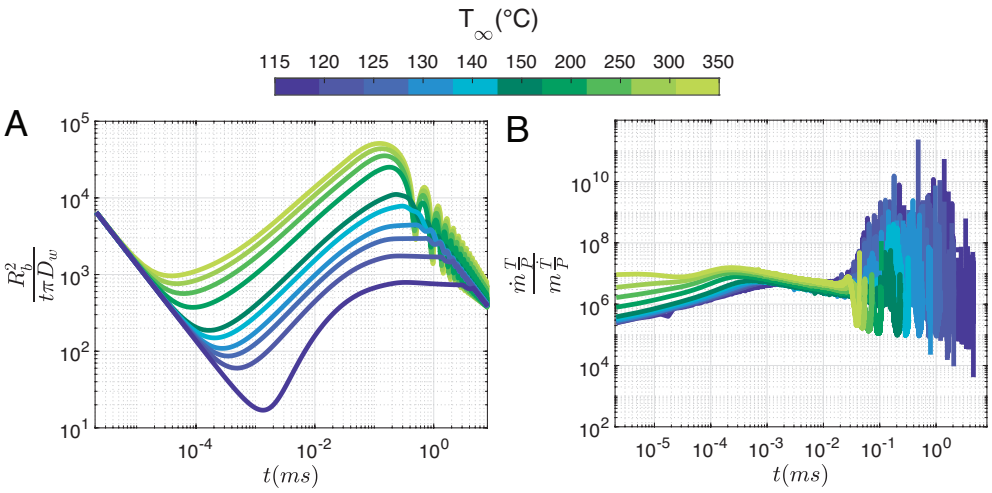

Figure 2.4: Vaporization of a 100 μm radius droplet. Evolution of: A. unsteady state of bubble growth, B. ratio of the mass transfer versus gas temperature.

The evolution of the ratio of rate in change of mass $\dot{m}_g \frac{T_g}{P_g}$ to change in temperature $m_g \frac{\dot{T}_g}{P_g}$, is plotted in Fig. 2.4B. Throughout the vaporization process, the ratio $\left(\frac{\dot{m}_g \frac{T_g}{P_g}}{m_g \frac{\dot{T}_g}{P_g}} \right)$ remains significantly larger than one indicating that the heat is almost exclusively utilized in phase change with minimal contribution to gas heating.

2.4.4 Vaporization regimes

The dominant physical mechanisms for the final growth of the bubble phase depends on droplet size and ambient temperature (see section 2.4.1). To characterize the specific physical phenomenon that governs the final stage of vaporization, we extract the time at which the droplet is fully vaporized t_f and non-dimensionalize it with, on the one hand, the characteristic heat diffusion time scale: $\tau_{thermal} = \frac{R_d^2 \rho_o c_{pw}}{k_w}$ and, on the other hand, with the inertial time scale: $\tau_{inertial} = R_{b_{(P_\infty, T_{sat})}} \sqrt{\frac{\rho_o}{P\infty}}$ where $R_{b_{(P_\infty, T_{sat})}} = \sqrt[3]{\frac{\rho_w R_d^3}{\rho_{g_{(P_\infty, T_{sat})}}}}$. The former is shown in Fig. 2.5A, and the latter in Fig. 2.5C. For reference, we also plot analytical models: the Plesset-Zwick model [21] describing thermal diffusive growth, and the Rayleigh model [20] that addresses the dominance of inertial effects.

As clarified in the previous section, these timescales are only rough estimates that help in understanding the main features. The absence of flat curves in this context results from the significant influence of ambient temperature influencing both diffusive and inertial timescales. Nonetheless, we can consider two limiting cases, the vaporization of large droplets (here 1 mm) follows the Plesset-Zwick model, and is thus dominated by diffusion for the temperature range ($115 - 250\ ^\circ C$). Second, small droplets (here 5 and 10 μm) are entirely dominated by inertia and thus follow the Rayleigh model i.e. for low and medium degrees of superheat. Using these two curves as references, it is immediately evident that droplets under study encompass some droplet sizes whose vaporization dynamics are dominated neither by diffusion nor by inertia.

This observation is further supported by the trends depicted in Fig. 2.5B and Fig. 2.5D where the vaporization enthalpy is reduced to that of pentane, which corresponds to a factor $\alpha = 6.6$ (measured in $J.kg^{-1}$). The other liquid properties are kept unchanged. Inertia becomes increasingly dominant as the vaporization enthalpy decreases and extends further to cover higher

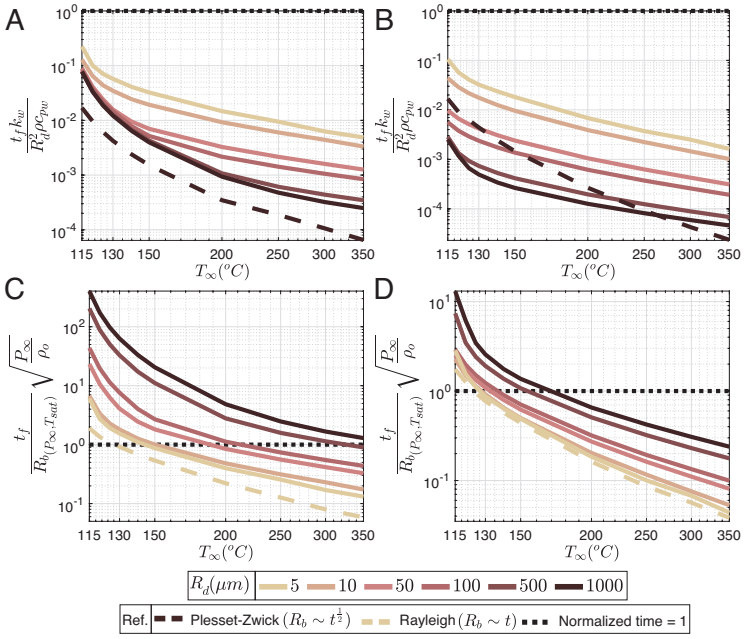

Figure 2.5: Dominant physical mechanism leading to bubble growth at the time of full vaporization t_f as a function of the bath temperature. t_f is normalized, in the top row, with the thermal-diffusion timescale, and in the bottom row, with the inertial time scale. A. and C. depict water, while the enthalpy of vaporization is reduced by a factor $\alpha = 6.6$ in B. and D. to mimic pentane. Plesset-Zwick's and Rayleigh's models solved for equivalent bubble radius for R_d of 1000 μm and 5 μm respectively, as a function of temperature.

temperatures while the thermal diffusive limit is pushed back to the low degree of superheat.

2.4.5 Influence of the thermal diffusivity of the host liquid

Thermal diffusivity influences the bubble dynamics, as vaporization relies on heat transfer from the surrounding liquid. Avedisian and Suresh [28] had proposed that the entire vaporization for a 1000 μm event splits into two stages, first during the initial bubble growth when the boundary layer is inside the droplet. In this way, thermal diffusivity and other properties of the outer liquid are of lesser importance. In the second stage, the thermal boundary layer

develops outside of the droplet in the heating fluid, and thus its diffusivity has significance in driving the bubble growth.

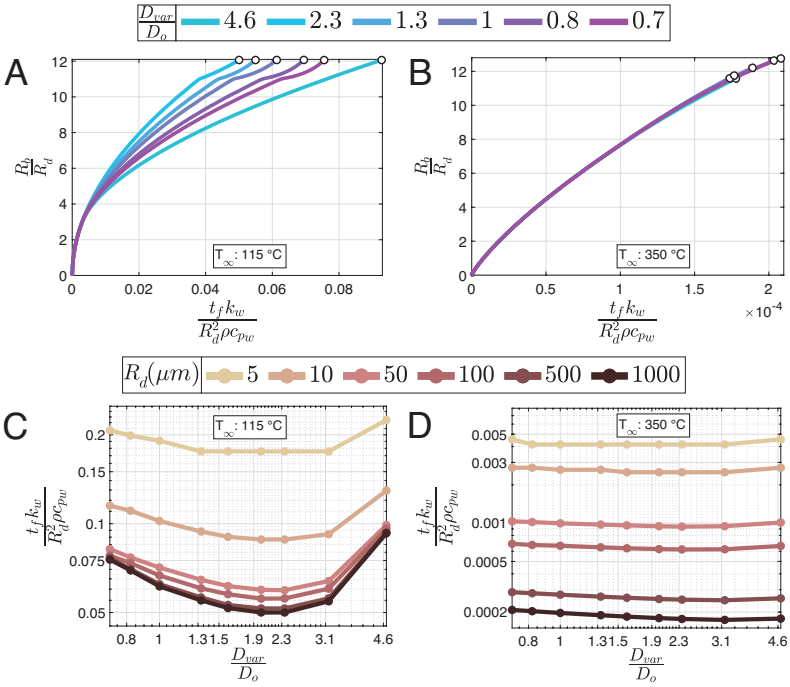

Figure 2.6: Effect of thermal diffusivity of the outer medium. Bubble growth profile of a 1000 μm radius droplet at temperatures A. 115 $°C$, B. 350 $°C$. Influence on full vaporization time across all ranges of sizes at C. 115 $°C$, D. 350 $°C$.

We have plotted the bubble growth profile until full vaporization in Fig. 2.6 (A, B) at 115 and 350 $°C$ respectively, for a 1000 μm radius droplet. These two temperatures establish the upper and lower limits of our simulations, effectively covering the entire range of dynamics. We focus on the time scale of thermal diffusion since its influence is under study here. Each figure shows the effect of varying oil diffusivity (D_{var}) non-dimensionalized by the original oil diffusivity (D_o). At 115 $°C$, two stages of growth are indeed visible in the plot: initially, all curves collapse for different diffusivity indicating no thermal influence of the outer medium. After a certain time, the curves start to diverge, highlighting the second growth stage and the dependence on the thermal properties of the outer medium. However, this is significant only

for temperatures and droplet size ranges where vaporization is dominated by thermal diffusive growth: at the upper end of our temperature range (350 $°C$) in Fig. 2.6B complete vaporization occurs within the first stage without relying on heat diffusion from outside. All growth curves collapse till complete vaporization indicating no influence of diffusion from the outer medium and validating results shown in Fig. 2.5A for the same size and temperature.
An interesting observation is that the time to reach full vaporization shows a minimum as a function of the relative diffusivity. This effect is best seen in Fig. 2.6 (C and D) showing the time of full vaporization nondimensionalized by the characteristic time of heat diffusion. The location of the minimum is $\frac{D_{var}}{D_o} \approx 2$ for low degrees of superheat while at high degrees of superheat, it is almost negligible. This indicates that at a 350 $°C$, there is enough energy stored in all size ranges of the droplet that it would vaporize fully without the necessity of acquiring heat from the outer medium. One could determine the temperature required (T') for complete droplet vaporization without depending on heat diffusion from the surrounding medium. This can be achieved through the equation $T' = \frac{H_{w(P_\infty, T_\infty)}}{C_{pw(P_\infty, T_{sat})}} + T_{sat}$, yielding values of 308 ^oC where H_w is calculated at 350 ^oC.

2.4.6 Influence of phase-change enthalpy

As seen in section 2.4.4, reducing phase change enthalpy shifts the vaporization regimes. We now explore its influence on the bubble's growth. We have scaled down the water enthalpy (H_w) by a factor $\alpha = 3.3$, 6.6, or 13.2. The value (measured in J/kg) obtained after reducing it by a factor of 6.6 corresponds to pentane, whereas the value 14 corresponds to bromoform. Most common liquids have a vaporization enthalpy ranging from 50% (e.g., pentane) to 100% of that of water. There are exceptional liquids with large molecules that have a lower enthalpy (as in the case of bromoform).
Fig. 2.7 shows the influence of reducing the phase-change enthalpy. In (A, B) we have plotted the vapor bubble radius as a function of time at a bath temperature of 115, and, 350 $°C$ respectively, for a 100 μm droplet. As phase-change enthalpy reduces, the conversion ratio from transferred heat to potential energy (i.e., vaporized mass and pressure) increases. As a result, vaporization happens much faster, and the effect is even more pronounced for low degrees of superheat. As observed in section 2.4.6, when the temperature is low the system contains relatively less stored heat, causing it to depend on heat diffusion from the surrounding environment. A reduction in phase change enthalpy necessitates a smaller amount of heat, resulting in faster vaporization and bubble

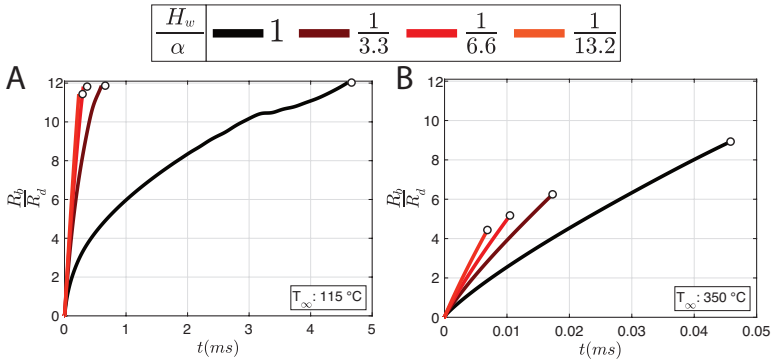

Figure 2.7: Effect of vaporization enthalpy: A - B. bubble growth at 115 and 350 $^{\circ}C$.

growth.
The influence of phase change enthalpy is not limited to vaporization and affects the post-vaporization dynamics. With lower enthalpy at a high degree of superheat (Fig. 2.7B), vaporization occurs at a smaller bubble radius. The excess energy is then utilized to raise gas pressure, leading to fast growth dynamics since no further energy is needed for phase change. This rapid expansion amplifies inertial effects, facing substantial resistance from the surrounding medium.

2.4.7 Post-vaporization damped oscillations

Once the droplet is fully vaporized, the resulting bubble overshoots its equilibrium radius $R_e^3 = \frac{3\rho_w V_{d_0} R_i T_\infty}{4\pi P_\infty M_w}$ as can be seen in Fig. 2.8A, where the bubble radius is non-dimensionalized by its equilibrium radius, and the vaporization dynamics is studied for ambient temperatures ranging from 120 ^{o}C to 350 ^{o}C. The overshoot is driven by the difference between gas pressure and ambient pressure, resulting from the potential energy available at the time of complete vaporization t_f. A decrease in temperature leads to a reduction in energy, thereby resulting in a decrease in the overshoot radius R_{max}.
At a high degree of superheat vaporization is accomplished at a radius R_{t_f} smaller than the equilibrium radius, due to the excess amount of energy in the system. For instance, vaporization of 10 μm droplet at 350 $^{\circ}C$ occurs at a radius 0.45 times smaller than its equilibrium radius as shown in Fig. 2.8B, where the radius at the time of complete vaporization is plotted for different

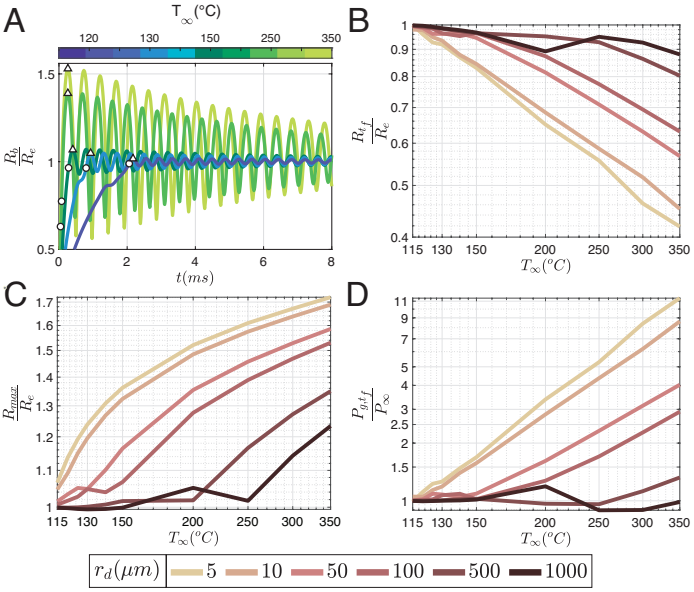

Figure 2.8: Post-vaporization dynamics. A. Time evolution of bubble oscillations non-dimensionalized by the equilibrium radius for a 100 μm radius droplet at a range of ambient temperatures. The white circles indicate the radius at full vaporization (R_{t_f}), while the white triangle indicates the maximum radius (R_{max}). For a range of ambient temperatures and droplet sizes: B. radius at the time of full vaporization non-dimensionalized by the equilibrium radius, C. maximum bubble radius non-dimensionalized by the equilibrium radius, D. gas pressure at the time of full vaporization non-dimensionalized by the ambient pressure.

droplet sizes. Here vaporization completes at a temperature well above the saturation temperature: for 10 μm at 350 $°C$ the residual pressure at complete vaporization is 8.6 times higher than the ambient pressure, thus driving the bubble after vaporization towards an overshoot of approximately 1.7 times the equilibrium radius, see Fig. 2.8 (C-D). On the other hand, for small-size droplets at a low degree of superheat, the bubble radius at full vaporization is nearly equal to the equilibrium radius with no energy to drive an overshoot and is therefore negligible.

The initial bubble expansion follows well-known damped oscillation behavior. In the model, damping has been described in terms of acoustic reradiation,

and viscous components. Assuming small radial excursion one may find the eigenfrequency (ω_o) as well as damping (ζ_{tot}) from the linearized equation of motion given as [36]:

$$\omega_o = \sqrt{\frac{3\gamma P_\infty}{\rho_o R_e^2} + (3\gamma - 1)\frac{2\sigma_o}{\rho_o R_e^3}}, \tag{2.17}$$

$$\zeta_{tot} = \frac{3\gamma P_\infty}{2\rho_o c_o R_e \omega_o} + \frac{3\gamma \sigma_o}{\rho_o c_o R_e^2 \omega_o} + \frac{2\mu_o}{\rho_o R_e^2 \omega_o}, \tag{2.18}$$

where γ indicates the polytropic exponent corresponding to 1 for our isothermal system and σ_o is the surface tension of oil. The frequency estimated from the Fourier transform of the simulated curves falls very close to resonance frequency $f_{res} = f_\circ\sqrt{1-\zeta_{tot}^2}$ estimated from the eigenfrequency in Eq. 2.17, with a damping contribution from Eq. 2.18. The frequency remains close to the well-established Minnaert frequency with a $1/R_b$ dependency. In contrast, the frequency of a vapor bubble oscillating in an infinite liquid scales as $\sim 1/R_b^{2/3}$ [37] as a consequence of gas dissolution and/or vapor condensation. In our system, we assume a pure water vapor bubble oscillating in oil, with no gas available to dissolve. Additionally, at the highest re-compression level, condensation remains absent as it necessitates releasing a significant amount of energy into a medium that is already superheated. The effect of ambient temperature on frequency can be seen by a shift of a few kiloHertz with an increase in temperature, while the shift becomes smaller with an increase in droplet radius. Equilibrium bubble sizes in our system range from 64 μm to 12 mm depending on droplet size and ambient temperature. These bubble sizes while driven acoustically are mainly dominated by sound re-radiation [38] and thus have a large contribution in Eq. 2.18 as compared to the viscous effect (third term). These findings also apply to the current system, wherein no external force is applied, and oscillations result only from a vaporization impulse (see SI Fig. 2.9).

2.5 Discussion on models comparison in literature

In literature, the closest models representing the system are those proposed by Avedisian and Suresh [28], and Emery et al. [30] that focus on droplets with a radius ranging from sub-millimeter to millimeter, and Roesle and Kulacki [29] focus on smaller droplets (with a range of 2 - 15μm). The numerical solutions employed in these studies are also different: the first two utilize Landau

immobilization, fixing the positions of moving interfaces, whereas the third implicitly solves the convection-diffusion equation to determine the temperature profile. Emery et al.'s model has limited comparability as it neglects momentum conservation. As such, it cannot capture initial rapid vaporization dynamics. Our model's findings are consistent with the predictions of Avedisian and Suresh [28] and Roesle and Kulacki [29] regarding the influence of the outer medium on vaporization, as discussed in Section 2.4.5. While these studies maintain the gas temperature at the boiling temperature throughout the simulations, the bubble growth dynamics presented here are more reliable because our model incorporates the time-dependent convective effects, gas pressure, as well as heat and mass transfer. Furthermore, our model predicts post-vaporization damped oscillations, as we also consider the acoustic damping term.

2.6 Conclusion

In this chapter, we have modeled and numerically solved the vaporization dynamics of a super-heated water droplet surrounded by an infinite oil (octadecene) medium. The droplet size as well as the degree of superheat has been varied to understand their effect on vaporization and bubble growth dynamics. For our system, it was found that the conventional two-phase analytical models (Rayleigh's and Plesset-Zwick's) are only valid for millimeter-sized droplets vaporizing at a low degree of superheat. With a decrease in droplet size and an increase in superheat, the physical mechanisms dominating bubble growth are inertia and thermal diffusion. A crucial thermal property that determines the dominant mechanism is the phase-change enthalpy. Thermal diffusivity is only important at low temperatures where vaporization relies on heat diffusion from the surrounding liquids at high temperatures as the droplet has stored enough thermal energy. Finally, bubble oscillations following complete vaporization depend on the achieved gas pressure and is influenced by the ambient temperature of the oil bath. The resonance frequency of these oscillations is close to the Minnaert frequency of a free gas bubble in an infinite medium with a $(1/R_b)$ dependency on size, unlike the oscillations of a pure vapor bubble where the resonance frequency scales with $1/R_b^{2/3}$.

Acknowledgments

This work is funded by the Dutch Research Council grant (Veni AES 2018 - 16879). G. Lajoinie acknowledges funding from the European Research Council (ERC-2022-STG Super-692 FALCON, No. 101076844).

Appendix

Theory: Model of the bubble growth

Bubble dynamics

The Navier–Stokes equations express the conservation of mass and momentum:

$$\rho(\frac{\partial \boldsymbol{v}}{\partial t} + (\boldsymbol{v}.\nabla)\boldsymbol{v}) + \nabla P = \mu \Delta \boldsymbol{v}, \tag{2.19}$$

$$\frac{\partial \rho}{\partial t} + \nabla.(\rho \boldsymbol{v}) = 0, \tag{2.20}$$

Considering the flow is symmetric ($\boldsymbol{v} = v(r)\boldsymbol{e_r}$) and incompressible ($\frac{\partial \rho}{\partial t} = 0$), with potential flow approximation ($\boldsymbol{v} = \nabla\phi$)) the above equation becomes:

$$\rho(\nabla(\dot{\phi}) + \frac{1}{2}\nabla(\nabla(\phi).\nabla(\phi)) + \nabla P = \mu\nabla(\Delta\phi). \tag{2.21}$$

Integrating equation 2.21 in both drop and accompanying outer medium:

$$\begin{cases} \rho_2 \left((\dot{\phi}_{R_2} - \dot{\phi}_{R_1}) + \frac{1}{2}(\dot{R}_2^2 - \dot{R}_1^2) \right) + P_{R_2^-} - P_{R_1^+} = 0 & \text{drop, - (a)} \\ \rho_2 \left(-\dot{\phi}_{R_2} - \frac{1}{2}\dot{R}_2^2 \right) + P_\infty - P_{R_2^+} = 0, & \text{medium. - (b)} \end{cases} \tag{2.22}$$

With spherical symmetry, the Laplacian simplifies to:

$$\Delta\phi = \frac{1}{r^2}\frac{\partial}{\partial r}(r^2\frac{\partial \phi}{\partial r}) = 0, \tag{2.23}$$

Substituting $\Delta\phi = \phi'$, and $\frac{\partial}{\partial r}(r^2\frac{\partial \phi}{\partial r}) = \alpha$:

$$\phi' = \frac{\alpha}{r^2}, \tag{2.24}$$

$$\phi = -\frac{\alpha}{r} + \beta, \tag{2.25}$$

In oil, the bubble has no long-range effect, so as $\phi \to 0$, $r \to \infty$, hence $\beta = 0$. As $\dot{R} = \phi'(R)$, $\alpha = \dot{R}R^2$. Solving incomprehensibility in both media and matching velocity at the interface:

$$\phi(r,t) = -\frac{\dot{R}_1 R_1^2}{r} = -\frac{\dot{R}_2 R_2^2}{r}, \tag{2.26}$$

$$\dot{\phi}(r) = -\frac{\ddot{R}_2 R_2^2 + 2\dot{R}_2^2 R_2}{r} = -\frac{\ddot{R}_1 R_1^2 + 2\dot{R}_1^2 R_1}{r}, \tag{2.27}$$

$$\dot{\phi}(R_1) = -\frac{R_1}{R_1}(\ddot{R}_1 R_1 + 2\dot{R}_1^2) = -\ddot{R}_1 R_1 - 2\dot{R}_1^2, \tag{2.28}$$

$$\dot{\phi}(R_2) = -\frac{\ddot{R}_2 R_2^2 + 2\dot{R}_2^2 R_2}{R_2} = -\ddot{R}_2 R_2 - 2\dot{R}_2^2 = -\frac{R_1}{R_2}(\ddot{R}_1 R_1 + 2\dot{R}_1^2). \tag{2.29}$$

The normal stress balance at second interfaces could be written as:

$$2\mu_1 \frac{\partial v}{\partial r}\bigg|_R - 2\mu_2 \frac{\partial v}{\partial r}\bigg|_R + P_{R_2^+} - P_{R_2^-} = -\delta P_{laplace}, \tag{2.30}$$

Where:

$$\delta P_{laplace} = \kappa\sigma = \frac{2\sigma_{12}}{R}, \tag{2.31}$$

$$v = \frac{\partial \phi}{\partial r} = -\frac{\partial}{\partial r}\left(\frac{\dot{R}R^2}{r}\right) = \frac{\dot{R}R^2}{r^2}, \tag{2.32}$$

$$\frac{\partial v}{\partial r}\bigg|_R = \frac{\partial \phi}{\partial r}\left(\frac{\dot{R}R^2}{r^2}\right)\bigg|_R = \frac{-2\dot{R}}{R}, \tag{2.33}$$

$$2\mu_1 \frac{\partial v}{\partial r}\bigg|_R - 2\mu_2 \frac{\partial v}{\partial r}\bigg|_R = 2\frac{\partial v}{\partial r}\bigg|_R (\mu_1 - \mu_2) = \frac{\dot{R}}{R} 4(\mu_2 - \mu_1). \tag{2.34}$$

Rewriting the normal stress balances at two interfaces:

$$\begin{cases} P_{R_1^+} = P_g - \frac{2\sigma_1}{R_1} - \frac{\dot{R}_1}{R_1} 4\mu_1, & \text{first, - (a)} \\ P_{R_2^+} = P_{R_2^-} - \frac{2\sigma_{12}}{R_2} + \frac{\dot{R}_2}{R_2} 4(\mu_1 - \mu_2), & \text{second. - (b)} \end{cases} \tag{2.35}$$

The expression for a spherical bubble expanding within a droplet, denoted as equation 2.36(a), is derived by substituting equations 2.29, 2.28, and 2.35(a) into equation 2.22(a). Similarly, the expression for the growth of the bubble from the droplet to infinity, represented as equation 2.36(b), is obtained by substituting equations 2.29 and 2.35(b) into equation 2.22(b).

$$\begin{cases} \rho_1 \left((1 - \frac{R_1}{R_2})(\ddot{R}_1 R_1 + 2\dot{R}_1^2) + \frac{\dot{R}_2^2 - \dot{R}_1^2}{2} \right) = P_g - \frac{2\sigma_1}{R_1} - \frac{\dot{R}_1}{R_1} 4\mu_1 - P_{R_2^-}, & \text{(a)} \\ \rho_2 \left(\frac{R_1}{R_2}(\ddot{R}_1 R_1 + 2\dot{R}_1^2) - \frac{\dot{R}_2{}^2}{2} \right) = P_{R_2^-} - \frac{2\sigma_{12}}{R_2} + \frac{\dot{R}_2}{R_2} 4(\mu_1 - \mu_2) - P_\infty. & \text{(b)} \end{cases} \tag{2.36}$$

Finally, the equation describing the dynamics of the bubble in two mediums is obtained by adding eq 2.36 (a) and (b):

$$\begin{aligned} &(\ddot{R}_1 R_1 + 2\dot{R}_1^2) \left(\rho_2 - \rho_1 \right) \frac{R_1}{R_2} + \rho_1 \Big) + \frac{(\rho_1 - \rho_2)\dot{R}_2^2}{2} - \frac{\rho_1 \dot{R}_1^2}{2} \\ &= P_g + \frac{R_1}{c_o} \dot{P}_g - P_\infty - 2 \left(\frac{\sigma_{12}}{R_2} + \frac{\sigma_1}{R_1} \right) - 4 \left(\frac{\dot{R}_2}{R_2} (\mu_2 - \mu_1) + \frac{\dot{R}_1}{R_1} \mu_1 \right). \end{aligned} \tag{2.37}$$

Vaporization dynamics

The pressure driving the bubble in accordance with temperature is given by semi-empirical Antoine law which relates as:

$$P_g = 10^{5 + A - \frac{B}{C + T_g}}, \tag{2.38}$$

where, $A, B, and C$ are the Antoine coefficients and T_g represents temperature of the gas. In dynamic form:

$$\frac{\dot{P}_g}{P_g} = \frac{\dot{T}_g B ln(10)}{(C + T_g)^2}. \tag{2.39}$$

During vaporization, the bubble surface and the neighboring liquid motion are influenced by the mass transfer from liquid to gas. The velocity $\dot{R}_b$ on the bubble side of the interface is higher than the velocity on the liquid side $\dot{R}_1$ by an amount that could be estimated by the rate at which mass flows per unit volume.

$$\dot{R}_1 = \dot{R}_b - \frac{\dot{m}}{4\pi R_1^2 \rho_1}, \tag{2.40}$$

$$\frac{\dot{R}_1}{R_1} = \frac{\dot{R}_b}{R_1} - \frac{\dot{m}}{3m} \frac{\rho_g}{\rho_1}, \tag{2.41}$$

The heat provided to the system is utilized in raising the gas temperature and providing phase change enthalpy:

$$4\pi K_1 R_1^2 \frac{\partial T}{\partial r}\bigg|_{R_1} = mC_{pg}\dot{T}_g + \dot{m}H_v, \tag{2.42}$$

$$\dot{m} = \frac{4\pi K_1 R_1^2}{H_v}\frac{\partial T}{\partial r}\bigg|_{R_1} - \frac{mC_{pg}\dot{T}_g}{H_v}, \tag{2.43}$$

$$\frac{\dot{m}}{m} = \frac{4\pi K_1 R_1^2}{H_v m}\frac{\partial T}{\partial r}\bigg|_{R_1} - \frac{C_{pg}\dot{T}_g}{H_v}. \tag{2.44}$$

A better estimate of gas temperature can be achieved by employing the dynamic form of the ideal gas law as the state function. This approach takes into account the variations in radius, pressure, mass, and temperature over time, providing a comprehensive understanding of how these factors evolve dynamically.

$$\frac{3\dot{R}_b}{R_b} + \frac{\dot{P}_g}{P_g} = \frac{\dot{m}}{m} + \frac{\dot{T}_g}{T_g}, \tag{2.45}$$

Where $R_b = R_1$. The equation that governs the dynamic gas temperature is finally obtained by substituting equation 2.39, 2.41, and 2.44 in 2.45:

$$\frac{\dot{T}_g}{T_g} - \frac{\dot{P}_g}{P_g} = \frac{3\dot{R}_1}{R_1} - \frac{\dot{m}}{m}\Big(1 + \frac{\rho_g}{\rho_1}\Big), \tag{2.46}$$

$$\dot{T}_g\left[\frac{1}{T_g} - \frac{Bln(10)}{(C+T_g)^2} - \frac{C_{pg}}{H_v}\Big(1+\frac{\rho_g}{\rho_1}\Big)\right] = \frac{3\dot{R}_b}{R_1} - \frac{4\pi K_1 R_1^2}{H_v m}\frac{\partial T}{\partial r}\bigg|_{R_1}\Big(1+\frac{\rho_g}{\rho_1}\Big). \tag{2.47}$$

Once the water is fully vaporized the transfer of mass $\dot{m}$ from the liquid phase to the vapor phase becomes zero and the heat is utilized only to raise the gas temperature. In this stage, the gas pressure is calculated by equation 2.45 and its temperature is calculated by

$$\dot{T}_g = \frac{4\pi K_1 R_1^2}{C_{pg} m}\frac{\partial T}{\partial r}\bigg|_{R_1}. \tag{2.48}$$

Supplementary information

Post-vaporization damped oscillations

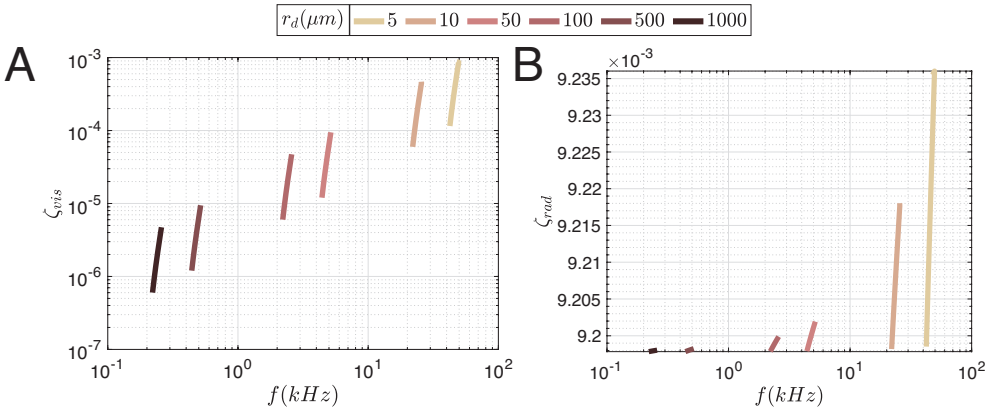

Figure 2.9: Damping coefficient of bubble oscillation as a function of frequency across different droplet sizes. A. Viscous damping, B. Acoustic damping. Increased damping for each size corresponds to the rise in ambient temperature from 115 to 350^o C.

Chapter 3

Dissolution and vaporization of a water droplet in oil exposed to a temperature ramp[1]

Vaporization of micron-sized droplets has applications in numerous technological processes including chemical reactors, oil and gas separation, and in medical imaging and therapy. Control of the vaporization for these applications requires a complete understanding of the phase-change dynamics which, in turn, requires insight into the hydrodynamic and thermodynamic processes underlying the vaporization. We utilize high-speed imaging to study the vaporization process of a water droplet in two organic media. Interestingly, a critical size exists below which droplet vaporization is prevented by droplet dissolution. The dissolution is described by a modified form of the Epstein–Plesset diffusion equation, resulting in a semi-empirical relation. Upon phase change, we show that rupture and subsequent retraction of the liquid sheet surrounding the bubble stall the vaporization, thereby limiting the growth of the vapor bubble. We compare the experimentally observed bubble growth with a numerical model based on a Rayleigh-Plesset-type equation, coupling phase change, and heat transfer through the convection-diffusion equation. Upon considering the dynamics of sheet retraction, the model shows good agreement with the

[1]Submitted as: **Muhammad Saeed Saleem**, Michel Versluis, and Guillaume Lajoinie, *Dissolution and vaporization of a water droplet in oil exposed to a temperature ramp*.

experiments.

3.1 Introduction

Droplets immersed in hot immiscible liquids can be heated far beyond their boiling point since, in the absence of free interfaces, the liquid has to overcome its tensile strength to undergo nucleation. Vaporization is consequently delayed to the so-called superheat limit which lies between the commonly known vaporization curve and the theoretical absolute limit known as the spinodal curve [39]. The exact location of the phase transition on the pressure-temperature phase diagram depends on many physical factors, including dissolved gas concentration [40], the presence of interfaces that provide interfacial energy and pressure [41], and the presence of impurities [42]. By overshooting the thermodynamic phase transition line, the considerable amount of heat that is stored in the droplet is released upon vaporization leading to violent dynamics, a phenomenon that is ubiquitous and is often very consequential. In nature, for example, contact of hot magma with underground water leads to superheating causing a phreatic eruption [37, 43]. In research, this mode of phase-change is investigated for solar-to-steam energy conversion [40], for the micro-manipulation of nano-objects [44], and to locally enhance chemical reactions. In medicine, it is used for medical imaging and therapy [26, 27, 45, 46]. Steam power plants utilize superheated steam to run turbines which in turn produce electricity [13]. In oil and gas industries, the crude mixtures of oil and gas are superheated to separate water and hydrocarbons, resulting in the formation of vapor fractions such as kerosene, and, naphtha [13]. Yet, our present physical understanding of the nucleation process and subsequent dynamics remains incomplete.

In literature, superheating has been investigated by observing the buoyant rise of a droplet in a tower filled with a thermally stratified host fluid. This experimental configuration has allowed researchers to study several aspects of the problem. Wakeshima & Takata [47] have compared experimental superheat limits of hydrocarbons to their theoretical prediction. Moore [48] investigated the formation of bubbles in superheated drops and compared experiments to the theory of homogeneous nucleation. Tochitani et al. [24] found that the heat transfer coefficient related to the interfacial area between the vaporizing drop and its host liquid increases with vaporization, while the influence of drop size and degree of superheat decreases. The separation of the droplet and vapor bubble, as a result of buoyancy, was observed, to ultimately suppress the phase change [49]. Shepherd and Sturtevant [50, 51] explored vigorous droplet vaporization and found that the rapid growth of a bubble inside the

droplet deforms its surface during the early stage of vaporization, which leads to greatly enhanced mass flux. In a configuration where the droplet rests on a surface, Van Limbeek et al. [52] have reported distinct bubble dynamics depending on the specific host liquid, which in turn is thought to primarily depend on the available interfacial energies of the various interfaces [48, 53]. With over a half-century of experimentation, literature mainly focused on measuring superheat limits, heat transfer characteristics, and nucleation aspects. However, there is a lack of understanding of the physical mechanisms that govern bubble growth and, consequently, droplet vaporization. In the present study, we combine experimentation with simulations to discover that even if sufficient heat is available, the vaporization can be hindered by the rupture and retraction of a liquid sheet surrounding the bubble. Unlike conventional boiling, the time scale of sheet retraction is dominant over the inertial or thermal diffusion timescales [21]. Here we study the vaporization of a water droplet positioned at the bottom of an oil bath. The droplet is heated by controlling the heating rate rather than placing it in a spatial temperature gradient, which thus provides better control over the heating dynamics. The temperature ramp leads to droplet dissolution, with a rate significantly larger than the typical dissolution rate described in the literature [54, 55] once the host liquid reaches the droplet boiling temperature. Vaporization is thus only observed beyond a critical size. The physical mechanisms underlying the bubble growth are studied by modeling the dynamics of sheet retraction using our earlier model of complete vaporization of the droplet, which couples bubble dynamics, phase-change, and heat transfer [56].

3.2 Material and Methods

Figure 3.1 shows the side view setup and the bottom view setup to capture the bubble dynamics. In the side view setup (Fig. 3.1A), the bottom surface of a quartz cuvette was coated with a hydrophobic Polydimethylsiloxane (PDMS 10:1) layer and placed on a heating plate. The container was filled with an organic liquid used as a heat transfer fluid and the denser water droplet rested at the bottom (contact angle $> 100^\circ$ [57]). Octadecene and oleic acid were used as heat transfer fluid and were purchased from Sigma-Aldrich and Fisher Scientific, respectively. A syringe with a 30-gauge needle was filled with ultrapure water from a Milli-Q system and jetted over a Petri dish containing heat transfer fluid resulting in a population with different droplet sizes. These droplets were transferred to the heating setup using a micropipette and the

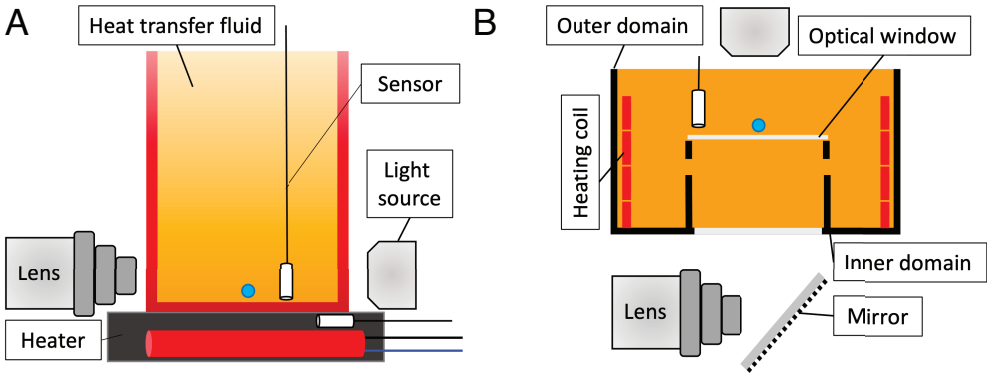

Figure 3.1: Sketch of the experimental setup: A. Side view. B. Bottom view.

host fluid was then heated from room temperature to the droplet's vaporization temperature at a rate of 0.45 °C per second.

Phase-change dynamics were captured with a high-speed camera (Photron FASTCAM SA-Z) at 30,000 frames per second (fps). The camera was connected to a Navitar 12× adjustable zoom lens providing a resolution of 17.6 μm per pixel. A SUMITA LS-M352 fiber optic light source was used for illumination. It was connected via an optical fiber and directed towards the droplet passing through a diffuser.

For the bottom view setup (Fig. 3.1B), since transparency of the side walls of the container was not required, we used a heating coil to achieve homogeneous heating. The droplet was placed on a Polydimethylsiloxane (PDMS 10:1) block placed in the center of the container. The heating rate was kept the same as that of the side view setup at 0.45 °C per second. The droplet was observed from the bottom through a glass window and its vaporization dynamics was recorded with the same camera and lens with an optical resolution of 17.6 μm per pixel, and at a frame rate of 100,000 (fps). In the same setup, dissolution dynamics was captured with a CCD camera (Lumenera LM165M), connected to the same objective lens at a frame rate of 2 fps, at a resolution of 0.45 μm per pixel.

The instantaneous droplet/bubble radius $R(t)$ is determined by image processing in MATLAB. In the bottom view, our in-house code detects and separates the bubble from the drop by a binary image thresholding algorithm. In a few cases, morphological erosion and dilation were applied in situations where separation was not achieved. This adjustment did not influence the results,

as verified by the contour plotted over the image. Assuming spherical symmetry, the radius is calculated from $R = \sqrt{\frac{A}{\pi}}$ where A is the area of the droplet/bubble extracted from the image. In the side view, we assumed cylindrical symmetry around the vertical axis (z). The area is then computed from $A = \sum_{i=1}^{I} 2\pi r_{z_i} \delta z$ where r is the distance from the axis of symmetry (z) to the bubble edge. We then calculate the equivalent radius of the hemispherical bubble as $R = \sqrt{\frac{A}{2\pi}}$.

3.3 Results

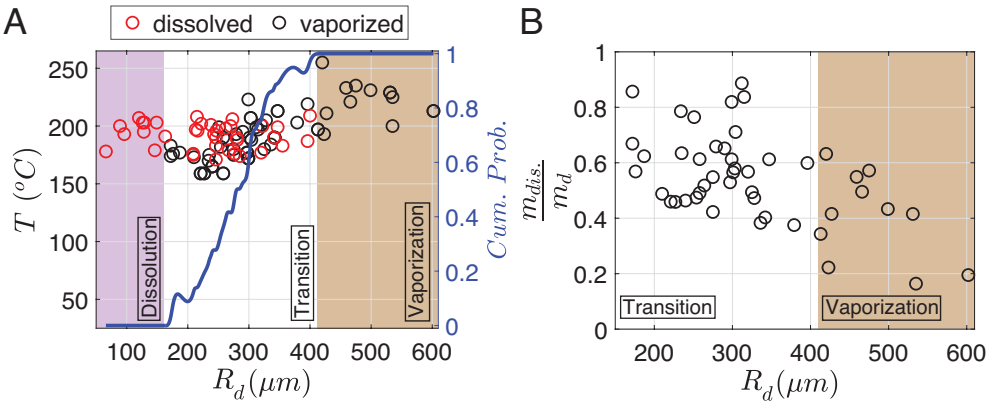

Figure 3.2: A. Phase diagram of dissolution and vaporization for different droplet sizes. Y-axis: left, indicating the measured dissolution/nucleation temperature; right, represents vaporization probability obtained by normalized cumulative sum of binary data, where 0 signifies dissolved droplets, and 1 represents vaporized ones. B. Fraction of mass dissolved before vaporization.

A water droplet immersed on a surface in an oil bath exposed to a temperature ramp can either disappear completely as it dissolves or produce bubbles as a result of the vaporization process. Fig. 3.2A shows the probability of dissolution or vaporization as a function of the temperature, divided into three areas. The pink area corresponds to droplets with a size less than 160 μm where droplets were all found to dissolve, whereas the brown region indicates droplets larger than 410 μm, representing droplets that all underwent vaporization. A transition region (white) lies between these two areas, where droplets either dissolve

or undergo a phase change.
The normalized cumulative distribution of data (blue) shows that as size increases the probability of vaporization also increases. Droplets that experience vaporization initially dissolve, resulting in a reduction in size before the nucleation process begins. Fig. 3.2B shows the mass fraction dissolved ($\frac{m_{diss}}{m_d} = \frac{R_d^3 - R_n^3}{R_d^3}$), where m_{dis} is the mass dissolved before nucleation, m_d is the initial total mass of droplet, R_n is the radius of the nucleated droplet just before nucleation as a function of the initial droplet size (R_d). The mass fraction dissolved before nucleation decreases from ~ 0.8 for $200 - 300$ μm droplets in radius up to ~ 0.2 for larger droplets. In the next two subsections, we will focus on the interplay between these competing aspects.

3.3.1 Dissolution

Dissolution is a consequence of the solubility of water in oil which has been reported for different organic media in literature [48, 49, 58]. Figure 3.3 shows an image sequence of a dissolving water droplet in octadecene, where (A) corresponds to a dissolving droplet at (constant) room temperature and (B) to a droplet exposed to a temperature ramp. The time it takes for the water droplet to fully dissolve into the oil differs by almost 2 orders of magnitude between these two cases i.e. 9.2 hours vs 8.5 minutes. Dissolution of a bubble [54] or a droplet [55] in a liquid medium at room temperature can be described by the well-known Epstein–Plesset (EP) model, $(1 - \frac{R^2}{R_d^2}) \sim \frac{t}{t_c}$, where $R(t)$ is the radius of the droplet in time t. The mass diffusion time scale is given by $t_c = \frac{\rho_w R_d^2}{2\Delta C D_w'}$, where ρ_w is the density of water, D_w' denotes the diffusion coefficient, and ΔC is the concentration difference at the droplet surface and that in the far field. In literature, data on the concentration and diffusion coefficient of water in oil is scarce, therefore t_c is not calculated explicitly.
The dissolution dynamics $R(t)$ corresponding to Figs. 3.3(A-B), is plotted in Fig. 3.3C. At room temperature (red circles), the droplet follows the scaling of the EP model (double dashed line), however, when exposed to the temperature ramp (blue & green circles) this only holds early times ($< 200s$). Fig. 3.3D shows the temporal evolution of the temperature in the bath containing the droplets. Around 200 s ($T \sim 95$ °C) the shrinkage greatly accelerates and follows a $(1 - \frac{R^2}{R_d^2}) \sim t^{6.5}$ law as can be seen by the dashed line plotted in Fig. 3.3C. The line is obtained by fitting the power law $y = ax^b$, with $a = 1.45 \times 10^{-17} \pm 2.45 \times 10^{-17}$ and $b = 6.5 \pm 0.42$. The fit is determined starting

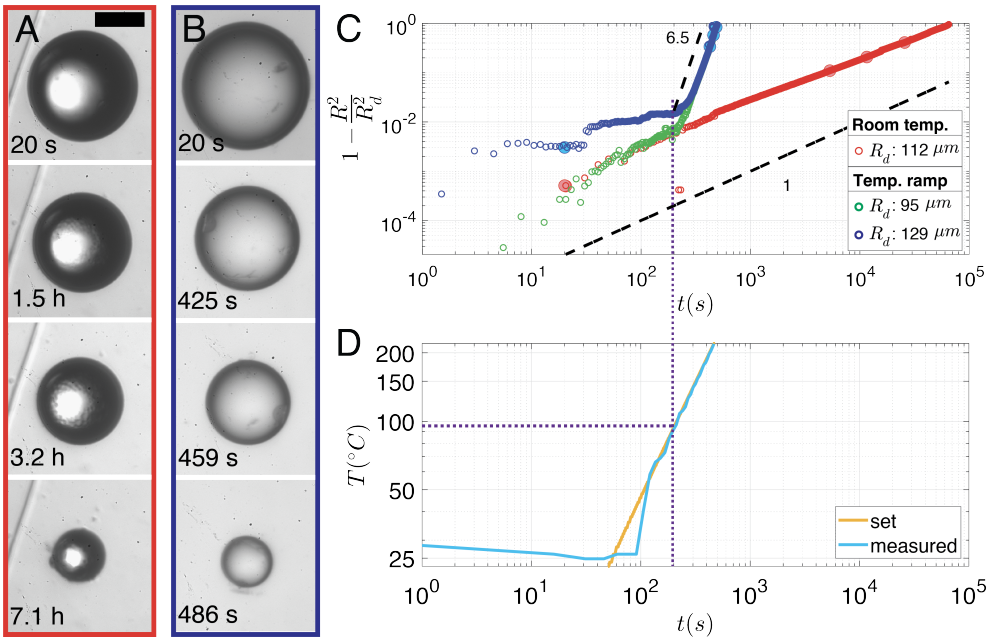

Figure 3.3: Dissolution of a water microdroplet in octadecene. Bottom view snapshots: A. Droplet at room temperature (R_d : 112 μm). B. Droplet exposed to a temperature ramp (R_d : 129 μm). C. Radius time curve of dissolved droplets, highlighted points correspond to frames in (A) and (B). D. Temperature profile of bath containing droplets exposed to 0.45 $\frac{^\circ C}{s}$ ramp. The purple dotted line relates the transition time (from power 1 to 6.5) to temperature. (scale bar: 100 μm). The white core in droplet A is from undiffused light.

at $t = 300$s and may exhibit slight variations when considering an earlier or later time.

3.3.2 Vaporization

Vaporization followed by dissolution leads to the formation of a bubble. Snapshots of a typical vaporization event for a 426 μm superheated water droplet in oleic acid is shown in Fig. 3.4A. The corresponding radius-time curve of the vaporization event is shown in Fig. 3.4B. Initially, a bubble grows from a sub-pixel size nucleus to a size of approximately five times that of the initial droplet. The vaporization dynamics are rich and consist of multiple coupled

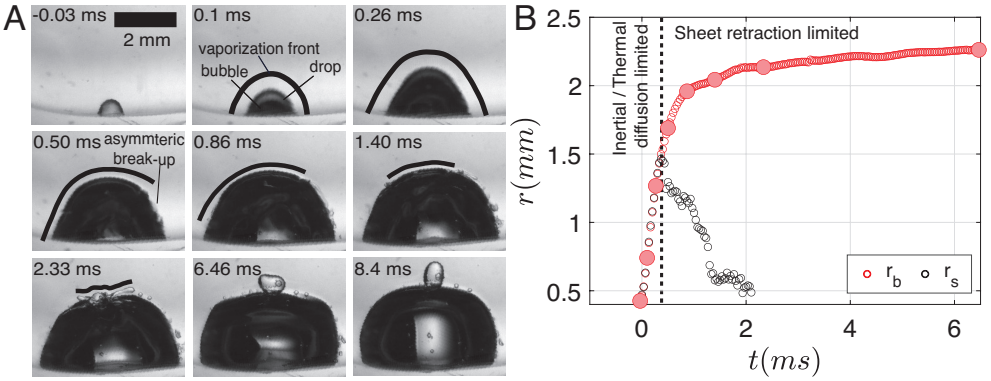

Figure 3.4: Vaporization dynamics of a superheated water droplet (R_d : 426 μm) in oleic acid nucleated at T_n : 235 $°C$: A. Side view images of the vaporization event. The vaporization front corresponds to opposing interfacial areas. B. Time evolution of bubble and sheet radius. The line splitting two regions is the dominant mechanism based on the onset of retraction. Highlighted points correspond to frames in (A).

hydrodynamic and thermodynamic events that occur simultaneously. The bubble consumes liquid at the interface by vaporization as it expands in the surrounding liquids. The phase transition is initially driven by the superheat stored in the droplet. This energy, however, rapidly decreases since the latent heat of the vaporization of water (2257 $\frac{kJ}{kg}$) exceeds the heat stored in the droplet (569 $\frac{kJ}{kg}$). Consequently while maintaining a large interfacial area, the growth is limited by inertia or thermal diffusion depending on the bubble size [56].

During the expansion process, the water is squeezed into a sheet that forms between the oil and the vapor bubble. The sheet subsequently thins both by further bubble expansion and by the consumption of its mass through vaporization. The geometry of the sheet, however, is unstable due to stretching/thinning and the sheet promptly ruptures at the contact line, then retracts under the effect of interfacial energy, leading to a reduction of the contact area between liquid and gas. This reduced surface area limits the mass transfer which, in turn, causes a drastic deceleration of the bubble expansion identified by the sheet retraction limited region (Fig. 3.4B). Once fully retracted, the sheet transforms into a droplet above the bubble surface, stalling mass transfer and thus further growth of the bubble.

3.3.3 Modelling bubble dynamics

Spherical vaporization

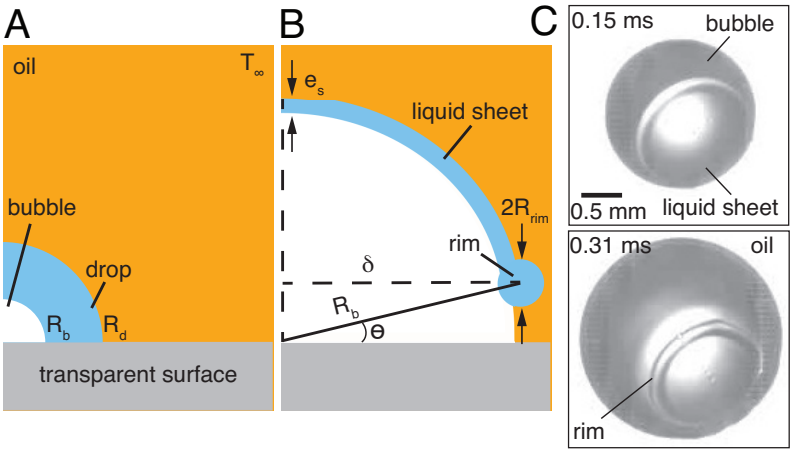

Figure 3.5: A. Sketch of nucleation, followed by bubble growth and B. sheet formation, and retraction. C. Bottom-view images, overexposed for sheet visualization.

Our system contains a bubble of radius R_b nucleating in the center of a water drop of radius R_d placed in oil used as heat transfer fluid. The entire system is kept at a homogeneous ambient temperature T_∞. A sketch of this configuration is shown in Fig. 3.5A. During vaporization, a liquid sheet of thickness e_s is formed between the bubble and the outer medium (Fig. 3.5B). When the sheet ruptures, it starts to retract collecting the liquid in a rim of radius R_{rim} as evidenced in the bottom view snapshots, see in Fig. 3.5C.

The model for the spherical vaporization of a droplet has initially been developed and numerically solved in Chapter 2. Here we will modify it to accommodate for the retraction of the sheet that leads to incomplete vaporization. Briefly, the bubble dynamics in a finite vaporizing liquid bounded by an infinite medium is governed by the momentum conservation equation given as:

$$\begin{aligned}(\ddot{R}_b R_b + 2\dot{R}_b^2)\left((\rho_o - \rho_w)\frac{R_b}{R_d} + \rho_w\right) + \frac{(\rho_w - \rho_o)\dot{R}_d^2}{2} - \frac{\rho_w \dot{R}_b^2}{2} \\ = P_g + \frac{R_b}{c_o}\dot{P}_g - P_\infty - 2\left(\frac{\sigma_{wo}}{R_d} + \frac{\sigma_w}{R_b}\right) - 4\left(\frac{\dot{R}_d}{R_d}(\mu_o - \mu_w) + \frac{\dot{R}_b}{R_b}\mu_w\right),\end{aligned} \tag{3.1}$$

where R is the radius, ρ is the density, σ is the interfacial tension, μ is the viscosity, P is the pressure, and c is the speed of sound. The subscripts b, d, w, o, g, and ∞ represent the bubble, droplet, water, oil, gas, and ambient conditions, respectively. The single and double dots indicate the first and second time derivatives, respectively. The bubble is driven by a difference in the gas pressure and the ambient pressure. The gas pressure is determined by a semi-empirical relation known as Antoine law [32] that describes the liquid-vapor transition curve at thermodynamic equilibrium in the pressure-temperature phase diagram, given as:

$$P_g = 10^{5 + A - \frac{B}{C + T_g}}, \tag{3.2}$$

where, A, B, and C are the Antoine coefficients and T_g represents the gas temperature. The driving bubble pressure is related to its temperature through the specific heat of the liquid, heat of vaporization, heat conduction across the interface, and mass available for vaporization. It is given as follows:

$$\dot{T}_g\left[\frac{1}{T_g} - \frac{B ln(10)}{(C + T_g)^2} - \frac{c_{p_g}}{H_w}\Big(1 + \frac{\rho_g}{\rho_w}\Big)\right] = \frac{3\dot{R}_b}{R_b} - \frac{A_s k_w}{H_w m_g}\frac{\partial T}{\partial r}\bigg|_{R_b}\Big(1 + \frac{\rho_g}{\rho_w}\Big), \tag{3.3}$$

where C_{p_g} is the specific heat, H is the enthalpy of vaporization, k is the thermal conductivity, m_g mass vaporized, A_s is the area where heat and mass transfer occurs between droplet and bubble. As the bubble expands it consumes mass at the interface at a rate determined by the heat flux across the interface.

$$\dot{m}_g = \frac{A_s k_w}{H_w}\frac{\partial T}{\partial r}\bigg|_{R_b} - \frac{m_g C_{p_g}\dot{T}_g}{H_w}. \tag{3.4}$$

The temperature profile outside of the bubble is determined by solving the convection-diffusion equation:

$$\dot{T}(r,t) = \frac{D}{R}\frac{\partial^2(RT(r,t))}{\partial r^2} - \dot{R}\frac{\partial T(r,t)}{\partial r}, \tag{3.5}$$

where r and D are the radial coordinate and thermal diffusivity, respectively, in their respective domain i.e. water or oil. Radius (R) corresponds to the bubble or drop.

Liquid sheet retraction model

The effective area of vaporization is given by $A_s = 2\pi R_b^2(1 - sin(\theta))$. It determines the effective region for mass transfer. Since heat changes are dominated by phase change enthalpy during vaporization and the specific heat of the gas is negligible, this area is also, de facto, the area relevant for the heat transfer. The angle of retraction θ, ranges from 0 (no retraction) to $\frac{\pi}{2}$ (fully retracted sheet). The rate of change in angle is determined as:

$$\dot{\theta} = \frac{v_s}{R_b}, \tag{3.6}$$

where v_s is the retraction velocity. Depending on the system, the retraction can be either dominated by capillary-inertial forces or capillary-viscous forces. A recent study by Sanjay et al. [59] summarizes the retraction of both a two-phase and a three-phase sheet: in two-phase retraction, the sheet is surrounded by one and the same medium while in three-phase retraction it is sandwiched between two different fluids. The scaling that describes best our water/oleic acid system could be determined by calculating the Ohnesorge number $Oh = \frac{\nu_{o(P_\infty, T_{sat})}}{\sqrt{\rho_w e_s \sigma_{wo(P_\infty, T_{sat})}}}$, where $\nu_{o_{(P_\infty, T_{sat})}} = 4\ m.Pa.s$ [60] is the viscosity of oil, $\rho_w = 998\ kg.m^{-3}$ is the density of water, $\sigma_{wo} = 31.1\ m.N.m^{-1}$ is the interfacial tension of the oil/water interface and $e_s = \frac{m_w - mg}{2\pi R_b^2 \rho_l} = 5\ \mu m$ is the sheet thickness with m_w being the initial (total) mass of droplet. Using these numbers we get $Oh \approx 0.32$.
When $Oh < 1$ in either a two-phase or a three-phase system, the retraction velocity is primarily influenced by inertial-capillary effects [59]. This behavior can be expressed using the Taylor-Culick (TC) relation: $v_s \sim \sqrt{\frac{\sigma_{wo}}{\rho_w e_s}}$. The Taylor-Culick modeling assumes a sheet of constant thickness throughout the retraction process with retracted liquid being collected in a rim dragged through the air. The rim diameter increases as the sheet retracts and therefore faces a drag in the liquid medium, unlike in air, resulting in a decrease in retraction speed. Jian et al. [61] reported another approach to model sheet

retraction that accounts for the hydrodynamic drag force on the rim formed by the retracting liquid sheet, which they applied to an air sheet contracting in a viscous surrounding. The authors demonstrate that the rim velocity decreases after reaching a maximum due to the hydrodynamic drag. The resulting expression is very similar to the Taylor-Culick velocity except that the retraction velocity is determined by the rim radius instead of the film thickness:

$$v_s = k\sqrt{\frac{\sigma_{wo}}{\rho_w R_{rim}}}, \tag{3.7}$$

where, R_{rim} is the rim radius, $k = 1/\sqrt{c_d}$ is a prefactor with c_d the drag coefficient. We estimate the radius of the rim by assuming that the liquid is collected into a perfectly symmetric toroidal rim. The detailed derivation can be found in Supplementary information 3.5 and leads to:

$$R_{rim} = \sqrt{\frac{(m_w - m_g)\tan\theta}{2\pi^2 \rho_w R_b}}, \tag{3.8}$$

3.3.4 Sheet retraction model validation

Equations 3.1, 3.3 to 3.6 are numerically solved in Matlab using the ODE 45 solver to give the radius-time relationship of the bubble $R_b(t)$. The spatial coordinate in the convection-diffusion equation (Eq. 3.5) is resolved through a re-centered finite difference scheme on the Eulerian grid using the method of lines. Supplementary information 3.5 provides the details of the numerical integration. Considering experimental uncertainty associated with the measurement of local temperature (T_n), we use temperature as a fitting parameter in all simulations represented by (T_m).

To implement the sheet retraction, we need to account for both the retraction start time and the drag coefficient c_d. The retraction start time was determined by manually tracking the sheet size frame by frame, while the overall size of the drop encapsulating the bubble was determined automatically as described in section 3.2. The ratio of the sheet to drop-encapsulated bubble surface areas is plotted by red circles for three cases in Fig. 3.6. Fig. 3.6A shows axis-symmetric retraction triggered by sheet rupture (see also Fig. 3.4), Fig. 3.6B illustrates a similar case where the contact line is partially pinned while the other side of the sheet is pulled up as the bubble grows, and Fig. 3.6C depicts a case where the growth is symmetric and forms a spherical cap. Initially, the area ratio remains constant at 1, followed by a sudden fall indicating the onset of sheet retraction. This moment is used to determine the

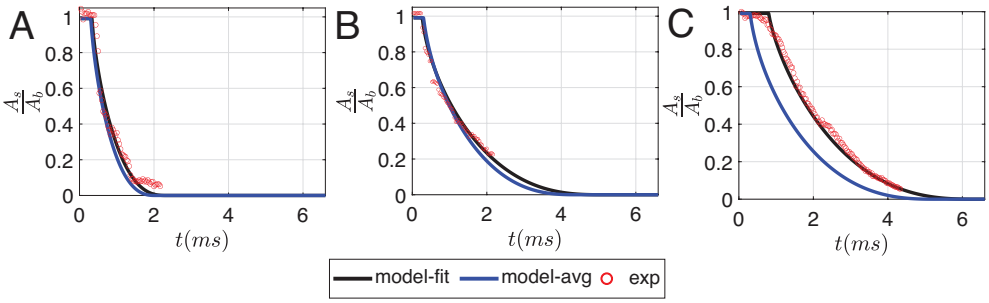

Fig. 3.6	R_d (μm)	t_{ret} (ms)	c_d	T_m $(°C)$
A	426	0.33	0.18	148
B	873	0.26	0.2	157
C	1093	0.8	0.12	155

Figure 3.6: The ratio of the area of the sheet to the area of the bubble for different cases in oleic acid of side-view experiments compared to simulation with parameters given in the table.

retraction start time, which is subsequently used to simulate each case of Fig. 3.6.

Estimating the drag on the expanding rim is necessary to model the retraction velocity based on the rim radius. The drag coefficient c_d depends on the shape of the rim [61] which is considered to be a torus here based on the optical images. As the sheet retracts, the liquid collects in the rim which thus thickens. The geometry of the rim is sensitive to the nucleation position; even a slight deviation from the center induces an asymmetric retraction, influencing the dynamics of the sheet. This variation, observed across different sizes and temperatures, leads us to also treat c_d as a fitting parameter. The best match is determined by employing a least squares fitting algorithm between the experimental and simulated curves (depicted in black) for each case, as shown in Figs. 3.6(A-C).

Considering the complexities involved in determining these two parameters (retraction start time and drag coefficient) for all experiments, we decided to keep them fixed for all the other simulations; c_d is set to 0.15 which is the average of the above three cases. Simultaneously, we utilized eight side-view experiments to measure retraction start time yielding an average of $t_{ret} = (0.304 \pm 0.22)$ ms. The data are given in Fig. 3.9 of supplementary information 3.5. Each of the cases of Fig. 3.6 are then simulated again with these averaged parameters,

as shown by the blue curves. The first two cases, representing the majority of experiments are mildly affected, therefore validate our approach. In the third case, where the sheet retraction occurs at a significantly delayed time, the earlier retraction results in a significant difference during bubble growth. It is important to emphasize that this mismatch arises from a retraction start time of $\sim 0.8\ ms$, which is much later than the rest of the data, as shown in Fig. 3.9.

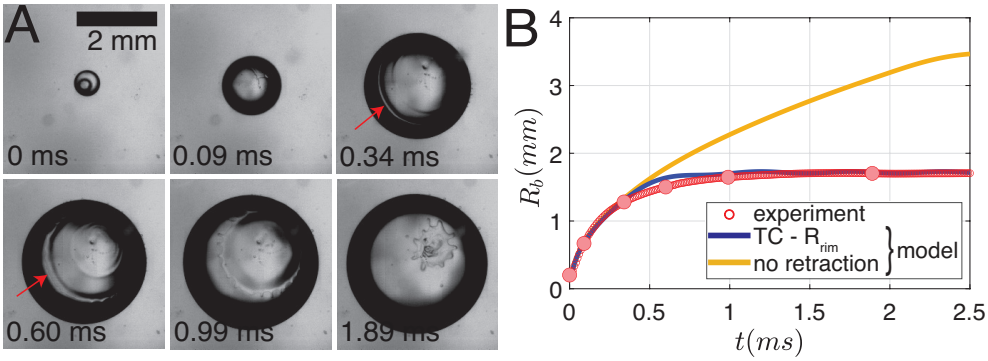

Figure 3.7: A. Bottom view images of a growing vapor bubble from a water droplet (R_d : 318 μm) in oleic acid. B. Comparison of bubble radius evolution with and without the inclusion of sheet retraction modeling, where TC is Taylor-Culick and R_{rim} is the rim radius. Highlighted markers correspond to frames in (A).

Six frames from a recording of bubble growth in oleic acid is shown in Fig. 3.7A, resulting from the vaporization of a droplet with a radius of 0.32 mm at a measured nucleation temperature $T_n = 141$ °C. The time points of these frames are depicted on the radius-time curve (red dots) shown in Fig. 3.7B. It also displays the radius-time curve obtained from the numerical solution (blue) using the average of both the retraction start time ($t_{ret} = 0.304$) and the drag coefficient ($c_d = 0.15$), providing excellent agreement for the model at all the stages of bubble growth. The model predicts rapid growth of the bubble as the vaporization area remains equal to the bubble area. Subsequently, the sheet retraction dominates, resulting in a sharp deceleration until reaching a state of no contact where the bubble expansion is slow. The model predicts a decreasing velocity due to the growth of the rim radius and accurately reproduces the experimental observations. On the contrary, if we assume no sheet

retraction in our model, the sheet will cover the entire bubble during the full vaporization, leading to sustained bubble growth (yellow curve).

3.4 Discussion

3.4.1 Effect of the location of nucleation site

Sheet retraction-dominated bubble growth discussed so far corresponds to the main phenomenon observed in our experiments. All the types of events observed are sketched in Figs. 3.8(B-C). Unlike homogeneous nucleation, where a vapor bubble can nucleate at any arbitrary location in the bulk of the liquid, heterogeneous nucleation theory predicts that interfaces will favor nucleation since the interfacial energy lowers the energy barrier for phase change. In this problem the interfaces include: the liquid-liquid (l-l) and liquid-solid (l-s) interfaces, and the liquid-solid-liquid (l-s-l) contact line, as indicated in Figs. 3.8A. The stochastic choice of a nucleation site gives rise to qualitatively different dynamics that we categorize as before [52].
Figure 3.8B shows the categories of vaporization phenomena through bottom-view setup:

- Type I ($\sim$ 48%) where sheet formation results from nucleation at the liquid-solid interface, away from the contact line. These dynamics and associated crown-shaped sheet retraction have been discussed earlier in section 3.3.2.

- Type IIa ($\sim$ 26%) where a half sheet forms as a result of nucleation occurring at the contact line and where the bubble partially grows under the droplet resulting in an asymmetric expansion. Retraction of the half sheet leads to a pinch-off phenomenon, thereby forming a single-daughter droplet (mostly) separated from the bubble.

- Type IIb($\sim$ 8%) where violent dynamics, and in some cases interfacial instability, trigger more vigorous vaporization, a phenomenon explained by baroclinic instability [62]. It was originally described for the interfacial instability of laminar flames and was later adopted for superheated vapor bubbles [50, 51]. Once a bubble has nucleated, vorticity is generated at the vaporizing front due to mass flux towards the bubble. This results in a corrugated interface, with an increased effective surface area that, in turn, increases the mass transfer. The violence of the dynamics

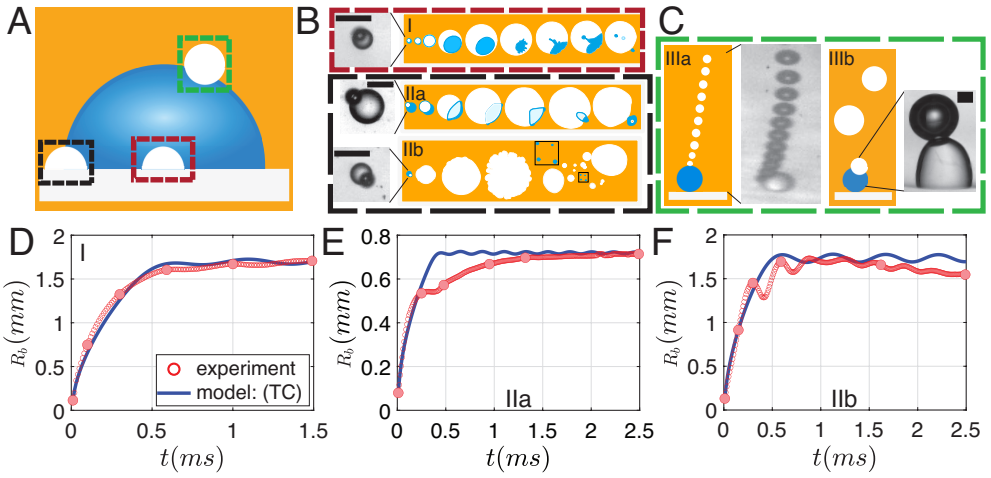

Fig. 3.8	R_d (μm)	T_m ($^\circ C$)
D	265	144
E	168	123
F	180	149

Figure 3.8: Sketch of observed vaporization dynamics: A. Nucleation location resulting in dynamical events types I-III. B. Bottom view sketch. C. Side view sketch. Comparison of events observed in octadecene with their numerical solution in (D-F), with parameters given in the table.

can subsequently lead to bubble fission through a Rayleigh-Taylor instability triggered by the acceleration towards a denser medium [37,52,62].

Figure 3.8C shows classes of vaporization phenomena shown through our side-view setup.

- **Type IIIa** (26 %) where a bubble train emerges from the droplet. Nucleation occurs at the liquid-liquid interface, and the interfacial area is limited for mass transfer. This holds especially true in a hydrophobic liquid where surface tension will favor the growth of the bubble towards the outer, non-vaporizing liquid. As the oil wets the bubble, it detaches and only leaves a small vapor pocket for the next bubble to grow leading to a rising bubble train.

- **Type IIIb** is similar to type IIIa, but results in a sparser uneven train

of larger bubbles. Additional information regarding statistics of these dynamics is provided in supplementary information 3.5.

These three nucleation phenomena have been observed in both oleic acid and octadecene. We will now compare experimental results in octadecene with the simulation. As expected for the type I event, the model is in good agreement with the experimental radius-time curve (Fig. 3.8D). In type II, the drop partially covers the growing bubble before pinch-off. It first results in less vaporized volume in the inertial or thermal diffusion limited region (Fig. 3.8E), and then, asymmetric growth during retraction ($0.2ms < t < 1.32ms$). The model nicely captures thermal diffusive growth and its size converges to the same radius plateau. When the same nucleation site is triggered by an instability (type IIb) the vaporized volume becomes comparable to type I, as can be seen in Fig. 3.8F. The model also captures the initial growth and converges to a size that is similar to those observed in experiment. However, after the thermal diffusive growth phase ($0.3ms < t < 2.49ms$), the bubble is fragmented by instabilities leading to a larger uncertainty in our size measurement, e.g. the decrease in the bubble size in the late phase in Fig. 3.8F.

3.4.2 Study considerations

In our experimental observations, dissolution is the limiting factor for the vaporization of droplets below the transition range, i.e. smaller than 160 μm as shown in Fig. 3.2A, irrespective of the heating medium used (octadecene or oleic acid). As droplet size decreases and temperature increases, there is a higher probability of undergoing ultra-fast vaporization [26, 56], potentially reducing the influence of liquid sheet retraction. Investigating the vaporization of smaller droplets would require either a host liquid where the solubility of water is negligible at all temperatures or encapsulating the water droplet into a shell to shield it against dissolution. This would change the physical properties of the system and add a source of damping to the vaporization dynamics.
By virtue of the pinning of the droplet on the glass surface dissolution also leads to a reduction of the contact angle, analogous to the pinning during the evaporation of a sessile drop [63]. This may result in an incorrect measurement of its volume using bottom-view imaging. We have therefore used a hydrophobic Polydimethylsiloxane surface (PDMS 10:1) to maintain a large contact angle $\theta > 100°$ before vaporization, i.e. during the first $6s$. A sessile drop on a PDMS layer still shows a small reduction of the contact angle [64] during partial evaporation, and this minor effect was not further investigated

here.
The model does not consider the enhanced mass flux observed by Shepherd and Sturtevant [50,51], resulting from the corrugated interface. This accounts for approximately 8 % (Type IIb) of the observed experiments. While solving the model, we used temperature as a fitting parameter to match the fast bubble growth before sheet retraction. There is a significant scatter in the data when comparing the experimental temperature (T_n) and the fitted temperature (T_m). Although this scatter can, in principle, be attributed to experimental uncertainty on the local temperature, it remains a limitation of this work. It can also be ascribed to asymmetric sheet retraction where some part of the contact line is pinned, while the remaining portion pulls off as the bubble expands. This would lead to an overestimation of the phase-change area, introducing further uncertainty in the temperature estimate.

3.5 Conclusion

In this chapter, we have studied the dissolution and vaporization experienced by microdroplets of water placed in oil as they experience a temperature rise by a slow heating ramp. While the dissolution of droplets in oil at room temperature is relatively slow, it significantly shoots up near the boiling point. The fast shrinkage due to the temperature rise is described by a power law ($(1 - \frac{R^2}{R_d^2}) \sim t^{6.5}$). This has direct consequences on achieving superheating of small droplets, as it introduces a critical size ($> R_d : 160\ \mu m$) for droplets to nucleate and undergo a phase change. Nucleation leads to the generation of a vapor bubble with vaporization dynamics that strongly depend on the initial location of the nucleation site. We have observed that the most likely nucleation site is at the liquid-solid interface, resulting in the expansion of the vaporizing droplet into a sheet that covers the growing vapor bubble. Modeling the bubble growth revealed that the time scale of sheet retraction governs the overall vaporization dynamics in contrast to classical boiling which is dominated by heat diffusion.

Acknowledgments

M.S. Saleem acknowledges M. van Limbeek for the discussion on superheated droplet vaporization and U. Sen for the discussion on sheet retraction dynamics. The authors thank G.W. Bruggert, M. Bos, and B. Benschop for

their technical support. This work is funded by the Dutch Research Council grant (Veni AES 2018 - 16879). G. Lajoinie acknowledges funding from the European Research Council (ERC-2022-STG Super-692 FALCON, No. 101076844).

Appendix

Rim radius estimation

The initial volume of the sheet is estimated as:

$$V_s = 2\pi R_b^2 e_s, \tag{3.9}$$

where e_s is the sheet thickness, that could be estimated from the non-vaporized mass:

$$e_s = \frac{m_w - mg}{2\pi R_b^2 \rho_l}, \tag{3.10}$$

where m_w is the total mass of liquid, m_g is mass vaporized, and ρ_l is the density of the liquid. The volume of the sheet can also be estimated from the volume of the spherical cap:

$$V_{cap} = 2\pi R_b^2 (1 - sin(\theta)) e_s, \tag{3.11}$$

with θ is the angle of retraction ranging from 0 (no retraction) and $\frac{\pi}{2}$ (fully retracted sheet). The retraction of the sheet results in the formation of a liquid rim in the shape of a torus. Assuming the retracted liquid is collected in the rim we can estimate its volume by subtracting eq. 3.11 from eq. 3.9 given as:

$$V_{tor} = 2\pi R_b^2 sin(\theta) e_s. \tag{3.12}$$

The volume of the torus can also be estimated as:

$$V_{tor} = 2\pi^2 R_{rim}^2 \delta = 2\pi^2 R_{rim}^2 R_b cos(\theta), \tag{3.13}$$

where R_{rim} is the torus (rim) radius, δ is the distance from the axis of symmetry to the torus center. Balancing eq. 3.12 and eq. 3.13 and substituting sheet thickness from eq. 3.10 one may obtain rim radius as:

$$R_{rim} = \sqrt{\frac{tan(\theta)(m_w - mg)}{2\pi^2 R_b \rho_l}}. \tag{3.14}$$

Supplementary information

Retraction start time

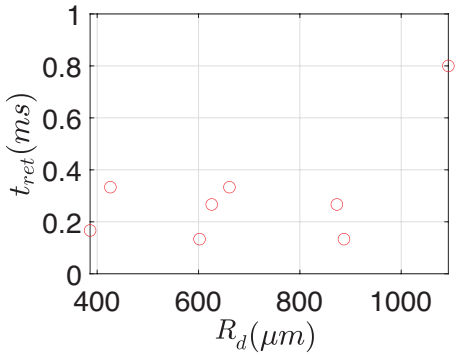

Figure 3.9: Time of sheet retraction as a function of droplet sizes for type-I dynamics measured from side view experiments.

Statistics for the types of vaporization events

In literature, the most favorable location for nucleation is credited to the specific interface with the highest interfacial tension [48, 49, 53]. However, we have observed all types of events in a single heating liquid (octadecene). The three nucleation sites were also observed in oleic acid. Nonetheless, wetting influences the observed dynamics since oleic acid displayed only types I, IIa, and IIIb with the addition of a single large bubble at the liquid-liquid interface. The likelihood of these phase-change events is independent of droplet size and nucleation temperature.

Fig. 3.10A shows the observed statistics for each type of event. Statistically, the most common event is type I, by far. This would indicate the most favorable place for nucleation is the liquid-solid interface. Type I is followed by types IIa and IIIb, which appear to have a similar likelihood. This suggests that nucleation at the contact line and liquid-liquid interface have a comparable probability. Type IIb and IIIa are the least common events. In all cases, bubble growth is hindered by a reduction of the contact area between the liquid water and its vapor.

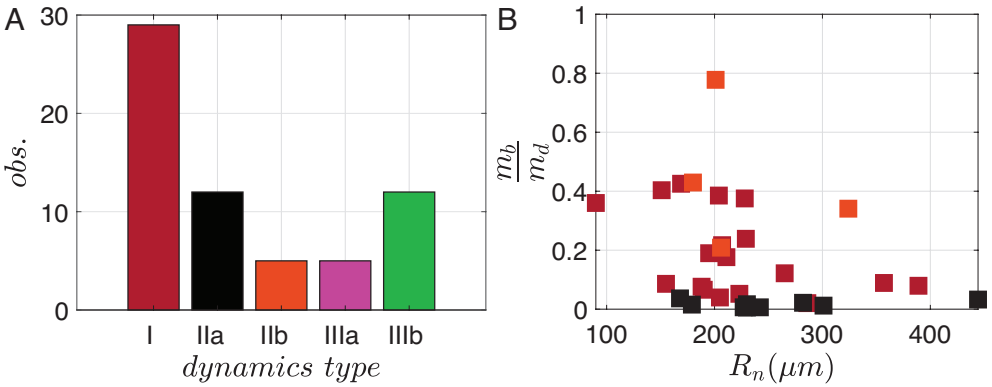

Figure 3.10: Bubble dynamics observed in octadecene. A) Statistic of observed dynamical events. B) Fraction of mass vaporized in type I, IIa, and IIb events.

Fig. 3.10B shows the fraction of mass vaporized as a function of the drop radius for types I, IIa, and IIb. The fraction of the droplet that undergoes phase change is maximum for type IIb. This result is expected since the baroclinic instability greatly enhances phase change. Type I results in smooth bubble growth compared to any other type, the bubble nucleates at or near the center of the liquid/solid interface and homogeneously from there. The transition from type I to type IIa occurs gradually and unavoidably results in some degree of subjectivity in the classification, leading to a large spread of the type I events.

Numerical scheme

The grid vector r is defined as:

$$r = \left[0, \sum_{i=1}^{N} d_i\right], \tag{3.15}$$

where $d = (1, 2, ..., N)^{(p-1)} r_1$, $N = (\frac{r_m p}{r_1})^{1/p}$, $r_1 = 1.9 \times 10^{-21}$ m, $r_m = 0.1$ m, $p = 4$. We have used temperature T_m as a fitting parameter while the corresponding experimentally measured nucleation temperature is represented by T_n. As in our experimental observation, we treat the bubble as a hemisphere.

Parameters	Initial conditions
Temperature	$T(r,0) = T_\infty$
Pressure	$P_g(0) = 10^{5+A-\frac{B}{C+T_\infty}}$,
Initial bubble	$R_b(0)$ measured exp.
Bubble velocity	$\dot{R}_b(0)$ measured exp.
Bubble mass	$m_g(0) = \frac{4}{3}\pi R_b^3(0)\frac{P_g(0)M_n}{R_i T_\infty}$
Droplet radius	$R_d(0)$ measured exp.
Droplet mass	$m_w(0) = \frac{4}{3}\pi R_d^3 \rho_w$
Parameters	**Boundary conditions**
Droplet Radius	$R_d(t) = \left(\frac{3(m_w - mg)}{4\pi\rho_w} + R_b^3\right)^{\frac{1}{3}}$
Droplet velocity	$\dot{R}_d(t) = \frac{\dot{m_g}}{4\pi\rho_w R_d^2} + \dot{R}_b\left(\frac{R_b}{R_d}\right)^2$
Interfaces:	
Vapour-Water	$T(r = R_b, t) = T_g$
Water-Oil	$k_w \frac{\partial T}{\partial r}\big\vert_w = k_o \frac{\partial T}{\partial r}\big\vert_o$
Ambient	$T(r = R_\infty, t) = T_\infty$

Table 3.1: Initial and boundary conditions.

All other initial and boundary conditions are listed in Table 1, and values of all parameters are listed in Table 2.

Parameter	Value	Unit
Antoine coefficient A^+	3.55959	-
Antoine coefficient B^+	643.748	-
Antoine coefficient C^+	-198.043	-
Dynamic viscosity $(\mu_w)^+$	function of temp. [33]	$Pa.s$
Dynamic viscosity $(\mu_o)^*$	function of temp. [33]	$Pa.s$
Dynamic viscosity $(\mu_{OA})^*$	function of temp. [60]	$Pa.s$
Thermal conductivity k_w^+	0.61	$W.m^{-1}.K^{-1}$
Thermal conductivity $(k_o)^*$	0.13	$W.m^{-1}.K^{-1}$
Thermal conductivity $(k_{OA})^*$	0.17	$W.m^{-1}.K^{-1}$
Density $(\rho_w)^+$	998	$kg.m^{-3}$
Density $(\rho_o)^*$	789	$kg.m^{-3}$
Density $(\rho_{OA})^*$	895	$kg.m^{-3}$
Specific heat $(C_{p_w})^+$	4216	$J.kg^{-1}.K^{-1}$
Specific heat $(C_{p_g})^\times$	2000	$J.kg^{-1}.K^{-1}$
Specific heat $(C_{p_o})^*$	2272	$J.kg^{-1}.K^{-1}$
Specific heat $(C_{p_{oA}})^*$	2386	$J.kg^{-1}.K^{-1}$
Vaporization enthalpy $(H_w)^+$	function of temp. [33]	$J.kg^{-1}$
Surface tension $(\sigma_o)^*$	function of temp. [34]	$N.m^{-1}$
Surface tension $(\sigma_{OA})^*$	function of temp. [65]	$N.m^{-1}$
Interfacial tension $(\sigma_{wo})^{+*}$	$\sigma_w - \sigma_o$	$N.m^{-1}$
Interfacial tension $(\sigma_{wOA})^{+*}$	$\sigma_w - \sigma_{OA}$	$N.m^{-1}$
Atmospheric Pressure (P_∞)	101325	Pa
Speed of sound $(c_o)^*$	1067	$m.s^{-1}$
Speed of sound $(c_{OA})^*$	1412	$m.s^{-1}$
Molecular mass $(M_n)^+$	18 x 10 $^{-3}$	$kg.mol^{-1}$
Ideal gas constant (R_i)	8.314	$J.K^{-1}.mol^{-1}$
Saturation temperature (T_s)	373	K

Table 3.2: Material properties: $^+$ Water-liquid, $^\times$ Water-vapor, * o: Octadecene – OA: Oleic Acid

Chapter 4

Dissolution and vaporization of a water-filled microcapsule exposed to a temperature ramp - modeling and experiments[1]

This chapter explores the dissolution and vaporization dynamics of an encapsulated water droplet in an immiscible phase. We combine both time-lapse and high-speed imaging to observe the heat-induced dynamics of capsules as they are subjected to a temperature ramp. The influence of the shell on the dynamics is quantified by comparing encapsulated and uncoated droplets. A transition region is identified where capsules undergo both dissolution and phase change. Droplets experience accelerated dissolution near their boiling point. The shell however shields the core against fast dissolution until the polymer melting point is reached, and thereafter dissolves rapidly. Here we also present an Epstein-Plesset-type model that accounts for a linear increase of the saturation concentration with temperature to describe the dissolution of both droplets and capsules. Upon nucleation, the vaporization dynamics is comparable to that of a free water droplet where it is transformed into a sheet

[1]To be submitted as: **Muhammad Saeed Saleem**, Jieke Jiang, Michel Versluis, Claas Willem Visser, and Guillaume Lajoinie, *Dissolution and vaporization of a water-filled microcapsule exposed to a temperature ramp - modeling and experiments.*

by the growing vapor bubble. Therefore, the timescale of sheet retraction governs the vaporization. However, the probability of vaporization is significantly reduced as the shell shields the capsule against external nucleation sources and limits it only to the core-shell interface. These findings hold significant implications for microcapsule stability and contribute to a deeper understanding of nucleation and its subsequent effects on the vaporization dynamics.

4.1 Introduction

Microencapsulation is a technique that encloses microdroplets within a solid shell. It has gained considerable attention for its applications in diverse industries, including pharmaceuticals, food, and cosmetics. The liquid core offers versatility, allowing for the encapsulation of a broad range of substances, including facilitating the controlled and localized release of pharmaceutical drugs in medicine [66], slow-release pesticides in agriculture while minimizing the environmental footprint [67], phase-change materials for energy storage [68], and carbon capture [69]. The shell acts as a protective barrier, shielding the core material from the surrounding liquid/gas, ensuring the stability of liquid precursors, and enables micro-manipulation.

The release of the core occurs through the process of dissolution either by diffusion through the shell matrix or by permeation through nanometric to micrometric size pores. Elastic stress buildup [70] during controlled release or excess energy storage in capsules leads to vaporization of the core. In a recent study, we discovered an uncoated microdroplet (hereafter referred to as microdroplet/droplet) of water gradually heated in an oil unfolds a sequential process of dissolution and vaporization involving both slow and ultrafast dynamics as described in Chapter 3. At room temperature, the dissolution of a water microdroplet in oil is typically described by the Epstein-Plesset model $\left(1-\frac{R^2}{R_o^2}\right) \sim t$ [54]. When exposed to a temperature ramp, the dissolution rate surpasses the expected behavior and obeys a behavior following $\left(1-\frac{R^2}{R_o^2}\right) \sim t^{6.5}$ near droplet boiling point [71]. For certain droplet sizes, dissolution is followed by phase-change resulting in the formation of a vapor bubble.

In literature, microcapsule vaporization has been explored through laser heating. Lajoinie et al. [26] investigated the vaporization dynamics induced by laser activation, revealing a sequence of vaporization/condensation cycles under continuous laser excitation. A model was developed to understand the subsequent growth and collapse of the bubble, taking into account laser-induced heat absorption of the polymeric encapsulation. In a recent study [27], both low and high boiling point cores were employed, described by two and three-phase models, respectively, with the polymeric shell serving as a heat source. Heating capsules through laser is instantaneous and localized in a medium that remains at room temperature throughout the vaporization event and as such does not encounter dissolution. Therefore, the influence of the shell on the dissolution dynamics of the core remains unexplored.

In this chapternetf, we study the influence of a polymeric shell (a composite

of polylactic acid and nanoparticles) on both the dissolution and vaporization of the encapsulated microdroplet. We employ both time-lapse and high-speed imaging techniques to study the sequential progression of microcapsule dissolution and vaporization as they are exposed to gradual heating in a bath of oleic acid. Our results show that accelerated dissolution observed for droplets near their boiling point is delayed for capsules until the polymer melting point. We develop a diffusion model that accounts for a linear increase in saturation concentration with temperature. The model is an extension of the well-known Epstein-Plesset model. We find a good correspondence between the model and experiment for the dissolution of microdroplets. The model recovers the main features of dissolution dynamics for capsules. The nucleation temperature of the microcapsules was found to be higher than that of microdroplets. This observation is attributed to the shell preventing the influence of foreign nuclei that otherwise reduce the nucleation temperature. Similarly to the case of droplets, the vaporization of a capsule is dominated by sheet retraction rather than by conventional thermal diffusion.

4.1.1 Theory of droplet dissolution

Background

The dissolution of a droplet immersed in a foreign liquid originates from diffusion into the surrounding liquid that is driven by a concentration gradient. It is described by the convection-diffusion equation, which writes:

$$\frac{\partial c}{\partial t} + \mathbf{v}.\nabla(c) = D\Delta c + p, \tag{4.1}$$

where, c (in mol/m^3) is the concentration field that is a function of space and time, $\mathbf{v}$ is the velocity field, p is a term describing the production or destruction of species, and D is the diffusion coefficient of the liquid constituting the droplet into the surrounding bath. The bold text denotes the vector field. The velocity ($\dot{R}$) of the droplet interface is then given by the mass flux across that interface induced by the local concentration gradient:

$$\dot{R} = \frac{MD}{\rho}\frac{\partial c}{\partial r}\bigg|_R, \tag{4.2}$$

where r is the radial coordinate (in the spherical coordinate system), R is the radius of the droplet, M is the molar mass of the liquid, and ρ is the density of the liquid. The dissolution process is physically equivalent (with the same

equations) to the dissolution of a gaseous bubble in a host liquid. Bubble dissolution has been investigated by Epstein and Plesset [54], and they were the first to point out that the advection was negligible. Assuming a constant gas concentration at the bubble interface, the absence of chemical reaction (i.e., $p = 0$), and neglecting the effects of surface tension, they solved these relations and proposed the well-known expression:

$$\frac{\partial R}{\partial t} = -\frac{MD\left(c_s - c_i\right)}{\rho}\left(\frac{1}{R} + \frac{1}{\sqrt{\pi D t}}\right), \tag{4.3}$$

with c_i the initial concentration in the surrounding liquid and c_s the saturation concentration in the liquid, i.e., the concentration at the bubble interface. When we consider that the diffusion timescale $\tau = \frac{R^2}{\pi D}$ is short as compared to the dissolution timescale Eq. 4.3 yields:

$$R^2 = R_o^2 - 2\frac{MD\left(c_s - c_i\right)}{\rho}t, \tag{4.4}$$

where, t is the time, and R_o is the initial bubble radius. This expression has been verified and refined multiple times since [72–74]. While the mathematical descriptions are identical for bubbles and droplets, the only difference is found in the expression of the saturation concentration c_s which in the case of the gas, depends on the ambient pressure. The result (Eq. 4.4) was also successfully applied to droplet dissolution [55, 71, 75]. Recent developments on the topic for both bubbles and droplets can be found in Lohse and Zhang [76]. The $\sqrt{t}$ dependency is only dominant at short timescale ($\tau = \frac{R^2}{\pi D}$), for which solving Eq. 4.3 yields:

$$R = R_o - 2\frac{M\left(c_s - c_i\right)}{\rho}\sqrt{\frac{Dt}{\pi}}. \tag{4.5}$$

Significance of a temperature ramp

The problem of droplet dissolution becomes more complex when the droplet is exposed to a temperature ramp since the saturation concentration of the liquid depends on temperature. There is very little data available on the saturation concentration of water in oleic acid and the only data found by the authors is that of Platford [77] that loosely suggests a linear increase of the saturation concentration with increasing temperature and we will adopt this dependency in the following. In the case of a temperature ramp, the saturation

concentration then writes:

$$c_s = c_{s_o} + \alpha a' t = c_{s_o} + \bar{a} t, \tag{4.6}$$

where, c_{s_0} is the saturation concentration at $t = 0$ (i.e., at $T = T_o$; here T_o is room temperature), α $\left(\frac{K}{s}\right)$ is the heating rate, and a' $\left(\frac{mol}{m^3 K}\right)$ is the rate of change of the saturation concentration with respect to temperature. This relation creates an unsteady boundary condition at the droplet interface, which invalidates the assumption of the traditional result from Epstein and Plesset of negligible advection [54]. To solve this problem assuming spherical symmetry while still neglecting advection, it is convenient to rewrite the diffusion equation Eq. 4.1 as:

$$\frac{\partial \tilde{c}}{\partial t} = D\Delta\tilde{c} + rp, \tag{4.7}$$

where $\tilde{c} = rc$ is the scale-invariant concentration field. This equation is now akin to a 1D cartesian equation, which is invariant to the addition of a homogeneous (i.e., independent on r) concentration field. The boundary condition at the droplet surface can then be easily applied by considering $\tilde{c}(r, t)$ as being an odd function of the translated variable $x = r - R_o$. The artificially created symmetry also allows for enforcing the unsteady boundary condition by rewriting the production/destruction term p that occurs physically at the droplet interface at $x = 0$ as destruction, that is both homogeneous and odd as a function of x:

$$\tilde{p}(x) = -\bar{a}\left(|x| + R_o\right) sign(x), \tag{4.8}$$

where, $\tilde{p}(x)$ is thus the odd translated function corresponding to $rp(r)$. Equation 4.7 can then be solved with respect to space in the Fourier domain:

$$\tilde{C}(k, t) = \tilde{C}_o(k) exp\left(-Dk^2 t\right) + \frac{\mathcal{F}\left(\tilde{p}(x)\right)}{Dk^2}\left(1 - exp\left(-Dk^2 t\right)\right), \tag{4.9}$$

here, $\mathcal{F}$ denotes the Fourier transform with respect to r, k is the wave number, and $\tilde{C}_o$ is the Fourier transform of the initial modified concentration field $\tilde{c}(x, t = 0)$ at room temperature T_o. In the symmetry considered for the resolution,

$$\tilde{c}(x, t = 0) = -\left(c_{s_o} - c_i\right)\left(|x| + R_o\right) sign(x), \tag{4.10}$$

with $c_{s_o} = c_s(t = 0)$. This particular choice for expressing $\tilde{p}(x)$ and $\tilde{c}(x, t = 0)$ provides a straightforward Fourier transforms:

$$\mathcal{F}\left(\tilde{p}(x)\right) = \frac{2jR_o\bar{a}}{k}, \tag{4.11}$$

and

$$\tilde{C_o}(k) = \frac{2jR_o\,(c_{s_o} - c_i)}{k}. \tag{4.12}$$

An inverse Fourier transform then directly gives the concentration field as a function of space and time:

$$\begin{aligned}\tilde{c}(x,t) =& - R_o\ (c_{s_o} - c_i)\ erf\left(\frac{x}{2\sqrt{Dt}}\right) \\ &-\frac{R_o\ \bar{a}}{2D}\ \left(-x^2\ sign(x) + \left(2Dt + x^2\right)\ erf\left(\frac{x}{2\sqrt{Dt}}\right) + 2\sqrt{\frac{Dt}{\pi}}\ x\ exp\left(\frac{-x^2}{4Dt}\right)\right).\end{aligned} \tag{4.13}$$

As expected, $\tilde{c}(x=0,t) = 0$ at the interface, and

$$\tilde{c}(x,t) \approx_{x>>0}\ -R_o\ (c_{s_o} - c_i + \bar{a}t)\,. \tag{4.14}$$

for $x >> 0$ far away from the droplet. The actual concentration field is then recovered by translating the modified concentration field $\tilde{c}$ (Eq. 4.13) by the artificially created offset described in Eq. 4.14, and subsequently dividing it by $r = x + R_o$ for $r >= R$:

$$\begin{aligned}c(x,t) =& - \frac{R_o\ (c_{s_o} - c_i)}{x + R_o}\ erf\left(\frac{x}{2\sqrt{Dt}}\right) \\ &-\frac{R_o\ \bar{a}}{2D}\ \left(-\frac{x^2}{x + R_o} + \frac{2Dt + x^2}{x + R_o}\ erf\left(\frac{x}{2\sqrt{Dt}}\right) + 2\sqrt{\frac{Dt}{\pi}}\ \frac{x}{x + R_o}\ exp\left(\frac{-x^2}{4Dt}\right)\right) \\ &+ \frac{R_o}{x + R_o}\,(c_{s_o} - c_i + \bar{a}t)\,.\end{aligned} \tag{4.15}$$

The concentration gradient of $c(r)$ in $r = R$ is the gradient of $c(x)$ in $x = 0$.

$$\frac{\partial c}{\partial x}(x = 0^+) = -\frac{c_{s_o} - c_i}{\sqrt{\pi Dt}} - 2\bar{a}\sqrt{\frac{t}{\pi D}} - \frac{c_{s_o} - c_i + \bar{a}t}{R_o}, \tag{4.16}$$

which directly yields the expression for the diffusion boundary layer:

$$\frac{1}{\delta} = \frac{c_{s_o} - c_i}{c_{s_o} - c_i + \bar{a}t}\ \frac{1}{\sqrt{\pi Dt}} + \frac{2\bar{a}}{c_{s_o} - c_i + \bar{a}t}\sqrt{\frac{t}{\pi D}} + \frac{1}{R_o}. \tag{4.17}$$

Note that, in the absence of heating, i.e., when $\bar{a} = 0$, the expression above reduces to:

$$\frac{1}{\delta} = \frac{1}{\sqrt{\pi D t}} + \frac{1}{R_o}, \tag{4.18}$$

which is the classical result for the diffusion from a sphere kept at constant concentration and temperature, which is the result recovered by Epstein and Plesset. Finally, Eq. 4.2 provides the ordinary differential equation obeyed by R, still in the quasi-static approximation:

$$\frac{\partial R}{\partial t} = \frac{MD}{\rho}\left(-\frac{c_{s_o} - c_i}{\sqrt{\pi D t}} - 2\bar{a}\sqrt{\frac{t}{\pi D}} - \frac{c_{s_o} - c_i + \bar{a}t}{R}\right). \tag{4.19}$$

Again considering that the diffusive timescale is short as compared to the droplet dissolution timescale:

$$R_o^2 - R^2 = \frac{2MD}{\rho}\left((c_{s_o} - c_i)t + \frac{\bar{a}t^2}{2}\right) \tag{4.20}$$

On short times, dissolution is thus dominated by the initial concentration difference $R_o^2 - R^2 \propto t$. However, on longer times, dissolution is dominated by a' $\left(\frac{mol}{m^3 K}\right)$, i.e. the rate of increase of c_s with respect to the temperature T and is faster with $R_o^2 - R^2 \propto t^2$. The transition occurs at a temperature $T_{trans} = T_o + \frac{2(c_{s_o} - c_i)}{a'}$ and at time:

$$t_{trans} = \frac{2(c_{s_o} - c_i)}{\bar{a}}. \tag{4.21}$$

Numerical integration with advection

The effects of advection and delayed temperature ramp-up (e.g., for the experimental data presented later) can be accounted for in a simple numerical scheme based on Eq. 4.9; the concentration field is first diffused over a time dt. The field is then advected using volume conservation, which provides a new concentration field to diffuse over dt. The iterative scheme then writes:

$$\tilde{C}(k, t + dt) = \tilde{C}(k, t) exp\left(-Dk^2 dt\right) + \frac{2jR_o\bar{a}}{Dk^3}\left(1 - exp\left(-Dk^2 dt\right)\right). \tag{4.22}$$

The velocity field used for advection is $v(r,t) = \frac{R^2\dot{R}}{r^2}$, with $\dot{R} = \frac{\partial R}{\partial t}$. This simple scheme converges easily in the context of droplet dissolution that displays slow and smooth dynamics. The scheme convergence was tested for the time step, wave vector range, and wave vector step. In practice, the time step dt was defined as $dt = 10^{-2}\frac{R}{|\dot{R}|}$ and with a maximum of 0.1 s to optimize speed while maintaining accuracy.

Interpretation and examples

The results from Eqs. 4.4, 4.5, 4.19, and 4.22 (iterative scheme) are plotted in Fig. 4.1 for a droplet with a radius of 220 μm. The parameters used for the simulation are $D = 2 \times 10^{-9}\ \frac{m^2}{s}$, $T_o = 293\ K$, $a' = 4.74\ \frac{mol}{m^3 K}$ [77], $C_{s_o} = 181.8\ \frac{mol}{m^3}$ [77], $\alpha = 0.4\ \frac{K}{s}$, $Mw = 18 \times 10^{-3}\ \frac{kg}{mol}$, and $\rho = 990\ \frac{kg}{m^3}$. In the absence of experimental data from the literature, D was chosen to reasonably fall in the range expected for water diffusing in organic liquids [76]. Figures 4.1(A-C) shows the dissolution dynamic of the 220 μm droplet without heating ($\bar{a} = \alpha = 0$). The short-time solution from Eq. 4.5 is, as expected, only significant over a timescale of the order of a second. The Epstein-Plesset solution from Eq. 4.4 captures the dynamics well, albeit with an overestimated dissolution time due to the initial development of the boundary layer. The solution to ODE Eq. 4.19 and the numerical solution provide nearly identical results. Figures 4.1(B-D) show the dissolution of the same droplet, now subjected to a temperature ramp. Droplet dissolution is now dramatically accelerated with a speed that far exceeds the Epstein-Plesset model. Figure 4.1D also clearly shows the transition from a linear behavior to a quadratic behavior where the vertical black lines in Figs. 4.1B and 4.1D depict the transition time point given by Eq. 4.21.

The effect of the heating rate on the dissolution timescale is shown more explicitly in Fig. 4.2. Fig. 4.2A shows the dissolution curves of the 220 μm droplet subjected to temperature ramps with varying heating rates. The heating rate, even for slow heating rapidly becomes the dominant factor in determining the dissolution time of the droplet, which decreases non-monotonically with the increasing heating rate. The classical scaling $1-\frac{R^2}{R_o^2}$ in Fig. 4.2B shows once again the expected deviation on short timescales between the dissolution curves and the Epstein-Plesset solution. On this timescale corresponding to $t \leq \frac{R_o^2}{\pi D} \approx 9$s, the heating has no strong effect and all the curves collapse. For later times, the dissolution curves show the transition from a liner to a quadratic dependency described by Eq. 4.20 occurring at a time that is inversely proportional to the heating rate, see Eq. 4.21. As a result, the linear to quadratic transition is only visible for very slow heating and disappears altogether for fast heating. Strictly speaking, this transition vanishes when the transition time becomes comparable to the diffusive timescale, i.e., $\frac{2(c_{s_o}-c_i)}{\alpha a} = \frac{R0^2}{\pi D}$. This occurs, for the present simulation parameters, for a heating rate of 10 $\frac{K}{s}$.

The dissolution time of a droplet can then be bounded by two limiting cases corresponding to slow and fast heating. If the heating rate is low, the droplet

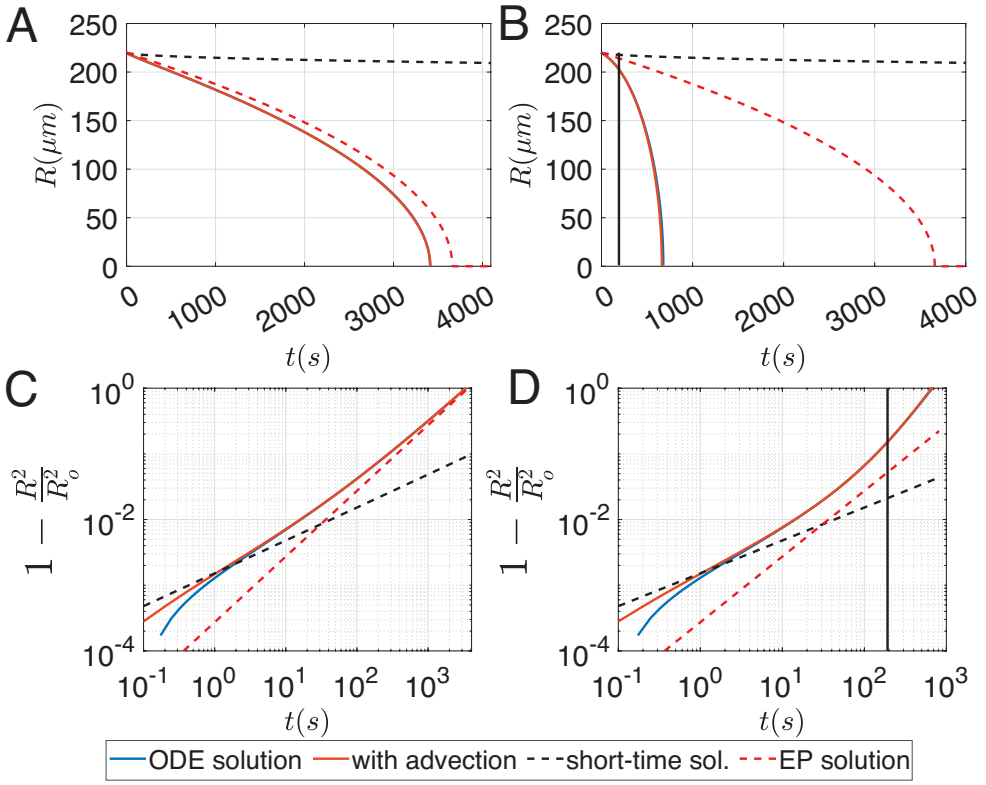

Figure 4.1: A. Dissolution dynamics of a 220 μm droplet without heating. Solutions are presented for the classical Epstein-Plesset (EP) theory, Eq. 4.4, the short-time solution, Eq. 4.5, the ODE Eq. 4.19, and the numerical solution with advection Sec. 4.1.1. B. The very same droplet when subjected to a 0.4 $\frac{K}{s}$ temperature ramp, showing a strongly increased dissolution. Dynamics in (A) and (B) are replotted using the usual Epstein-Plesset scaling in (C) and (D), respectively. The solid black line in B and D indicates the transition time point from a linear to a quadratic law and follows directly from Eq. 4.21.

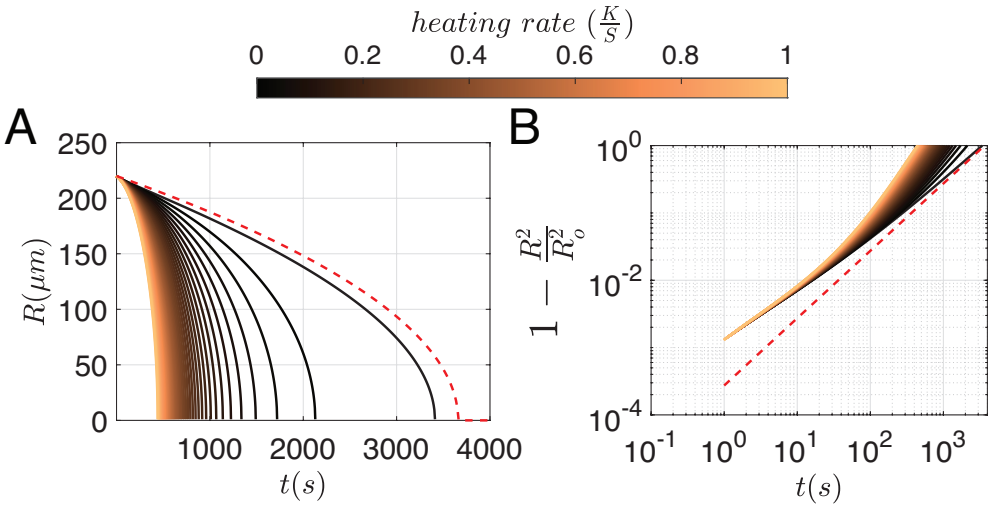

Figure 4.2: A. Dissolution dynamics of 220 μm droplet subjected to temperature ramps with varying heating rates from 0 to 1 $\frac{K}{s}$. The red dashed line is the Epstein-Plesset solution. B. The same dynamics is replotted using the Epstein-Plesset scaling, showing how the linear to quadratic transition point shifts towards shorter times for larger heating rates.

dissolution time is governed by the Epstein-Plesset dynamics:

$$\tau_{EP} = \frac{\rho R_o^2}{2MD(c_{s_o} - c_i)}. \tag{4.23}$$

If, on the other hand, the heating is strong, Eq. 4.20 provides the second limiting dissolution time:

$$\tau_\alpha = R_o \sqrt{\frac{\rho}{MD\alpha a}}, \tag{4.24}$$

which is inversely proportional to the heating rate α. Fig. 4.3 shows the dissolution time of droplets with initial radii $(80 - 240)$ μm as a function of the heating rate. In Fig. 4.3A, the dissolution time is scaled to the Epstein-Plesset timescale τ_{EP} and in Fig. 4.3B, the dissolution time is scaled to τ_α. The dissolution time matches the Epstein-Plesset timescale for heating rates of 10^{-3} $\frac{K}{s}$ or less, while it is entirely dominated by the heating rate above 1 $\frac{K}{s}$.

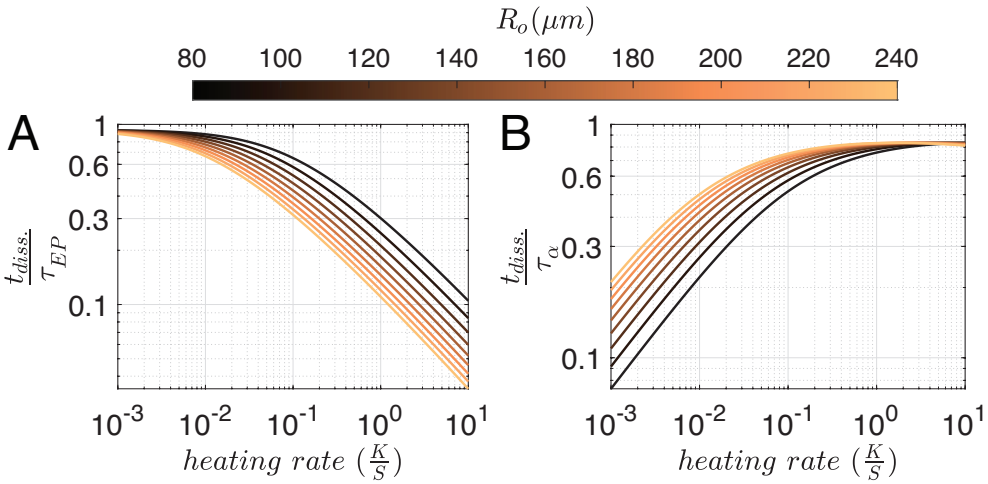

Figure 4.3: A. Non-dimensional dissolution time of droplets with varying radii as a function of the heating rate of the applied temperature ramp. The dissolution time is scaled with the dissolution time predicted by the Epstein-Plesset theory. B. Non-dimensional dissolution time scaled with the dissolution time predicted for large heating rates. A and B represent the limiting cases for weak and strong heating.

4.2 Material and Methods

4.2.1 Capsules/droplet production

The microcapsules were produced using a recently developed high-throughput clog-free liquid jetting method [78]. A schematic depicting the setup for capsule production is shown in Fig. 4.4A. A polymer solution and demineralized water were ejected through the inner and outer channels of a coaxial nozzle to form a compounded liquid jet. The outer channel has an inner diameter of 4 mm while the inner channel has an inner diameter of 100 μm. The outer channel was 3D-printed nylon, while the inner channel was made of a stainless steel needle prolonged by a glass capillary. To ensure the capsules were well dispersible in the oleic acid phase, which was used as the heat transfer fluid, hydrophobic silica nanoparticles were added to the polymer solution. To prevent clogging, the inner diameter of the outer channel is significantly larger than that of the capillary.

A piezo element attached to the nozzle generated vibrations in the direction

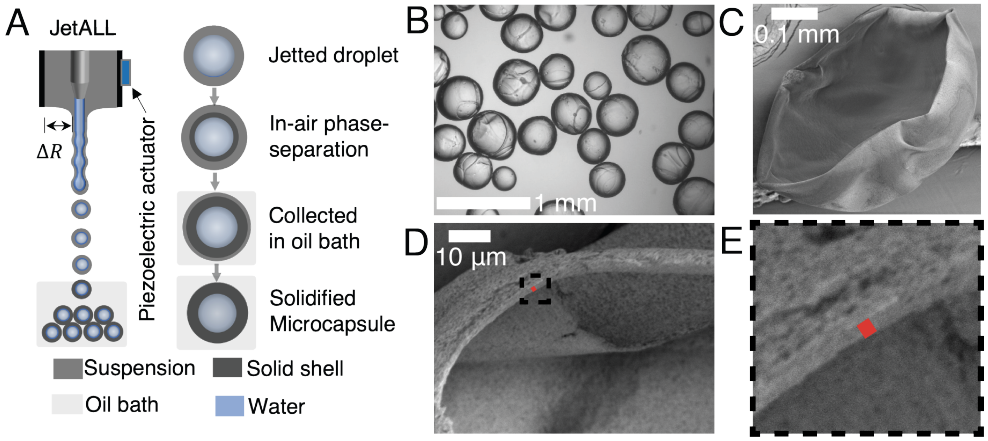

Figure 4.4: A. Sketch of the capsule production setup. B. Optical microscope image of a sample of produced microcapsules. C. Scanning Electron Microscopy (SEM) image showing a collapsed microcapsule observed in high vacuum. D. Cross-sectional view showing the thickness of the shell. E. A zoomed image of (D) with a red line indicating a thickness of 1 μm.

perpendicular to the liquid jet that ensured the compounded liquid jet broke into droplets. A camera was used to visualize the formation of the compound microdroplets. The droplets were then collected in a bath of n-hexane placed approximately 10 *cm* below the nozzle. The polymer layer surrounding the droplets solidified due to the diffusion of solvent toward both the water core and the collection bath. To ensure rapid solidification and to minimize particle aggregation, the flow rate of the polymer solution supply was kept low (2.0 $\frac{ml}{min}$), while for the water it was set to 5.0 $\frac{ml}{min}$, thereby forming a thin shell layer.

The polymer solution was prepared by first dissolving polylactic acid (PLA, Ingeo 4043D, NatureWorks) in dichloromethane to form a dense 20 % (w/v) solution that was magnetically stirred overnight. This solution was then mixed with silica powder (AEROSIL R972) and diluted using a binary solvent mixture of xylene and acetone (volume ratio of 7 : 3). This provided the final ready-to-use polymer solution containing 3% (w/v) silica and 5% (w/v) PLA. All the experiments were performed in a fume hood. After being collected, the capsules were kept in hexane in a sealed container to prevent evaporation.

Fig. 4.4B shows a snapshot of the produced microcapsules under an optical

microscope. The capsules were allowed to dry for over 48 hours by water evaporation which resulted in its deflation. A snapshot of a collapsed capsule observed under a scanning electron microscope is depicted in Fig. 4.4C. This procedure enabled us to examine the cross-section of the shell to measure its thickness, which was found to be 1 μm, as shown in Fig. 4.4 (D-E).

4.2.2 Heating

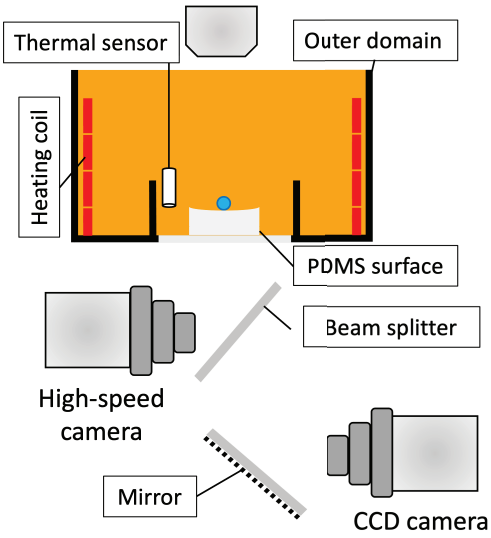

Figure 4.5: Sketch of the imaging setup (bottom-view) to capture the dissolution and vaporization processes. A capsule placed in the bottom of the container is heated through a coil until it completely dissolves or vaporizes. Dynamics are recorded through a CCD camera and a high-speed camera.

An illustration of the experimental configuration employed for the heating of the microcapsules and droplets is depicted in Fig. 4.5. In this setup, a microcapsule (PLA-water) or microdroplet (water) is placed at the bottom on a PDMS surface within a container filled with oleic acid. The heat transfer fluid is subjected to a thermal ramp through a heating element at a controlled rate of 0.4 K per second, gradually increasing from room temperature until the capsule or droplet is either completely dissolved or until it undergoes a phase change.

4.2.3 Imaging

The sample under observation is illuminated by a SUMITA LS-M352 fiber optic light source. The light is directed towards the capsule/droplet through a diffuser. Subsequently, a beam splitter (50/50) is employed to observe dissolution through a CCD camera (Lumenera LM165M) at a frame rate of 2 frames per second (fps) and vaporization with a Photron FASTCAM SA-Z high-speed camera at 100kfps. Both cameras are connected to a Navitar 12x magnification adjustable zoom lens, providing a resolution of 0.92 μm per pixel and 17.6 μm per pixel, respectively.

4.2.4 Image analysis

To determine the instantaneous radius of the microcapsule and microdroplet during dissolution, the encapsulated bubble and free bubble, respectively, are segmented through a black and white (B&W) image threshold in MATLAB. In both cases, the radius of the vapor bubble is calculated using the formula $R = \sqrt{\frac{A}{\pi}}$, where A represents the area of the bubble in the image. It is important to highlight that as the bubble expands, the radius of the encapsulated bubble becomes equal/identical to the free bubble over time as the vaporizing droplet/capsule transforms into a sheet. In the case of dissolution, we assume that the capsule has the shape of an ellipsoid and determine from its projection in the image plane the major axis ($2a$) and minor axis ($2b$) lengths using the `regionprops` function in MATLAB®. The instantaneous equivalent radius is then calculated using the formula $R = \sqrt[3]{a \cdot b^2}$ [79], where a and b represent the semi-major and semi-minor axis lengths, respectively. It allows the determination of the radius of a sphere that has the equivalent volume as the ellipsoid.

4.2.5 Experimental curve fitting

The experimental dissolution curves were fitted to the dissolution model using the iterative procedure of section 4.1.1. The least square method `lsqcurvefit` in Matlab was used to fit the diffusion coefficient D, the initial concentration difference $c_{s_o} - c_i$, and the rate of increase of the saturation concentration with temperature a. Initially, the temperature is constant as the set temperature remains below the bath temperature, which is usually around 310 K. During this time, $a = 0$. After that, the temperature effectively ramps up and dissolution accelerates. The time at which the temperature starts to change

was extracted from the velocity of the droplet wall, which shows a clear and expected rise of slope (see for example Figs. 4.8(C-D)).

4.3 Results

4.3.1 Droplets and capsules dissolution

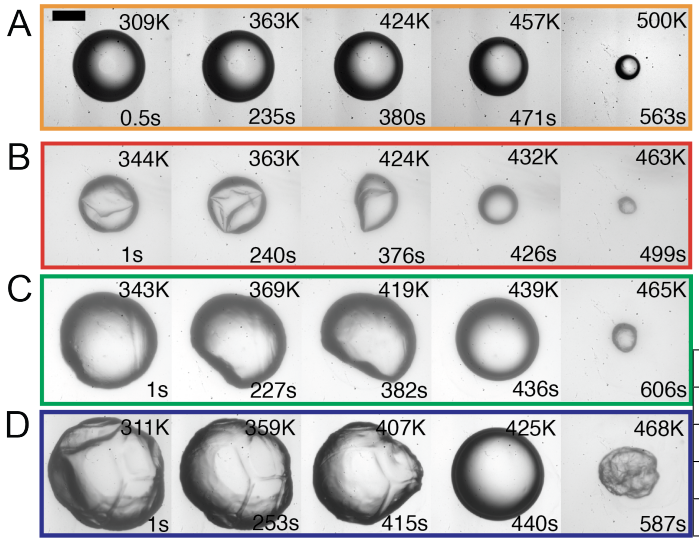

Fig. 4.6	R_o (μm)
A	220
B	178
C	293
D	347

Figure 4.6: Dissolution dynamics of a water microdroplet (A), and microcapsules (B-D). The corresponding radii are given in the table to the right. Time points and the corresponding temperature of the heating bath are given in each frame.

Figure 4.6A shows snapshots of a water droplet dissolving in oleic acid being exposed to a temperature ramp of 0.4 K per second. Initially, the dissolution is minimal until approximately 235 seconds, whereafter it completely disappears within a comparable amount of time. A series of snapshots of the dissolution of three microcapsules with different sizes is shown in Figs. 4.6B, C, and D. The corresponding radial dynamics is shown in Figs. 4.7A and C for microdroplets and microcapsules, respectively. Microcapsules replicate the dynamics of microdroplets and show little change as they reach the boiling temperature of the cores, as illustrated in the second frames of the image sequence in Fig. 4.6,

as well as by the initial slow dissolution region in Fig. 4.7. During this period, the polymer temperature exceeds the glass transition temperature (328 - 333 K) and therefore acquires a soft or elastic state. Thus, the slow dissolution leads to buckling and enhancement of pre-existing surface creases.

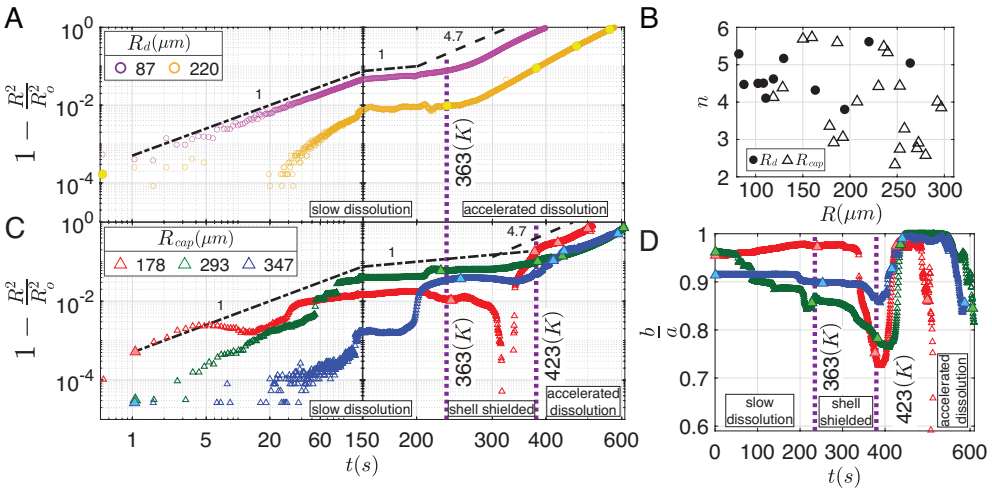

Figure 4.7: Radial dynamics plotted as $1-\frac{R^2}{R_o^2}$ vs. time for microdroplets (A) and microcapsules (C). B. Power of the radial dynamics in the fast dissolution phase as a function of the initial size of both droplets and capsules obtained through a power law fit. The fitting for droplets begins at 263 s (378 K), while for capsules it starts at 394 s (430 K). D. Shows the non-sphericity of the microcapsules depicted by the major-to-minor axis ratio vs. time. The dotted line plotted at 363 K and 423 K represents water boiling point and polymer melting point, respectively, and corresponds to the time of 238 $\pm$ 4 s and 384 $\pm$ 8 s.

Earlier work [71] showed that the dissolution of a water droplet placed in octadecene subjected to the same temperature ramp follows the scaling law $(1-\frac{R^2}{R_o^2}) \sim t$ until about 363 K, i.e., close to the boiling point of water. Above this point, dissolution significantly accelerates and follows a power law $(1-\frac{R^2}{R_o^2}) \sim t^{6.5}$. We observe the same trend in the present study where we use oleic acid as the heat transfer fluid as shown in Fig. 4.7A. However, the exponent is now 4.7. Fig. 4.7B displays the power law fit for various droplet sizes (circles), resulting in a mean value of 4.7 $\pm$ 0.45.

Above 363 K the microcapsules continue to experience slow dissolution as they are protected by the shell, see Fig. 4.7C. Around the melting temperature of the polymeric shell (418 - 433 K), the capsules rapidly transition from a pronounced buckled state to a smooth spherical shape resembling that of a droplet, visible in the third and fourth frames of the image sequence of Fig. 4.6B to D. In the time frames that lead to this transformation, the major-to-minor axis ratio first decreases before suddenly increasing to a value of 1, see Fig. 4.7D. After this transition, the capsules enter a regime of accelerated dissolution, similar to that experienced by the microdroplet above 363 K, see Fig. 4.7C. Figure 4.7B shows that a power law of 3.9 $\pm$ 1.1 for the capsules, with considerably more variation than that found for the microdroplets. This variability may arise from inhomogeneities of the shell material. Prompted by the rapid dissolution at the highest temperatures, the microcapsules rapidly reach a deformation ratio diverging once again from spherical symmetry during the final stage, see Fig. 4.7D, the capsules now exhibiting a non-spherical shape as the core reaches a minimal volume, while the compressed shell material persists. The capsules then display a highly irregular, crumpled structure, see e.g. last frame of Fig. 4.6D, most likely caused by a collection of nanoparticles that are part of the shell composition, see e.g. last frame of Fig. 4.6D.

4.3.2 Experimental comparison with the dissolution model

Figure 4.8 shows the dissolution curves $R(t)$ (A-B) and the interface velocity $\dot{R}(t)$ (C-D) of a dissolving microdroplet (A-C) and microcapsule (B-D) of comparable sizes. The experimental curves are fitted to the dissolution model as explained in the section 4.2.5. In these examples, the heating ramp effectively starts at about $t = 250$ s and $t = 120$ s for the microdroplet and the microcapsule, respectively. While the model features a simplified linear dependency of the saturation concentration on temperature, by virtue of a lack of experimental data, it captures all the important features of bubble dissolution. First dissolution is slow and nearly steady. When the temperature ramp starts, it suddenly accelerates and the dissolution rate becomes dominated by the heating rate. The fit for the capsule shows less of a correspondence due to the complexity of the buckling of the capsule and the non-trivial effect of the shell on the dissolution process. Yet, the main dynamics is captured, which allows for the extraction of effective mean physical parameters.
The fit provides values of $D = 2.3 \pm 0.9 \times 10^{-9}$ $\frac{m^2}{s}$ for the microdroplets and $D = 1.3 \pm 0.7 \times 10^{-9}$ $\frac{m^2}{s}$ for the microcapsules. While the large standard deviations found for these values do not allow for a final conclusion, they suggest

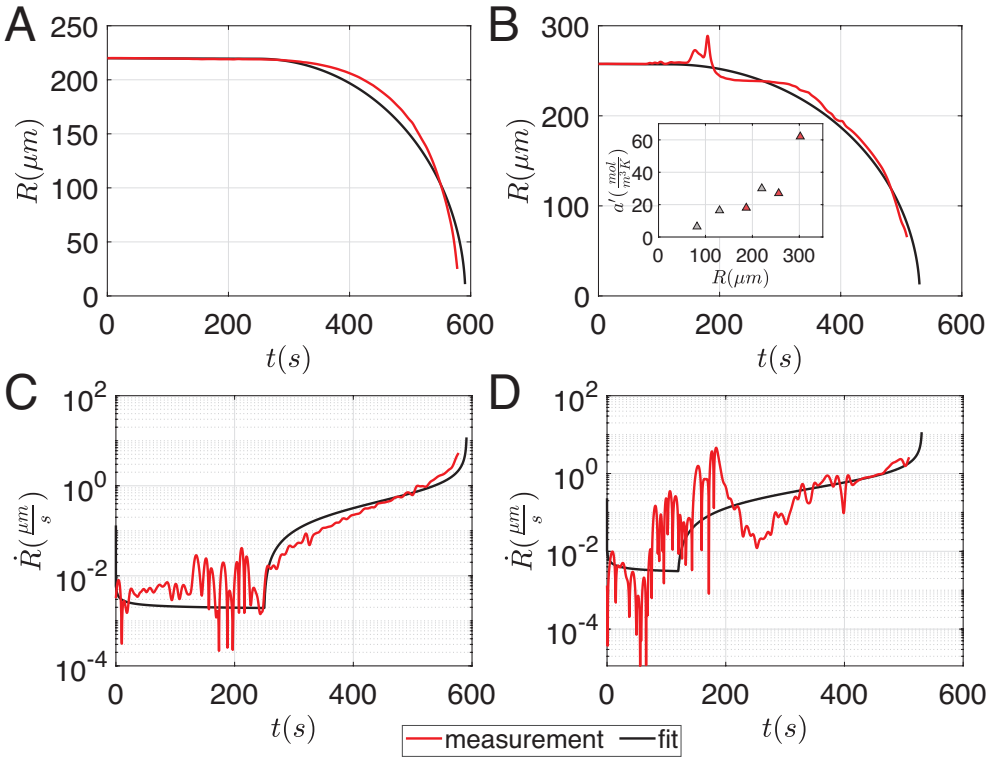

Figure 4.8: A. Experimental dissolution curve of a 220 μm droplet subjected to a 0.4 $\frac{K}{s}$ temperature ramp. The initial temperature is 310 K and the ramp starts at $t \approx 250$ s. B. Experimental dissolution curve of a 256 μm capsule subjected to a 0.4 $\frac{K}{s}$ temperature ramp. The initial temperature is 308 K and the ramp starts at $t \approx 120$ s. Modeled and measured dissolution speeds of (A-B) are plotted in (C-D) respectively. The solid black curve is the fit of the model to the experiments. The insert in (B) shows the fitted rate of increase of the saturation concentration with respect to temperature, as a function of the radius. The grey markers represent the microdroplets, and the red markers represent the microcapsules.

that the shell significantly reduces the effective diffusivity. The values fitted for the initial concentration difference were $c_{s_o} - c_i = 7.6 \pm 2.8 \ \frac{mol}{m^3}$ for the microdroplets and $c_{s_o} - c_i = 16 \pm 13 \ \frac{mol}{m^3}$ for the microcapsules. These parameters should, a priori, show the most variation since, first, the concentration of water in the oleic acid changes in time due to the experiment themselves and, second, due to environmental conditions around the experiment. However, the initial concentration differences found are low as compared to the saturation concentration $c_{s_o} \approx 262 \ \frac{mol}{m^3}$ at 310 K [77], which corresponds to 4.7 $\frac{mL}{L}$. The oleic acid is thus saturated at over 95% with water before the recording of the bubble dissolution, which was already clear from the near-zero dissolution rate before the application of the temperature ramp. Finally, the fitting procedure provides an average value of the rate of change of the saturation concentration with respect to temperature $a' = 26 \ \frac{mol}{m^3 K}$. However, a' demonstrates strong dependency on the microdroplet, c.q. microcapsule radius, as plotted in the inset of Fig. 4.8C. a' is lower for the microcapsules (red markers) than for the microdroplets (grey markers), but its dependency on size is weaker. This clear dependency of a' on size is most likely an indirect effect of the longer dissolution times for large sizes, which therefore experience a higher temperature. This, in turn, shows that the assumed linear increase of the saturation concentration with temperature is not a very precise representation, even though if it is sufficiently accurate to fit the dissolution curves.

4.3.3 Dissolution to vaporization transition

Fig. 4.9A provides a typical example of the radial dynamics of a microcapsule that undergoes nucleation before it has fully dissolved. The radius is normalized to the initial capsule radius. Three snapshots are shown, with the first snapshot at $t = 0.5$ s depicting visible surface wrinkles over the capsule interface. Around 440 s the radius of the capsule is decreased by 3 %, and upon reaching 561 s the capsule rapidly shrinks with the radius being reduced by 20 %. It then displays the smooth surface morphology described in the previous section, and evidenced in the accompanying snapshot. At this point, the capsule reaches a temperature of 224 °C, which triggers a phase change. This results in the formation of a vapor bubble with a radius four times that of the initial capsule within 6 ms, 0.001 % of the overall time (561 s), as depicted by the sudden spike in size, see the associated snapshot.
To quantify the effect of the shell on the nucleation statistics, we can compare the influence of temperature on the probability of dissolution or vaporization for different droplet sizes in Fig. 4.9B and to that of microcapsules in Fig.

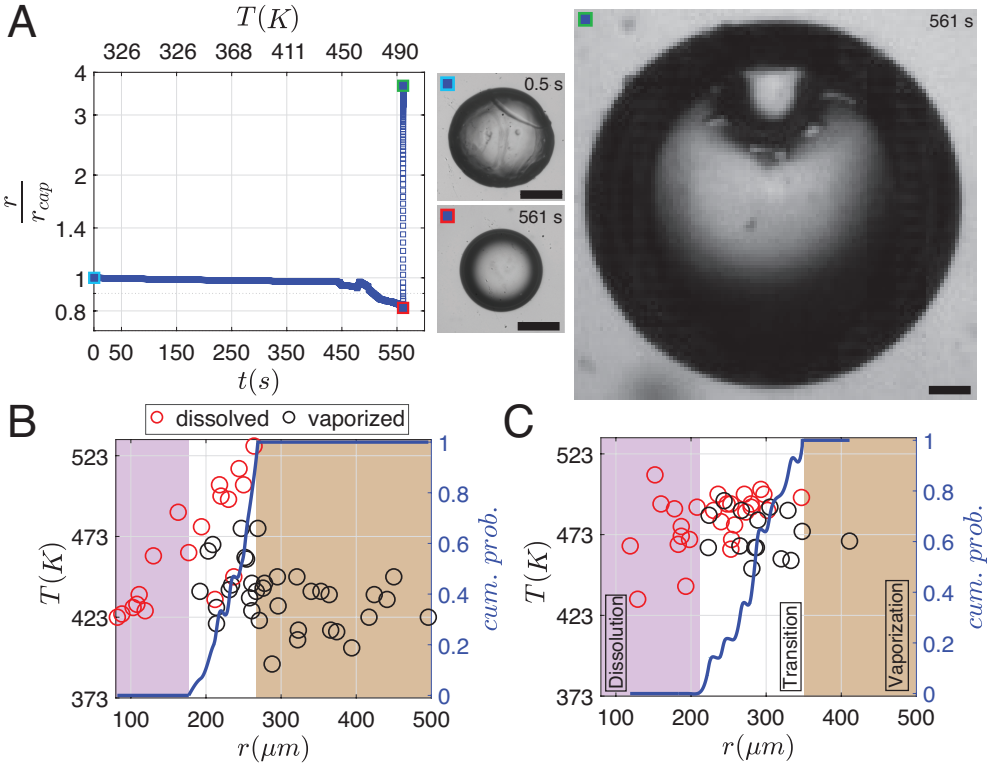

Figure 4.9: A. Radial dynamics of a microcapsule (R_{cap} : 244 μm) subjected to a temperature ramp. Snapshots on right correspond to the colored markers indicated in (A). B. Phase diagram of dissolution (purple) and vaporization (brown) for microdroplets and microcapsules (C) with a transition region indicated in white. Y-axis: left, indicating the measured dissolution/nucleation temperature with circles (red and black); right, represents the vaporization probability obtained by normalized cumulative sum of binary data (blue line), where 0 denotes dissolved, and 1 represents vaporized. (scale bar: 200 μm)

4.9C. Both figures are divided into three regions indicating complete dissolution, vaporization, and the transition region between the two, represented by a pink, brown, and white, background, respectively. The dissolution temperature, i.e. the temperature at which the droplet/capsule fully dissolves in the heating medium, rises for microdroplets with increasing size, while for microcapsules it is scattered. Where the dissolution temperature corresponds to the temperature at which the droplet/capsule fully dissolves in the heating medium. For microdroplets, as the size increases, the dissolution requires more time thus the temperature reached is higher. Microcapsules, on the other hand, may be influenced by structural differences of the shell, leading to the observed scatter in the data, although it is not quantified in this study. In general, both probability curves indicate that the likelihood of nucleation increases with an increase in size. However, the transition region for microdroplets (190 - 270 μm) is smaller than that for microcapsules (220 - 348 μm).
Microdroplets exhibit an average nucleation temperature, i.e. the maximum temperature that a droplet/capsule can withstand before it nucleates, of 437 $\pm$ 19 K, while microcapsules display a notably higher average nucleation temperature: 473 $\pm$ 13 K. Where the nucleation temperature corresponds to the temperature withstood by the droplet/capsule before a bubble is nucleated. We have demonstrated in our earlier study that microdroplets can nucleate at multiple interfaces, namely at liquid-solid, and liquid-liquid, interfaces, as well as at the liquid-solid-liquid contact line [71]. The interface determines the energy required for nucleation, and thus the temperature [39]. In Fig. 4.9B, droplets can be seen nucleating even at a lower temperature, around approximately $\sim$ 393 K. In contrast, nucleation in microcapsules is limited to the shell-core interface, further discussed in section 4.3.3. Consequently, for microdroplets, this leads not only to a lowering of the droplet's nucleation temperature but also to an increase in the probability of vaporization. On the other hand, the addition of the shell reduces the nucleation likelihood, as evidenced by the decreased steepness in the cumulative probability density function for capsules compared to droplets.

Bubble nucleation and growth

Following incomplete dissolution, nucleation of both droplets and capsules results in bubble formation through vaporization. A typical nucleation interface and the resulting vapor bubble growth for a droplet are shown in Figs. 4.10A and 4.10B, respectively, for nucleation at the liquid-solid (l-s) interface, and in

Figs. 4.10C and 4.10D for nucleation at the liquid-liquid (l-l) interface. The radial evolution of the vaporizing droplet encapsulating bubble, normalized by the initial radius R_o, is depicted in Fig. 4.10F. Notably, the initial growth is damped depending on the location of the nucleation site. In the first scenario (l-s), the bubble starts to expand from the initially one pixel-sized nucleus

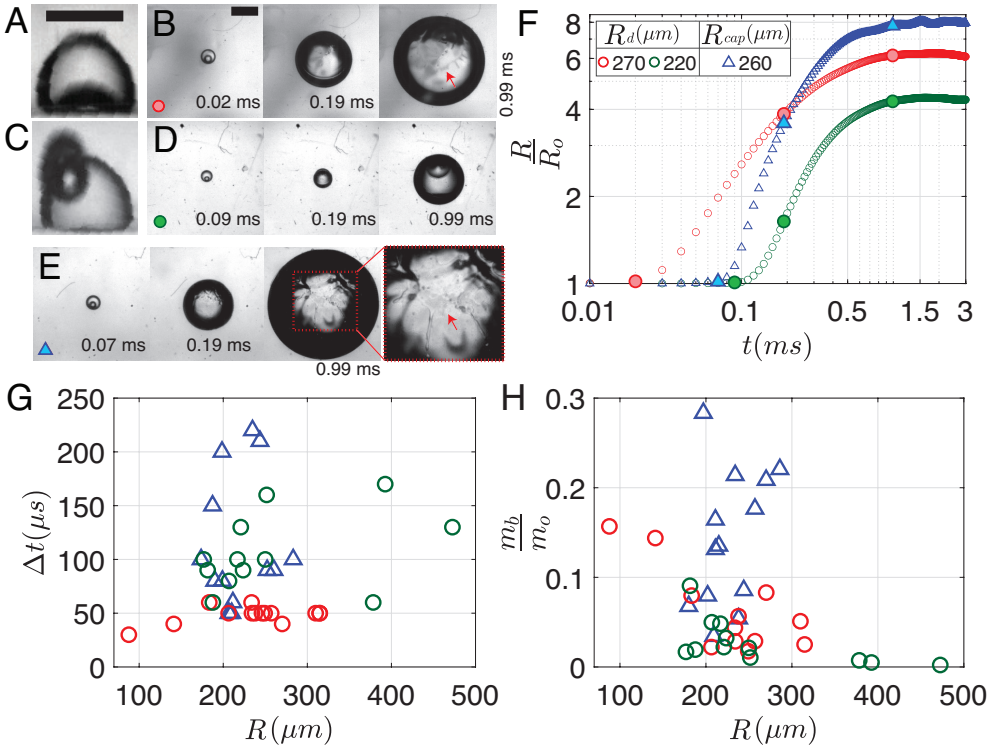

Figure 4.10: Side view images show typical nucleation sites of microdroplets without encapsulation: (A) at the liquid-solid (l-s) interface, and (C) at the liquid-liquid (l-l) interface. Bottom view images show the vaporization of microdroplets: B. l-s interface at $T : 415\ K$, D. l-l interface at $T : 439\ K$. E. Snapshots from a bottom-view recording of the vaporization of a microcapsule at $T : 475\ K$. F. Radial dynamics evolution of B, D, and E with droplet radius R_d (red and green circles) and microcapsule radius R_{cap} (blue triangles) plotted against time t. G) Time duration for $(\frac{R}{R_o})$ to rise over 1. H) Fraction of mass vaporized. Circles and square markers indicate l-s and l-l interfaces, and triangles indicate capsules. Scale bar: 1 mm.

within 20 μs, while in the second case (l-l), this process takes approximately 100 μs to start. In Fig. 4.10G, we quantify this by extracting the time it takes for $(\frac{R}{R_o})$ to increase by 1 % for different droplet sizes, with red and green circles denoting liquid-solid and liquid-liquid interfaces, respectively.
An image sequence depicting capsule vaporization is shown in Fig. 4.10E, while the resulting radial expansion of the vapor bubble is plotted in Fig. 4.10F. Notably, the initial growth is delayed, similar to observations of nucleation of the droplet at the liquid-liquid interface. This delay is quantified for various capsule sizes in Fig. 4.10G, represented by triangles. Since the shell inhibits contact between the core and external interfaces that may contain foreign nuclei, nucleation is anticipated to occur at the core-shell interface. This is further supported by Fig. 4.9C, where capsules favor dissolution, resulting in a lower probability of vaporization. Thus the shell allows capsules to sustain a degree of super-heat, of approximately 50 K.
The expansion of the vapor bubble causes microcapsules to transform into a sheet as the bubble expands, similar to the bubble growth observed when nucleation occurs at the liquid-solid interface of droplets (see ref. [71]). The liquid sheet exists in a metastable state and eventually retracts along the bubble surface, as indicated by the red arrows in the last frames of the image sequence (Figs. 4.10A and E). The sheet formation maximizes the surface area available for mass transfer, leading to a larger volume of vaporized mass. It can be seen in Fig. 4.10H, where the mass fraction vaporized for different sizes is plotted for both droplets and capsules. In contrast, the bubble nucleated at the liquid-liquid interface remains only in partial contact with the droplet (Fig. 4.10C), resulting in a less exposed area for vaporization, and thus a suppressed bubble growth. In some cases for capsule vaporization, it is expected that the bubble is fully encapsulated and stabilized by the liquified shell, thereby delaying sheet retraction. This delay facilitates a larger mass fraction vaporized of the liquid core (see Fig. 4.10H).

4.3.4 Bubble growth model

In our earlier work [56], we developed a model for the dynamics of vapor bubbles as a result of the vaporization of superheated water droplets in oil. It is based on a classical understanding of vaporization dynamics and considers a Rayleigh-Plesset-type equation to account for momentum, thermodynamics of vaporization, and heat transfer through the convection-diffusion equation. Subsequently, we incorporated the physics of sheet retraction in the model based on experimental observations [71]. Here we aim to explore its validity

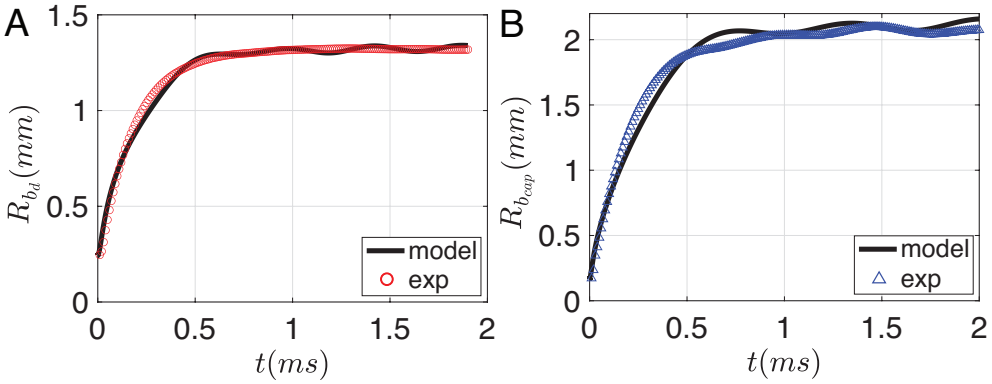

Figure 4.11: Experimental and numerical simulations of the vapor bubble growth: bubble radius R_b vs. time. A. Vapor bubble radius R_{b_d} for a microdroplet with R_d : 242 μm, T : 405 K. B. Vapor bubble radius $R_{b_{cap}}$ for a microcapsule R_{cap} : 260, T : 423 K.

on capsule vaporization with a thin melted/soft shell, which experimentally shows sheet retraction.
The numerical solution of the model utilizes temperature as a fitting parameter, where the retraction start time is kept at a constant value of t = 0.304 ms, with a drag coefficient set at 0.15. These parameters were initially determined for droplet vaporization as outlined in [71]. Figs. 4.11A and B present a comparison of the vaporization dynamics of a microdroplet (red) and microcapsule (blue), alongside the corresponding numerical results (black). The model is in good agreement with the experimental data. This shows that the vaporization of the microcapsule configuration explored in this study is also dominated by the dynamics of sheet retraction and that it plays a dominant role over inertial and thermal diffusion-dominated growth.

4.4 Study limitations

The model developed for dissolution can account for unsteady boundary conditions, but it was not adjusted for the presence of the substrate [72]. Although this correction is small, it may have some impact on the fitting of the experimental curves and the values extracted. However, given the morphology variation in different capsules, it is unlikely to lead to any significant change. Another limitation of the present study is that microcapsules had differences

in major-to-minor axis ratio that we treated as projected spheroids, see Fig. 4.7D. In Fig. 4.7C, a discrepancy may occur due to the capsules not being perfect spheroids. Additionally, the threshold applied during image processing may also lead to artifacts in the analysis that are then magnified on the logarithmic scale.

4.5 Conclusion

In this study, we have explored how the presence of an encapsulating shell affects the dissolution and vaporization dynamics of a water microdroplet undergoing a temperature increase in a heat transfer fluid. The shell delays the onset of the rapid dissolution, pushing it to the polymer's melting point (423 K). In contrast, water droplets without encapsulation experience an accelerated dissolution close to their boiling temperature. Utilizing an Epstein-Plesset type model that includes a linear increase of the saturation concentration at the interface we reproduced experimental recordings of the dissolution of both microdroplets and microcapsules. As the shell prevents contact of the liquid core with potential nucleation sites in the host liquid, the microcapsule must rely on the shell-core interface for nucleation, thereby reducing the probability of vaporization as compared to microdroplets. Numerical simulations confirm that for capsules the vapor bubble dynamics after nucleation is comparable to that of droplets without a shell and that it is primarily influenced by sheet retraction, despite the initial delay in nucleation and vapor bubble growth.

Chapter 5

Additive manufacturing of 3D flow-focusing millifluidics for the production of mono-sized curable microdroplets[1]

Microfluidics plays a crucial role in generating mono-sized microdroplet emulsions. Traditional glass microfluidic chips typically lack the versatility in generating curable droplets of certain liquids due to the inherent hydrophilic nature of glass and fabrication constraints. To overcome this, we designed a microdroplet generator with 3D flow-focusing capabilities that can be 3D-printed. The chip can handle oil-in-water emulsions despite its lipophilicity. Operating in the jetting regime, the chip utilizes the Rayleigh–Plateau instability to ensure high throughput. With its versatile design, the chip is capable of producing both single and double emulsions within the same channel. We utilize a thermoset (epoxy–melamine) based system to test its ability to handle curable chemicals and to produce in a post-processing step both solid particles and filled capsules. With a low solvent concentration in the curable material, the present system can encapsulate water-based cores of a wide range of sizes.

[1]Submitted as: **Muhammad Saeed Saleem**, Timothy T.K. Chan, Michel Versluis, Dominik Krug, and Guillaume Lajoinie, *Additive manufacturing of 3D flow-focusing millifluidics for the production of mono-sized curable microdroplets.*

5.1 Introduction

Monodisperse particles and capsules hold high technological value due to their broad range of applications from fundamental scientific research to industry. Neutrally buoyant particles can be used as tracers to visualize flows [80, 81], heavy particles can be employed as model particles to improve our understanding of how mineral extraction from an aqueous slurry of the ground ore [82]. The use of microcapsules spans across pharmaceuticals [66, 83], enabling the precise and localized release of drugs, in agriculture [84, 85] for slow-release micro-encapsulated fertilizer, and for energy storage as a phase change material [86]. Producing particles and capsules with fine-tuned properties is therefore both scientifically appealing and technologically important.

In literature, the most common methods to produce small monodispersed particles is by curing droplets [87–91]. Hence, generating droplets is the first step in this process. Droplets are typically generated in microsieves [46, 92], where the liquid breaks up into droplets after passing through an orifice, or microfluidic chips with coaxial flow, T-junction, or flow-focusing geometries [93, 94]. The flow-focusing geometry is especially interesting as it can reach high production rates, as utilized by Yobas et al. (2006) [95] to produce water-in-oil and oil-in-water droplets with a production rate of 10,000 Hz and 1,000 Hz, respectively. In this geometry, a jet formed by the dispersed phase is squeezed from two sides by the surrounding liquid (continuous phase) to form droplets.

One of the challenges in the design of microfluidic droplet generators is to ensure that the channels can effectively handle both water/oil and oil/water-based systems with excellent wetting properties. Glass, which is widely employed for microfluidic chips due to its excellent durability and optical transparency, is hydrophilic and typically manufactured with 2D (planar) geometries. When water is used as the dispersed phase, the jet can adhere to the upper/bottom walls, hindering droplet formation. In this case, surface treatments are necessary to increase hydrophobicity of the chip while introducing additional variables in the chip design process.

In principle, the wetting effects can be eliminated by employing three-dimensional flow geometries where the jet is axisymmetrically contained by the continuous phase [94]. While this approach is complex and expensive to fabricate in glass chips, it is applicable in rapid-prototyping types of chips with polydimethylsiloxane (PDMS). Manufacturing microfluidic droplet generators through 3D-printing is an attractive alternative for glass chips as it offers much greater

freedom in the chip geometry, greatly simplifies the manufacturing process and reduces the cost when produced on a small scale. Various studies (see e.g. refs. [96, 97]) have reported droplet generators with a range of geometries and liquids. One of the first attempts was performed by Shallan et al. (2014) [98], who qualitatively demonstrated the concept by generating aqueous droplets in an organic solvent. Studies followed which employed chips with various geometries (with rectangular or circular channel cross-sections) and either the flow-focusing or T-junction configuration, see e.g. refs. [99, 100]. Bhargava et al. (2014) [99] produced water-in-oil droplets by operating a flow-focusing chip in the jetting regime. Donvito et al. (2015) [100] and Dewandre et al. (2020) [101] showed that the monodispersity of droplets generated using 3D-printed chips is comparable to conventionally manufactured devices. Building on these successes, an introductory extension to more complex droplet morphologies, such as double emulsions [88], has been achieved by linking multiple droplet generators in series using O-rings [102].

Producing droplets is only the first part of the process of making particles or capsules since the liquid droplets still need to be solidified. Solvent evaporation [103], utilized e.g. Visscher et al. (2019) [46], can be used to cure droplets. In this process, liquid droplets containing either dichloromethane, hexadecane, and PMMA or dichloromethane, perfluorocarbon oils, and PGLA can be generated. By stirring the solution, the droplets remain suspended, giving time for the solvent to evaporate yielding particles or capsules. Particles have also been produced by utilizing droplets consisting of photo-active [88, 104] and heat-activated resins [90]. Despite their advantages only recently Zhang et al. (2023) [90] utilized 3D-printed microfluidic chips to produce curable droplets with complex chemicals.

In this work, we make use of the versatility and cost-effectiveness of 3D-printing to design a fully three-dimensional flow-focusing millifluidics channel that can produce curable single- and double-emulsion microdroplets. The chip is operated in the jetting regime for high production rate. Despite the inherent lipophilicity of the chip material, the present chip geometry does not require any surface treatment to produce droplets with an oil-based dispersed phase. We employ a model system based on a thermoset resin comprising epoxy–melamine to demonstrate the chip's ability to handle complex curable mixtures. Following droplet production, single-emulsion droplets are cured into particles and capsules by stirring and heating, while the double-emulsion droplets undergo shell polymerization to form capsules.

5.2 Materials and methods

5.2.1 3D millifluidic chip

The chip is printed using a Formlabs Form 3+ 3D printer with clear v4 resin. Following printing, the chip is cleaned thoroughly with isopropyl alcohol (IPA), air-dried, coated on one side with the same resin for improved optical transparency, and subsequently cured at 60°C for 7 hours. A sketch of the 3D millifluidic chip demonstrating the formation of double emulsion droplets is shown in Fig. 5.1A. To form capsules that encapsulate pure water, a water-based continuous phase and an oil-based shell phase are formulated and will be discussed later in section 5.2.3. The chip comprises two flow-focusing junctions and four channels: one for a continuous phase, two for the dispersed phases (shell and core), and an outlet channel where droplets are collected. At the first junction, the shell phase is focused by the continuous phase while at the second junction, the core phase is focused by the shell phase. Downstream in

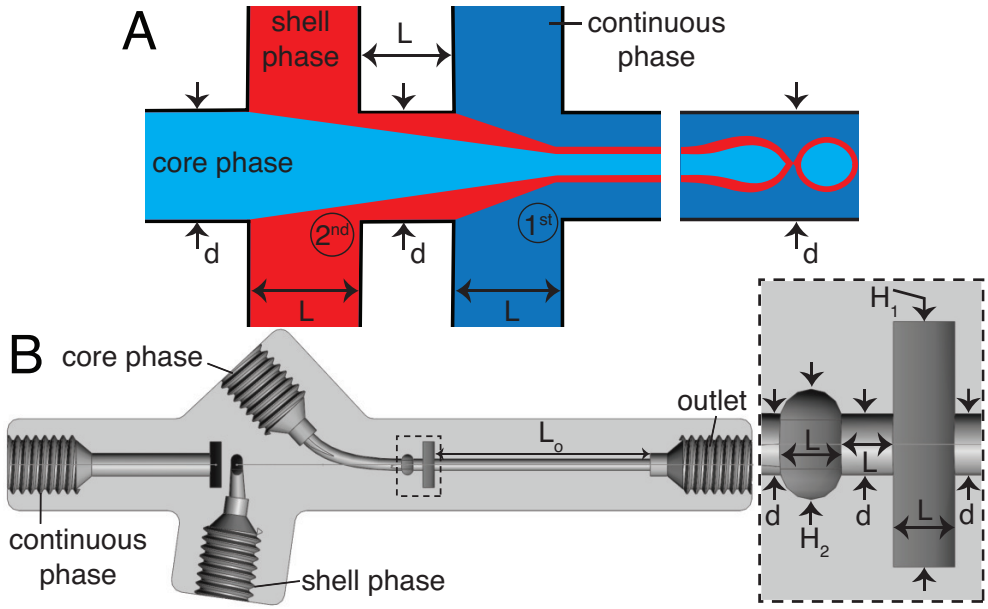

Figure 5.1: A) A sketch illustrating a double emulsion flow junction. B) A SolidWorks® cross-section view of the droplet generator along the centreline. $H_1 = 4\ mm$, $H_2 = 2\ mm$, $d = L = 1\ mm$, $L_o = 19\ mm$.

the outlet channel, a co-flow is generated where the jet breaks up into droplets due to the Rayleigh–Plateau instability.
A cross-section of the 3D millifluidic nozzle design is shown in Fig. 5.1B. At both junctions, the channel height of the phase being focused is always higher than the focusing phase. This allows non-planar flow-focusing and prevents the jet from wetting the channel walls. This concept was applied by Castro-Hernandez et al. (2016) [94] to generate micron-size droplets with a junction height of 50 μm. In the present case, the first junction has a height (H_1) of 4 mm and the second junction has a height of 2 mm. We observed that the 3D-printed material has an inherent lipophilic affinity and therefore wetting from the oil-based shell phase is prevented by keeping the height of the first junction at 4 mm thereby dissipating surface energy, that dose not require a need for surface treatment. The length of the outer channel (L_o) is kept at 19 mm to ensure sufficient space for jet formation and breakup.

5.2.2 Operation

Figure 5.2 displays a schematic of the setup for producing microparticles or microcapsules. To generate single emulsion droplets, the core phase inlet is initially left open, and the continuous phase is first allowed to wet the channels. As the continuous phase begins to drip from the outlet, the core phase channel is sealed with a fingertight microfluidic plug. The shell phase is then slowly introduced to form a jet that breaks up into droplets. Since there is

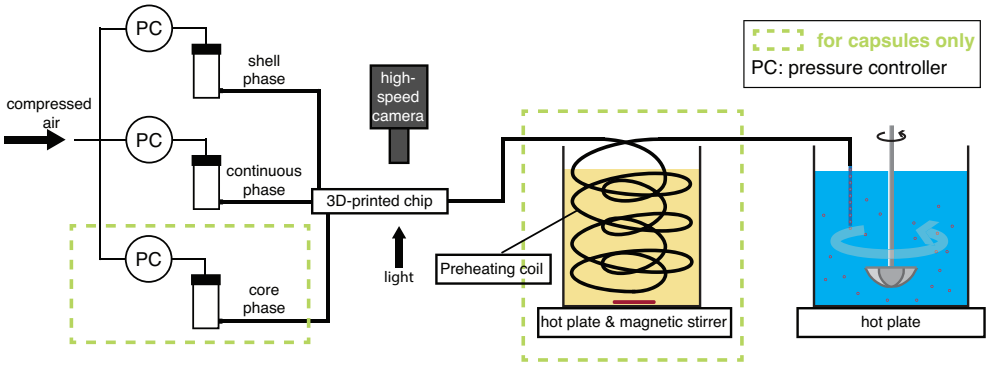

Figure 5.2: Schematic of the experimental setup. The chemicals are forced into the fluidic chip with compressed air to form droplets, which are subsequently cured into particles or capsules by stirring and heating.

no shell present in the single emulsion, the shell phase hereafter is referred to as the dispersed phase. In the case of double emulsion, the core phase is also infused next to the shell phase creating a coaxial jet that breaks up into double-emulsion droplets. All the connections on the chip were made with PEEK fingertight connectors and PEEK tubing with an inner diameter of 1 mm except for the core phase, where 0.5 mm tubing is used in view of the lower liquid viscosity. The entire process is observed using a high-speed camera (Photron Fastcam SA-X2) connected to a Navitar 12× adjustable zoom lens with back illumination.
After the droplets are produced, the suspension passes through an outlet tube. For the double-emulsion case, the outlet tube is connected to a coil immersed in a 50°C sunflower-oil-bath to trigger polymer network formation in the shell. The bath was stirred by a magnetic stirrer at 900 rpm to reduce thermal gradients. Once the droplets exit the outlet tube, they are collected in a beaker filled with 5% Tween 80–water solution at 40°C and cured into particles and capsules. The mixture is stirred using a Heidolph overhead stirrer at 150 rpm during collection and at 250 rpm for the remainder of the process to prevent sedimentation. Over the next 4 hours, the solution is maintained at 40°C for the particles or capsules to reach maximum polymer strength. This elevated temperature, which is the solvent's boiling point, triggers fast evaporation [71, 105] and is therefore expected to quickly stabilize the curing droplets, especially for the double-emulsion droplets during the initial stage. After 4 hours at 40°C, the suspension was allowed to cool down for an hour whilst being stirred before the particles and capsules were analyzed.

5.2.3 Continuous and dispersed phases

The continuous phase is comprised of 40% glycerol and 60% water mixture. This optimum mixture was selected based on a systematic study where the glycerol concentration was varied from 5% to 74%. At low concentrations, the coaxial jet oscillates laterally in the channel, whereas at high concentrations, the droplets coalesce in the outlet tube resulting in slug flow, particularly when the preheating coil is employed, see Fig. 5.2. For the shell phase, we selected a polymer mixture consisting of $1\,g$ ($1.17\ \frac{g}{ml}$) of epoxy resin, $1\,g$ ($1.165\ \frac{g}{ml}$) of hardener, and $0.5\,ml$ melamine crosslinker, with $0.2\,g$ ($0.98\ \frac{g}{ml}$), dinonylnaphthalenedisulfonic acid (DNNDSA) acting as a catalyst. The acid's hydrophobic nature inhibits diffusion of the curing resins into the surrounding liquid. Upon addition of $0.1\,mg$ of Nile red dye the mixture had a total volume of $V_{diss} \approx 2.42\ ml$ of which 10 % is butanol (BU). The mixture is dissolved in

dichloromethane whose concentration varies for particles and capsules as will be discussed in the following subsections. The optimal concentration of each component was determined (except DCM) via trial and error by mixing them in a petri dish and subsequently heating the mixture to 40 ^{o}C in an oven, aiming to achieve the minimal reaction time to gel i.e. losing fluidity.

5.2.4 Materials

Each chemical was used without dilution or preconditioning. Melamine formaldehyde resin (MR) was provided by Allnex, marketed under the trade name SETAMINE US-132 BB-71. The epoxy resin (ER) and crosslinker (EC) with the name Araldite Rapid were purchased from Araldite. Dichloromethane (DCM), dinonylnaphthalenedisulfonic acid solution (DNNDSA), and Tween 80 were purchased from Sigma Aldrich. Glycerol (G) was purchased from Laboratoriumdiscounter, and water (W) was collected from the Milli-Q type 1 ultrapure water systems. PEEK tubing was purchased from Fisher Scientific.

5.2.5 Analysis

The analysis is divided into two parts: on-chip droplet sizing and cured droplet characterization. On-chip sizing is performed by analyzing the images captured by the high-speed camera in an image processing algorithm programmed in MATLAB®. A background image was first subtracted from each frame and the resulting images were binarized to identify the droplets. Then assuming cylindrical symmetry, we sliced the droplet along the horizontal axis x as shown in Fig. 5.3A where the contours are plotted overlaying the droplet

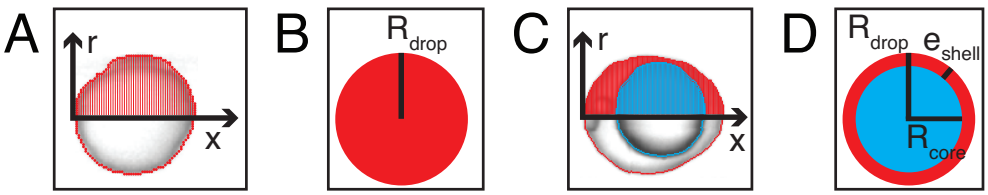

Figure 5.3: Contours plotted over single emulsion in red (A) and double emulsion (C) droplets (shell: red, core: blue). The encapsulated satellites in capsules were not detected in the analysis. A sketch defining the radius of single emulsion (B) and double emulsion (D) droplets.

image. The surface area is calculated by $A_{drop} = \sum_i 2\pi r_{x_i} \delta x$, where $r(x)$ denotes the distance from the horizontal axis x to the droplet edge and δx is the width of each slice. The droplet radius and its volume are then given by $R_{drop} = \sqrt{\frac{A_{drop}}{4\pi}}$ (see Fig. 5.3B) and $V_{drop} = \frac{4}{3}\pi R_{drop}^3$, respectively. For the double-emulsion case, the core is segmented by applying an additional image binarization threshold, as shown in Fig. 5.3C where the contours of the core and droplet are plotted. The core radius R_{core} and volume V_{core} are found analogously. The shell thickness is then derived from $e_{shell} = R_{drop} - R_{core}$A sketch defining each parameter is shown in Fig. 5.3D. To characterize the cured particles or capsules, the cured samples were first imaged under an optical microscope. The pictures were analyzed by finding circles using a circular Hough transform (`imfindcircles` function in MATLAB®) to obtain their size distributions from $V_{cured} = \frac{4}{3}\pi R_{cured}^3$. Furthermore, the surface structure and capsule's core were imaged under a scanning electron microscope (SEM). In preparation, the particles and capsules were concentrated by removing the surfactant solution and washed successively with milliQ water and isopropyl alcohol. The solution was poured away after each rinse and the sample was air dried. The particles were then sputtered with gold to enhance sample conductivity for SEM observation.

5.3 Results

5.3.1 Single emulsion droplets

Fig. 5.4A and 5.4B show a typical snapshot of the chip when single-emulsion droplets are produced with $(P_{disp}, P_{cont}) = (9.5, 77.4)$ kPa, where P corresponds to the driving pressure of the respective phase; the subscripts *disp* and *cont* represent disperse and continues phases respectively. As illustrated, the dispersed phase is hydrodynamically focused into a jet that breaks up into droplets in the outlet channel. A DCM volume of 3.5 ml was chosen to ensure that the jet breaks up before the outlet (distance = 19 mm) at the driving pressures tested. We note that the higher the DCM concentration, the earlier the jet breaks up. The reason is that a lower DCM concentration has a higher viscosity, which dampens the growth of the instability thereby delaying jet breakup [106]. We measured the size distribution of the droplets on the chip and the probability density function (PDF) is plotted in Fig. 5.4C, together with a Gaussian fit. Note that sometimes much smaller satellite droplets were formed but these were not detected in the on-chip images due to their low

contrast. In this configuration, $R_{drop} = 205 \pm 19\,\mu$m and the production rate was 110 droplets/s.

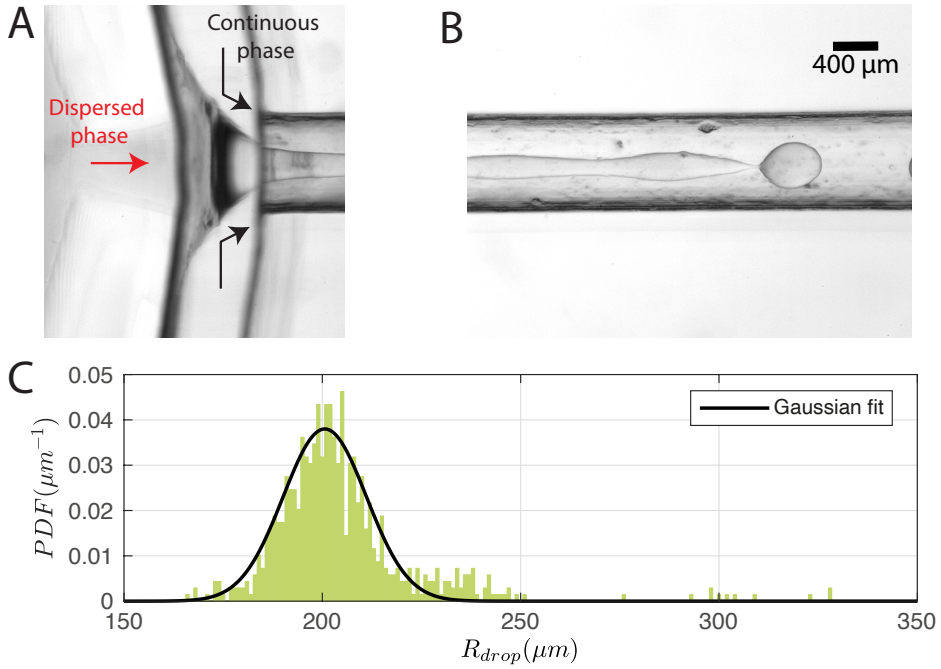

Figure 5.4: Snapshot of A) the junction and B) the jet breaking up inside the chip when producing single-emulsion droplets with $(P_{disp}, P_{cont}) = (9.5, 77.4)$ kPa. C) Measured on-chip droplet size distribution and corresponding Gaussian fit.

For gain a first impression of the range of droplets that the chip can produce, P_{cont} was fixed at 77.3± 0.1 kPa and P_{disp} was varied from 8.5 kPa to 15.5 kPa. Plotting R_{drop} against P_{disp}/P_{cont} in Fig. 5.5A indicates that the chip is able to produce droplets with a size range from 180 μm up to 278 μm in radius for the tested values of P_{cont}. In general, R_{drop} increases with increasing P_{disp}. Assuming that the driving pressure P is directly proportional to the flow rate q as in Poiseuille flows, this increase is linear as predicted by the theory of Guerrero et al. (2020) [106]:

$$\frac{R_{drop}}{R_{tip}} = \left(\frac{3K^*}{4}\right)^{1/3} \sqrt{\frac{q_{disp}}{q_{disp} + q_{cont}}} \tag{5.1}$$

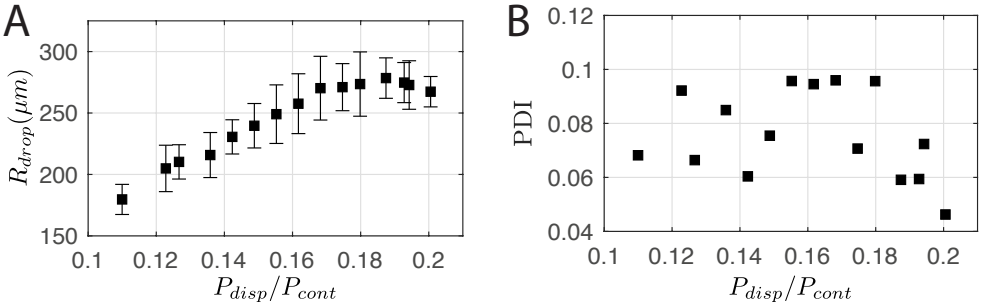

Figure 5.5: A) Droplet radius and B) polydispersity index over a range of dispersed phase pressures P_{disp}. P_{cont} was constant at 77.3± 0.1 kPa.

where R_{tip} is the radius of the dispersed phase channel and K^* is a parameter that depends on the fastest growing mode of the Rayleigh–Plateau instability. At the largest values of P_{disp}, the curve plateaus. In this region, the droplet begins to attain a bullet shape and its width no longer increases with P_{disp}, presumably because it is now constrained by the presence of the continuous phase. The jet breaks up close to the outlet and its pinch-off location moves back and forth in time. Note that the minimum R_{drop} can be further reduced by extending the outlet channel and operating at higher P_{cont}, at the cost of higher chemical throughput.

The polydispersity index (PDI) — defined as the ratio between the standard deviation to the mean value of R_{drop} — is shown in Fig. 5.5B, and ranges from 0.04 to 0.1. For comparison, Donvito et al. (2015) [100] reported a PDI between 0.023 and 0.063 for a 3D-printed T-junction droplet generator. The slightly lower PDI achieved by Donvito et al. (2015) [100] may be due to their operation of the T-junction chip in the squeezing regime with a lower droplet production rate. The squeezing regime in a T-junction chip [107] is comparable to the dripping regime in a flow-focusing junction [94], where the droplet has a low production rate and a diameter comparable to the channel width, hence a lower PDI, *cf.* higher monodispersity.

5.3.2 Particles collection

To produce particles, the droplets generated have to be cured. For this purpose, the dispersed phase mixture was kept the same as in Section 5.3.1 and the droplets were produced at $(P_{disp}, P_{cont}) = (13.9, 77.4)$ kPa. The produc-

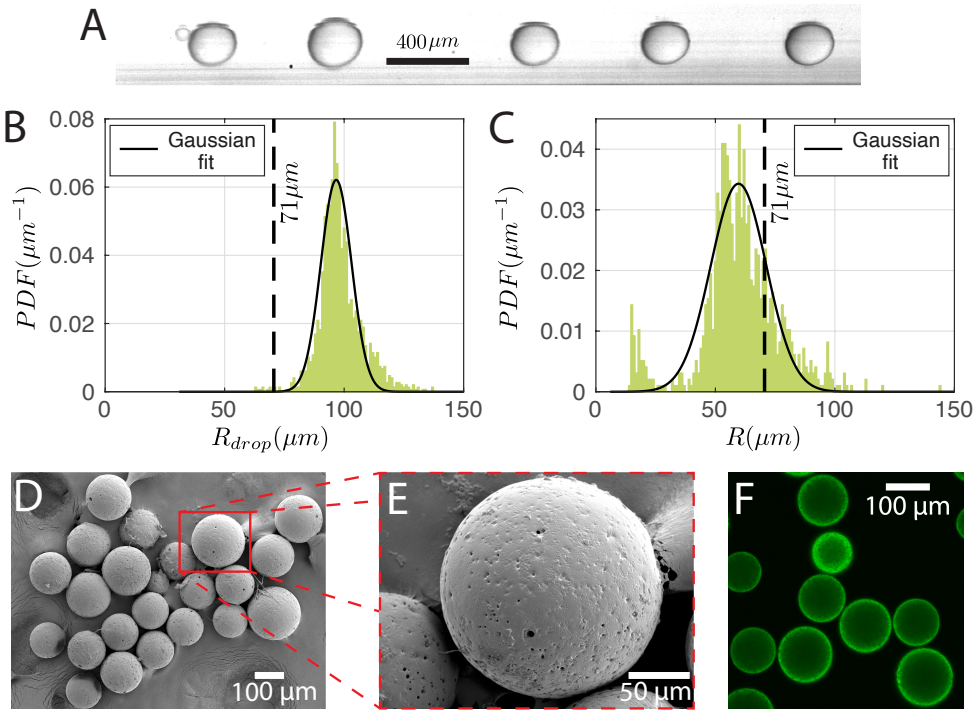

Figure 5.6: A) Image of the droplets in the chip before curing. Size distribution of B) the droplets in the chip and C) the cured particles with their Gaussian fits. D) SEM image of the particles and E) a zoomed image of a single particle. (F) Fluorescent image taken with confocal microscopy. The dashed lines in (B) and (C) indicate the calculated particle size assuming complete solvent evaporation.

tion rate was 350 droplets/s. A snapshot of the droplets in the chip and the corresponding size distribution are shown in Fig. 5.6A and 5.6B, respectively. R_{drop} was $98 \pm 9\,\mu$m. Cured droplets are observed under SEM demonstrating mono-sizes with spherical shapes as can be seen in Fig. 5.6D which shows their population and Fig. 5.6E shows a zoomed image of a single particle. The particles are also imaged with a confocal microscope to demonstrate their ability to fluoresce (Fig. 5.6F). Fig. 5.6C displays the size distribution of the cured particles (with a cut-off radius of 14 μm applied for circle detection). The particle radius was $60 \pm 17\,\mu$m. With $R_{drop} = 98 \pm 9\,\mu$m and a solvent volumetric concentration of 63% (59% DCM and 4% BU), the average particle radius R would have been reduced to $71\,\mu$m upon complete solvent evaporation. The difference between the estimated and observed sizes may be due to variation of the droplet radius over time (Fig. 5.6B is from a 0.9-s recording while Fig. 5.6C is from a sample of droplets collected over $\sim 3\,$min) and uncertainties in on-chip sizing. We note that there is a secondary peak at small particle sizes in Fig. 5.6C. This is due to satellite droplets (see leftmost droplet of Fig. 5.6A) which were not evaluated during on-chip sizing.

5.3.3 Double emulsion droplets

A typical image of the double co-flow nozzle with all three phases present is shown in Fig. 5.7A. In the outlet channel, the coaxial jet pinches off into double-emulsion droplets, as shown in Fig. 5.7B. The volume of dichloromethane was reduced to 2.5 ml, 1 ml lower the single emulsion droplet. With a volume of 2.42 ml of dissolved material, resulting in a DCM-to-solution ratio of 51 % (V/V). At this concentration, the shell phase forms a stable jet that does not destabilize between the first and second co-flows. On the other hand, it does break up due to the Rayleigh-Pleateau instability of the second coflow, forming double emulsion droplets. In the case depicted, 625 droplets/s are generated under driving pressures of 75.4 kPa, 60.3 kPa, and 69.9 kPa for the continuous phase (P_{cont}), shell phase (P_{shell}), and core phase (P_{core}), respectively. The subscripts *shell* and *core* represent shell and core phases, respectively. Note that the production rate typically varies with droplet size and can be increased by operating the chip at higher pressures. We chose to operate at these pressures to conserve chemicals since it takes ≈ 30 min to empty the 1-litre container for the continuous phase. The size distributions of the droplets, cores, and shells are shown in the bar plots of Fig. 5.7C. For this case, $R_{drop} = 240 \pm 13$ μm, $R_{core} = 214 \pm 18$ μm, and $e_{shell} = 25 \pm 13\,\mu$m. The variations in droplet size is due to pressure fluctuations, which slightly

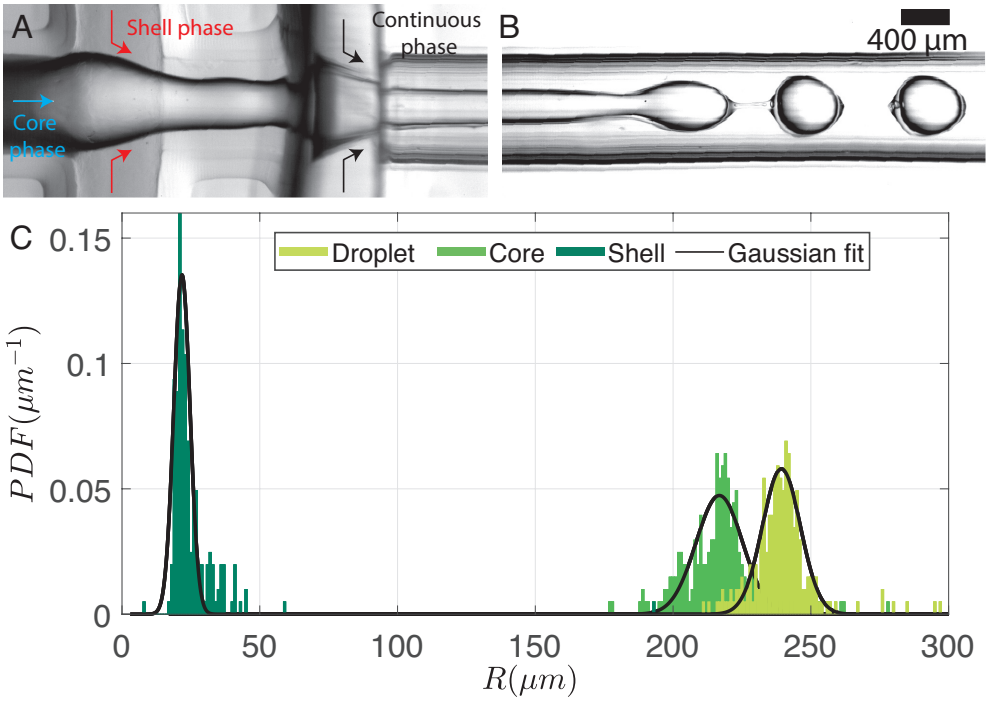

Figure 5.7: A) Images showing the three-phase junction with the introduction of continuous, shell (DCM volumetric concentration = 51 %), and dispersed phases. B) Snapshots illustrating the resulting coaxial jet breaking into encapsulated droplets. C) Size distribution of the droplet radius, core radius, and shell thickness of the samples depicted in (A-B).

changes the length of the jet.

Figure 5.8A illustrates the variation in droplet size for a constant continuous phase pressure of $P_{cont} = 75.4 \pm 0.2$ kPa, while changing the ratio of core to shell phase pressures. The resulting change in core-to-droplet volume fraction is shown in Fig. 5.8B. The colors of the markers in the plot correspond to different shell phase pressures. At $P_{shell} = 60$ kPa, a stable production regime is observed between $0.9 \leq P_{core}/P_{shell} \leq 1.15$. In this range, increasing P_{core} increases the droplet sizes from 260 μm to 290 μm. Consequently, the core-to-droplet volume fraction increases from 0.5 to 0.6. Expectedly, increasing the pressure of the dispersed phase increases both the overall size and core volume. However, when $(P_{core}/P_{shell}) \approx 1$, both the overall size and the volume

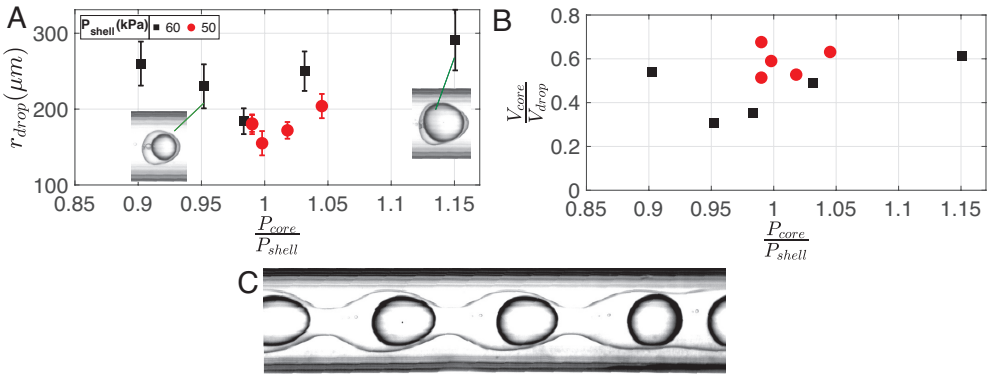

Figure 5.8: Variation of A) doplet size and (B) core-to-shell volume fraction due to changes in core and shell phase pressures indicated in the legend. The marker colors correspond to different shell phase pressures. C) Coaxial jet behavior above the maximum operating shell phase pressure, where core droplets are formed, but the coaxial jet does not break up inside the channel. $P_{cont} = 75.4$ kPa is kept constant.

fraction reached a minimum corresponding to 184 μm and 0.35 respectively. The trend continues at a reduced operating pressure of shell phase $P_{shell} = 50$ kPa (red circles). Further investigations into the pressure drop across the junctions while producing droplets would provide additional insights into this phenomenon, but it is beyond the scope of the current study. Below a certain minimum operating pressure ratio, there is insufficient inertia in the dispersed phase to sustain the flow resulting in irregular sizes and, occasionally, a separation of the shell and core phases. Above a maximum operating pressure ratio, core droplets are formed, but the coaxial jet does not break up within the channel (Fig. 5.8C).

5.3.4 Capsules collection

To keep the core liquid entrapped in the shell during the solidification of the capsules requires rapid cross-linking and fast solvent evaporation. To achieve this, a preheating coil is utilized to initiate the curing reaction before the sample is collected in the beaker. As the polymer cures it facilitates polymer and solvent separation. Additionally, to accelerate solvent evaporation the volume of DCM is decreased to 1.5 ml, 2 ml lower than the DCM used for

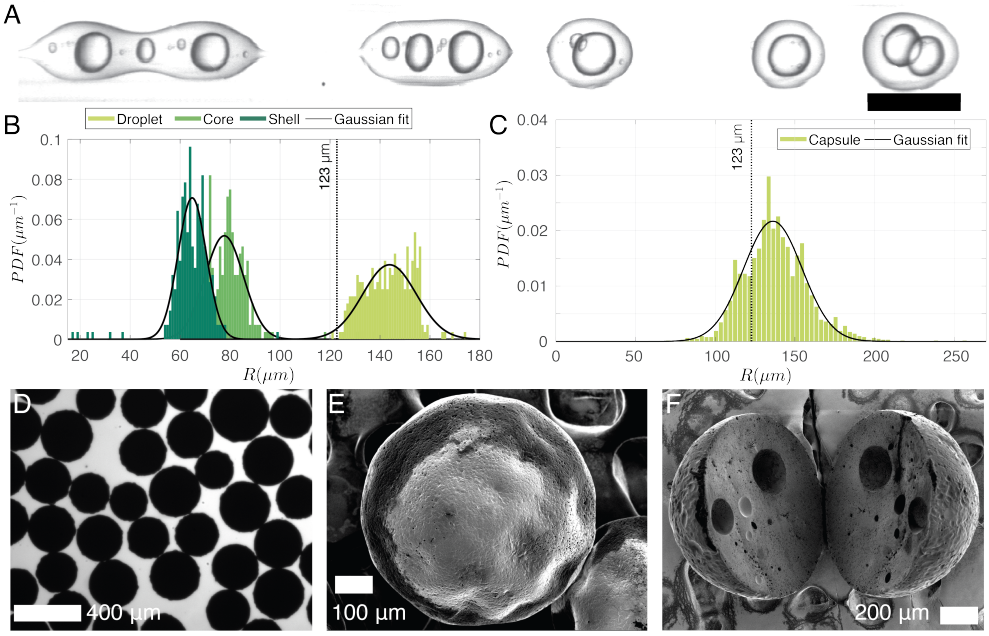

Figure 5.9: A) Illustration of a typical jet breakup with a DCM volume concentration of 38% and small core volume (R_{core} 79 $\pm$ 10 μm). B) On-chip size distribution of the uncured droplets in (A), and C) optical sizing of the cured droplets corresponding to the case depicted in (A). D) A sample of the cured capsules under an optical microscope. E) scanning electron microscope image of a capsule and (F) sliced capsules showing the encapsulation of multiple cores. The dotted lines in (B) and (C) indicate the estimated capsule size assuming complete solvent evaporation.

particles. It results in a DCM-to-solution ratio of 38 % (V/V). This reduction directly influences droplet production, as is evidenced in Fig. 5.9A, where the increased viscosity of the shell phase leads to the formation of double, triple, and quadruple emulsions at (P_{cont}, P_{core}, P_{shell}) = (77.4, 60.1, 77.6) kPa. As a rough estimate, 50% of the droplet population contains double emulsion droplets. The on-chip droplet size distribution (limited to double emulsions) is plotted in Fig. 5.9B and shows that the mean core radius is notably smaller (79 ± 10 μm) than in Fig. 5.7 where a higher concentration of DCM was used, while the overall droplet size and shell thickness are 143 ± 10 μm and 64 ± 8 μm, respectively. Note that higher-order emulsions can be eliminated by increasing P_{core}/P_{shell}, although the range of achievable shell thicknesses remains limited as the increased shell phase viscosity makes it challenging for the jet to break up within the channel. Nonetheless, a smaller core (thicker shell) has the advantage of remaining encapsulated as it minimizes the likelihood of the core escape due to liquid shell rupture. After the capsules are cured, they are imaged under an optical microscope (Fig. 5.9D), and their size distribution is shown in Fig. 5.9C. Assuming that all solvent in the shell phase (38% DCM and 6% BU totaling 44% solvent-to-solution ratio (V/V)) evaporates, the expected capsule size will be 123 μm (dotted line in Fig. 5.9(B-C)). However, if the shell ruptures and the core dissolves in the continuous phase, the resulting particle size would be around 111 μm. Considering a 10 % error in optical sizing, these estimates are quite close to the measured size of 138 ± 21 μm. A scanning electron microscope image of a typical capsule with a radius of ∼200 μm is shown in Fig. 5.9E. It is larger than our predicted size (123 μm) and is likely to have an encapsulated core. Within the same size range, Fig. 5.9F displays a sliced capsule demonstrating multiple encapsulated cores that are most likely as a result of the curing of a double of higher-order core droplet.

5.4 Limitations

3D printing is advantageous for its benefits of rapid prototyping and high chemical resistance with several organic mediums. However, channels that are in direct contact with dichloromethane for an extended period of time lead to deformation. Fig. 5.10A and 5.10B show that the channel between the two junctions deforms from a cylindrical to a diverging profile over time. Note that it returns to the original cylindrical profile in ∼ 12 h of inactivity. The deformation changes the operating regime. For instance, the size of the

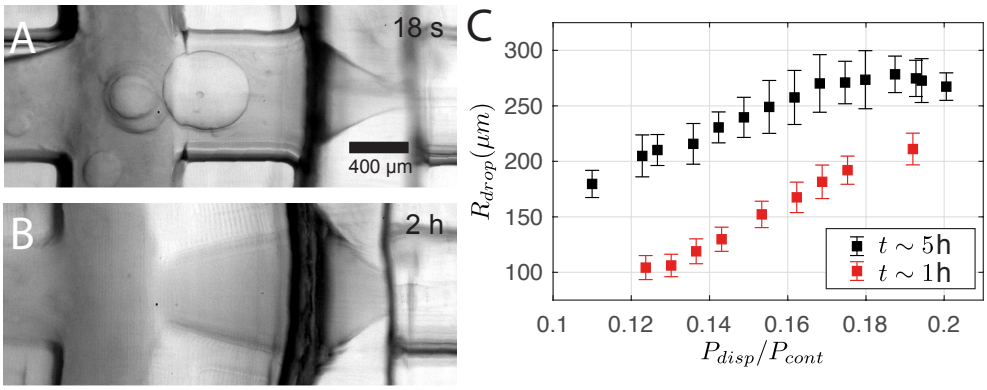

Figure 5.10: A-B) Deformation of the junction region of the chip that deforms under ac3on of direct contact with the shell phase as deformation occurs. C) Single-emulsion droplet radius R_{drop} at different P_{disp}/P_{cont} generated at different times t of 1 hour and 5 hours of operation.

droplets increases with time as shown in Fig. 5.10C, where the single-emulsion droplet radius R_{drop} is plotted against P_{disp}/P_{cont} while being measured at two time points t at 1 hour and 5 hours of operation. We stress that the difference in R_{drop} cannot be attributed to fluctuations in P_{cont} as P_{cout} was 0.4 kPa higher at $t \sim 5$ h. This deformation also explains the measurable change of R_{drop} between Secs. 5.3.1 and 5.3.2 despite the similar control parameters. For the droplet cases presented in Secs. 5.3.1 and 5.3.3, the chip was deformed for more than 1 hour of operation before the experiments started.

5.5 Conclusion

A three-dimensional millifluidic chip design is presented with two flow-focusing junctions that can be easily manufactured using a 3D printer. The chip can produce both single and double-emulsion microdroplets depending on the inlet configuration. Droplet production occurs by coflow, which causes jet breakup via a Rayleigh–Plateau instability. Using a mixture of dichloromethane, epoxy resin, melamine crosslinker, and dinonylnaphthalenedisulfonic acid, the chip produces monodispersed droplets with sizes $\sim O(100)\mu$m. Operating at low driving pressures, we measured that the production rate in the jetting regime is around 100 Hz and 600 Hz for single and double emulsion droplets, respec-

tively. By varying the core phase driving pressure, a large range of droplet sizes and shell thicknesses can be obtained. The overall size for single emulsion droplets increases with increasing dispersed phase pressure. In the case of double emulsion droplets, the droplet size reaches a minimum before increasing with increasing core phase pressure, while maintaining a constant shell phase pressure. By heating the suspended droplets at 40°C for 4 hours, the droplets were cured into either particles or capsules.

Acknowledgements

M.S. Saleem thanks A. Hermes from Allnex for providing technical guidance and the melamine resin samples for this research. Additionally, M.S. Saleem is grateful to S. Ma, J. Liu, and T. de Boer from PPG Industries for supplying epoxy samples and offering technical expertise. The authors would like to thank T. Segers, D. van Buuren, and B. van Elburg for useful discussions as well as P. Dekker for operating the confocal microscope. M.S. Saleem acknowledges funding from the Dutch Research Council grant (Veni AES 2018 - 16879). T.T.K. Chan and D. Krug have received funding from the European Research Council (ERC) under the European Union's Horizon 2020 research and innovation programme (grant agreement No. 950111, BU-PACT). G. Lajoinie acknowledges funding from the European Research Council (ERC-2022-STG Super-692 FALCON, No. 101076844).

Chapter 6

Conclusions and outlook

In this thesis, we have studied the dissolution and vaporization dynamics of liquid precursors for application in intumescent coatings. First, we have established a semi-analytical model and numerically solved it to systematically study the vaporization of droplets with a range of sizes, as a function of the ambient temperature. Next, we have explored the dynamics of superheated droplets-in-oil experimentally and adapted the model with sheet retraction dynamics. We have then explored the effect of the shell on the dissolution and vaporization of the encapsulated core. Finally, we have developed a 3D millifluidics chip capable of producing single and double emulsion microdroplets made of a curable material.

6.1 Conclusion

Chapter 2 introduces a model to describe the vaporization dynamics of superheated water-in-oil droplets by accounting for bubble dynamics, phase change, and heat transfer. The numerical solution of our model shows that both droplet size and the degree of superheat are key to describing the growth of the vapor bubble, which is limited by either inertia or thermal diffusion. Analytical models, i.e. Rayleigh and Plesset-Zwick, describing these vaporization phenomena are valid only for the vaporization of millimetric droplets at a low degree of superheat. We further study the influence of the thermal properties of the system: phase change enthalpy was found to be crucial for the determination of the dominant mechanism, while thermal diffusivity of the heating medium is significant only at low temperatures where vaporization relies on heat diffusion from the surrounding liquid. Finally, post-vaporization bubbles

oscillate at the Minnaert resonance frequency, with an inverse relationship to size ($f_M \sim 1/R_b$) and with a magnitude depending on the potential energy stored in the system at the time of complete vaporization, and thus on the bath temperature.

In Chapter 3, we study experimentally the dissolution and vaporization of microdroplets gradually heated in an oil bath. We discover that a transition region exists where microdroplets can dissolve completely or vaporize after some dissolution. The entire dissolution process is divided into two stages. First, the microdroplets dissolve slowly following the Epstein-Plesset dissolution law ($(1-\frac{R^2}{R_d^2}) \sim t$). Then around 90 ^oC a transition to a rapid dissolution phase occurs, where the dissolution takes a semiempirical form $(1-\frac{R^2}{R_d^2}) \sim t^{6.5}$. Upon vaporization, the expanding bubble transforms the vaporizing droplet into a sheet which subsequently retracts and stalls the phase change. The model of Chapter 2 is therefore adapted to account for the dynamics of sheet retraction, where the time scale of retraction is found to be dominant over the inertial or thermal diffusive growth.

Chapter 4 explores the influence of a shell, composed of polylactic acid and nanoparticle, on both the dissolution and vaporization of encapsulated droplets, or microcapsules, when exposed to a slow-heating ramp. We observe that in the case of microcapsules, the transition from slow dissolution towards rapid dissolution is delayed until the bath reaches the polymer melting temperature (150 $^\circ C$). Beyond this, the capsule experiences the accelerated dissolution behavior observed before for microdroplets. To describe this phenomenon, we developed an Epstein-Plesset-type model that considers a linear increase in saturation concentration at the interface with temperature. The shell shields the core against vaporization nuclei present in the host liquid, resulting in a decrease in the vaporization probability. The growth of a vapor bubble from a capsule with a melted shell is comparable to that of a bubble originating from a droplet. In both cases, the timescale of sheet retraction controls the vaporization process.

Finally, in Chapter 5, we develop a flow-focusing 3D milifluidics chip and additively manufacture it to produce microdroplets. It utilizes the Rayleigh-Plateau instability to form either from single or double emulsion droplets at low driving pressures with sizes $\sim O(100)\mu$m. The size of the single emulsion droplet increases with the driving pressure of the dispersed phase. When producing a double emulsion, droplet size exhibits a minimum as a function of core phase pressure P_{core} (when keeping constant shell phase pressure P_{shell}). Droplet size and shell thickness are tuned by varying pressure ratio

(P_{core}/P_{shell}). The chip is versatile in its ability to produce complex emulsions which are then cured into particles or capsules.

6.2 Outlook

The work carried out in this thesis lays the foundation for using microcapsules as a blowing agent for intumescent coatings. We have explored the problem on the microscale. Research on an individual droplet/capsule revealed a critical size range below which both microdroplets and microcapsules will not nucleate due to accelerated dissolution. The population of capsules embedded in the coating presented in the introduction falls under dissolution-dominated sizes. Nucleated droplets/capsules also face limited vaporization due to sheet retraction-dominated growth. Both dissolution and vaporization aspects are far from the classical predictions for these problems. Fig. 6.1A shows a comparison of the Epstein-Plesset dissolution model with the model developed in the present study accounting for a linear increase of saturation concentration with temperature. Fig. 6.1B shows a comparison of thermal diffusion-limited and sheet retraction-limited vaporization. In both cases, accompanying experimental measurement shows the overestimation of classical predictions. Finally, we develop a 3D milifluidics device that can produce droplet sizes of complex

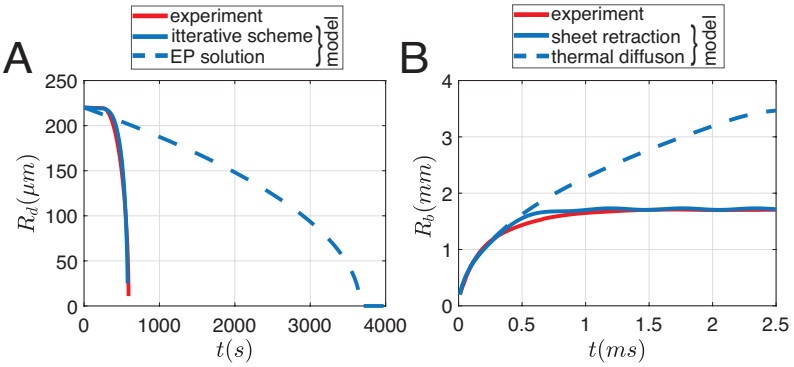

Figure 6.1: Evolution of dissolution and vaporization models utilized in the thesis. A. Dissolution curve of 220 μm droplet in oleic acid subjected to a 0.4 $\frac{K}{s}$ temperature ramp. The initial temperature is 310 K and the ramp starts at $t \approx 250$ s. B. Vaporization curve of a 318 μm droplet in oleic acid subjected to a 0.4 $\frac{K}{s}$ temperature ramp.

materials that are required for intumescent applications. There are, however, still several questions to address on the route to practical implementation as discussed below.

6.2.1 Dissolution and vaporization

Accelerated dissolution observed for both microdroplets (Chapter 3) and capsules (Chapter 4) is described using power law-based adaption of the Epstien-Plesset equation. Our developed Epstien-Plesset-type model of Chapter 4 accounts for a linear increase in the saturation concentration with increasing temperature. More realistic data on the dependence of saturation concentration as a function of temperature will further aid our understanding of this accelerated dissolution process.
The vaporization model developed in Chapter 1 was later adopted for film retraction based on experimental observation and is validated for the vaporization of both microdroplets (Chapter 3) and microcapsules (Chapter 4). Utilizing temperature as a fitting parameter remains a limitation. It could potentially embody the uncertainty in local temperature, or a missing thermodynamic component, and therefore requires further investigation.

6.2.2 Suspension and multiscale study

Furthermore, capsule-capsule interactions are a crucial next step toward translating our understanding of capsule vaporization from the microscale to the macroscale expansion of a coating. Studying the influence of neighboring capsules is significant for both dissolution and vaporization. Dissolution will be influenced/reduced by the surrounding concentration gradient, which would now be coupled to the dissolution of other surrounding capsules. A reduced dissolution also increases the vaporization probability. Neighboring capsules would also limit the thermal energy available as it now must be shared. Additionally, multiscale modeling with a crystalline arrangement of capsules from initially two to several thousand would thus be crucial to optimize the overall expansion behavior of the coating.

6.2.3 Capsule design and composition

The recent introduction of melamine, a key ingredient of present fire-protective coatings, into the list of carcinogenic materials by the European Union, has disrupted the market of intumescent coatings and creates opportunities to look

for new eco-friendly blowing agents. Utilizing microcapsules with a water-based core and a melamine-based shell as a source of intumescence already significantly reduces the amount of melamine needed for the coating. Capsules developed in Chapter 5 have a core radius of 79 μm, which would typically result in a pure dissolution as observed in Chapters 3 and 4. Encapsulation of droplets with a larger core radius was not tested and is also limited by the slow gelling time. The polylactic acid (PLA)–based microcapsules studied in Chapter 4 encapsulate in a larger core volume. However, the shell needs to be highly hydrophobic to resist water diffusion. Additionally, embedding capsules in an intumescent coating requires a shell with sufficient mechanical strength to endure mixing or agitation while being integrated into a resin. A core that is in solid form at room temperature, such as hexadecane, would provide a much-improved shelf life of the agent and increase its long-term stability. However, such an oil-based material is extremely flammable, and further research in finding a suitable core will also be a good step.

6.2.4 Coating design and stability

The new coating requires specific properties for controlled intumescence. The thermal response of resin needs synchronization with that of capsules. The solid coat should melt as capsules activate upon heating. The resin should be hydrophobic to prevent mass diffusion through the structure, thereby increasing the vaporization probability. Ideally, a shear-thickening polymer prevents bubble coalescence during the intumescence process.

References

[1] S. Hall and B. Evarts, "Fire loss in the united states during 2021", National Fire Protection Association (NFPA) (2022).

[2] "www.telegraph.co.uk/news/2017/06/14/grenfell-tower-inferno-disaster-waiting-happen-concerns-raised", Website .

[3] "https://www.wb-sg.com/projects/myzeil/", Website .

[4] G. MacLeod, "The grenfell tower atrocity: Exposing urban worlds of inequality, injustice, and an impaired democracy", City **22**, 460–489 (2018).

[5] R. Prior, "The entire wooden interior of notre dame cathedral has been lost", (2019).

[6] K. Mróz, I. Hager, and K. Korniejenko, "Material solutions for passive fire protection of buildings and structures and their performances testing", Procedia Engineering **151**, 284–291 (2016).

[7] R. G. Puri and A. Khanna, "Intumescent coatings: A review on recent progress", Journal of Coatings Technology and Research **14**, 1–20 (2017).

[8] "https://www.ddcoatings.co.uk/intumescent-fire-protection-painting", Website .

[9] G. Okyay, F. Samyn, M. Jimenez, and S. Bourbigot, "A facile technique to extract the cross-sectional structure of brittle porous chars from intumescent coatings", Polymers **11**, 640 (2019).

[10] J. Alongi, Z. Han, and S. Bourbigot, "Intumescence: Tradition versus novelty. a comprehensive review", Progress in Polymer Science **51**, 28–73 (2015).

[11] C. Sui, J. A. Preece, S.-H. Yu, and Z. Zhang, "Novel encapsulation of water soluble inorganic or organic ingredients in melamine formaldehyde microcapsules to achieve their sustained release in an aqueous environment", RSC advances **8**, 29495–29498 (2018).

[12] R. Letan and E. Kehat, "The mechanism of heat transfer in a spray column heat exchanger", AIChE Journal **14**, 398–405 (1968).

[13] W. L. McCabe, J. C. Smith, and P. Harriott, *Unit operations of chemical engineering*, volume 5 (McGraw-hill New York) (1993).

[14] E. Can and A. Prosperetti, "A level set method for vapor bubble dynamics", Journal of Computational Physics **231**, 1533–1552 (2012).

[15] E. Ory, H. Yuan, A. Prosperetti, S. Popinet, and S. Zaleski, "Growth and collapse of a vapor bubble in a narrow tube", Physics of Fluids **12**, 1268–1277 (2000).

[16] H. S. Lee and H. Merte Jr, "Spherical vapor bubble growth in uniformly superheated liquids", International Journal of Heat and Mass Transfer **39**, 2427–2447 (1996).

[17] P. Dergarabedian, "The rate of growth of vapor bubbles in superheated water", Journal of Applied Mechanics **20**, 537–545 (2021).

[18] P. Kosky, "Bubble growth measurements in uniformly superheated liquids", Chemical Engineering Science **23**, 695–706 (1968).

[19] L. Florschuetz, C. Henry, and A. R. Khan, "Growth rates of free vapor bubbles in liquids at uniform superheats under normal and zero gravity conditions", International Journal of Heat and Mass Transfer **12**, 1465–1489 (1969).

[20] L. Rayleigh, "On the pressure developed in a liquid during the collapse of a spherical cavity", Philosophical Magazine **6**, 94–98 (1917).

[21] M. S. Plesset and S. A. Zwick, "The growth of vapor bubbles in superheated liquids", Journal of Applied Physics **25**, 493–500 (1954).

[22] A. Chernov, A. Pil'nik, I. Vladyko, and S. Lezhnin, "New semi-analytical solution of the problem of vapor bubble growth in superheated liquid", Scientific Reports **10**, 16526 (2020).

[23] S. Sideman and Y. Taitel, "Direct-contact heat transfer with change of phase: evaporation of drops in an immiscible liquid medium", International Journal of Heat and Mass Transfer **7**, 1273–1289 (1964).

[24] Y. Tochitani, Y. Mori, and K. Komotori, "Vaporization of single liquid drops in an immiscible liquid part i: Forms and motions of vaporizing drops", Wärme-und Stoffübertragung **10**, 51–59 (1977).

[25] Y. Tochitani, T. Nakagawa, Y. Mori, and K. Komotori, "Vaporization of single liquid drops in an immiscible liquid part ii: Heat transfer characteristics", Wärme-und Stoffübertragung **10**, 71–79 (1977).

[26] G. Lajoinie, E. Gelderblom, C. Chlon, M. Böhmer, W. Steenbergen, N. De Jong, S. Manohar, and M. Versluis, "Ultrafast vapourization dynamics of laser-activated polymeric microcapsules", Nature Communications **5**, 3671 (2014).

[27] G. Lajoinie, M. Visscher, E. Blazejewski, G. Veldhuis, and M. Versluis, "Three-phase vaporization theory for laser-activated microcapsules", Photoacoustics **19**, 100185 (2020).

[28] C. Avedisian and K. Suresh, "Analysis of non-explosive bubble growth within a superheated liquid droplet suspended in an immiscible liquid", Chemical Engineering Science **40**, 2249–2259 (1985).

[29] M. Roesle and F. Kulacki, "Boiling of small droplets", International Journal of Heat and Mass Transfer **53**, 5587–5595 (2010).

[30] T. S. Emery, P. A. Raghupathi, and S. G. Kandlikar, "Bubble growth inside an evaporating liquid droplet introduced in an immiscible superheated liquid", International Journal of Heat and Mass Transfer **127**, 313–321 (2018).

[31] M. S. Plesset, "The dynamics of cavitation bubbles", Journal of Applied Mechanics **16**, 277–282 (2021).

[32] M. C. Antoine, "Nouvelle relation entre les tensions et les temperatures", Comptes Rendus des Séances de l'Académie des Sciences **107**, 681–684 (1888).

[33] "https://webbook.nist.gov", Website .

[34] "https://materials.springer.com/lb/docs/sm_lbs_978-3-540-69409-0_2", Website .

[35] B. Mikic, W. Rohsenow, and P. Griffith, "On bubble growth rates", International Journal of Heat and Mass Transfer **13**, 657–666 (1970).

[36] M. Versluis, E. Stride, G. Lajoinie, B. Dollet, and T. Segers, "Ultrasound contrast agent modeling: a review", Ultrasound in Medicine & Biology **46**, 2117–2144 (2020).

[37] A. Prosperetti, "Vapor bubbles", Annual Review of Fluid Mechanics **49**, 221–248 (2017).

[38] A. Prosperetti, "Thermal effects and damping mechanisms in the forced radial oscillations of gas bubbles in liquids", The Journal of the Acoustical Society of America **61**, 17–27 (1977).

[39] F. Caupin and E. Herbert, "Cavitation in water: a review", Comptes Rendus Physique **7**, 1000–1017 (2006).

[40] Y. Wang, M. E. Zaytsev, G. Lajoinie, H. L. The, J. C. Eijkel, A. van den Berg, M. Versluis, B. M. Weckhuysen, X. Zhang, H. J. Zandvliet, and D. Lohse, "Giant and explosive plasmonic bubbles by delayed nucleation", Proceedings of the National Academy of Sciences **115**, 7676–7681 (2018).

[41] D. Lohse, "Bubble puzzles: from fundamentals to applications", Physical Review Fluids **3**, 110504 (2018).

[42] S. Karthika, T. Radhakrishnan, and P. Kalaichelvi, "A review of classical and nonclassical nucleation theories", Crystal Growth & Design **16**, 6663–6681 (2016).

[43] A. Battaglia, J. M. de Moor, A. Aiuppa, G. Avard, H. Bakkar, M. Bitetto, M. M. Mora Fernández, P. Kelly, G. Giudice, D. Delle Donne, and H. Villalobos, "Insights into the mechanisms of phreatic eruptions from continuous high frequency volcanic gas monitoring: Rincón de la vieja volcano, costa rica", Frontiers in Earth Science **6**, 247 (2019).

[44] C. Zhao, Y. Xie, Z. Mao, Y. Zhao, J. Rufo, S. Yang, F. Guo, J. D. Mai, and T. J. Huang, "Theory and experiment on particle trapping and manipulation via optothermally generated bubbles", Lab on a Chip **14**, 384–391 (2014).

[45] G. Lajoinie, T. van Rooij, I. Skachkov, E. Blazejewski, G. Veldhuis, N. de Jong, K. Kooiman, and M. Versluis, "Laser-activated polymeric microcapsules for ultrasound imaging and therapy: in vitro feasibility", Biophysical Journal **112**, 1894–1907 (2017).

[46] M. Visscher, G. Lajoinie, E. Blazejewski, G. Veldhuis, and M. Versluis, "Laser-activated microparticles for multimodal imaging: ultrasound and photoacoustics", Physics in Medicine & Biology **64**, 034001 (2019).

[47] H. Wakeshima and K. Takata, "On the limit of superheat", Journal of the Physical Society of Japan **13**, 1398–1403 (1958).

[48] G. R. Moore, "Vaporization of superheated drops in liquids", AIChE Journal **5**, 458–466 (1959).

[49] T. J. Jarvis, M. D. Donohue, and J. L. Katz, "Bubble nucleation mechanisms of liquid droplets superheated in other liquids", Journal of Colloid and Interface Science **50**, 359–368 (1975).

[50] J. Shepherd and B. Sturtevant, "Rapid evaporation at the superheat limit", Journal of Fluid Mechanics **121**, 379–402 (1982).

[51] B. Sturtevant and J. Shepherd, "Evaporative instability at the superheat limit", Applied Scientific Research **38**, 85–97 (1982).

[52] M. A. van Limbeek, H. Lhuissier, A. Prosperetti, C. Sun, and D. Lohse, "Explosive boiling?", Physics of Fluids **25**, 091102 (2013).

[53] C. Avedisian and R. Andres, "Bubble nucleation in superheated liquid—liquid emulsions", Journal of Colloid and Interface Science **64**, 438–453 (1978).

[54] P. S. Epstein and M. S. Plesset, "On the stability of gas bubbles in liquid-gas solutions", The Journal of Chemical Physics **18**, 1505–1509 (1950).

[55] J. M. Zhang, Y. Chen, D. Lohse, and A. Marin, "Dissolution of microdroplets in a sparsely miscible liquid confined by leaky walls", Journal of Fluid Mechanics **912**, A34 (2021).

[56] M. S. Saleem, M. Versluis, and G. Lajoinie, "Vaporization dynamics of a super-heated water-in-oil droplet: modeling and numerical solution", (2024).

[57] A. Mata, A. J. Fleischman, and S. Roy, "Characterization of polydimethylsiloxane (PDMS) properties for biomedical micro/nanosystems", Biomedical Microdevices **7**, 281–293 (2005).

[58] M. Blander, D. Hengstenberg, and J. L. Katz, "Bubble nucleation in n-pentane, n-hexane and n-pentane+ hexadecane mixtures and water", The Journal of Physical Chemistry **75**, 3613–3619 (1971).

[59] V. Sanjay, U. Sen, P. Kant, and D. Lohse, "Taylor–culick retractions and the influence of the surroundings", Journal of Fluid Mechanics **948**, A14 (2022).

[60] D. Sagdeev, I. Gabitov, C. Isyanov, V. Khairutdinov, M. Farakhov, Z. Zaripov, and I. Abdulagatov, "Densities and viscosities of oleic acid at atmospheric pressure", Journal of the American Oil Chemists' Society **96**, 647–662 (2019).

[61] Z. Jian, P. Deng, and M.-J. Thoraval, "Air sheet contraction", Journal of Fluid Mechanics **899**, A7 (2020).

[62] C. E. Brennen, *Cavitation and bubble dynamics* (Cambridge university press) (2014).

[63] D. Lohse and X. Zhang, "Physicochemical hydrodynamics of droplets out of equilibrium", Nature Reviews Physics **2**, 426–443 (2020).

[64] Y.-S. Yu, Z.-Q. Wang, and Y.-P. Zhao, "Experimental study of evaporation of sessile water droplet on polydimethylsiloxane surfaces", Acta Mechanica Sinica **29**, 799–805 (2013).

[65] L. D. Chumpitaz, L. F. Coutinho, and A. J. Meirelles, "Surface tension of fatty acids and triglycerides", Journal of the American Oil Chemists' Society **76**, 379–382 (1999).

[66] M. Singh, K. Hemant, M. Ram, and H. Shivakumar, "Microencapsulation: A promising technique for controlled drug delivery", Research in Pharmaceutical Sciences **5**, 65 (2010).

[67] T. L. Mervosh, E. W. Stoller, F. W. Simmons, T. R. Ellsworth, and G. K. Sims, "Effects of starch encapsulation on clomazone and atrazine movement in soil and clomazone volatilization", Weed Science **43**, 445–453 (1995).

[68] G. Nelson, "Application of microencapsulation in textiles", International Journal of Pharmaceutics **242**, 55–62 (2002).

[69] Y. Long, J. Jiang, C. W. Visser, W. Brilman, and W. Rohlfs, in *Burgers Symposium 2023* (2023).

[70] M. Bruning, M. Costalonga, J. Snoeijer, and A. Marin, "Turning drops into bubbles: cavitation by vapor diffusion through elastic networks", Physical Review Letters **123**, 214501 (2019).

[71] M. S. Saleem, M. Versluis, and G. Lajoinie, "Dissolution and vaporization of a microdroplet of water in oil exposed to a temperature ramp", submitted for publication (2024).

[72] O. R. Enríquez, C. Sun, D. Lohse, A. Prosperetti, and D. Van Der Meer, "The quasi-static growth of CO_2 bubbles", Journal of Fluid Mechanics **741**, R1 (2014).

[73] Á. M. Soto, O. R. Enríquez, A. Prosperetti, D. Lohse, and D. Van Der Meer, "Transition to convection in single bubble diffusive growth", Journal of Fluid Mechanics **871**, 332–349 (2019).

[74] Á. M. Soto, D. Lohse, and D. Van Der Meer, "Diffusive growth of successive bubbles in confinement", Journal of Fluid Mechanics **882**, A6 (2020).

[75] P. B. Duncan and D. Needham, "Microdroplet dissolution into a second-phase solvent using a micropipet technique: Test of the epstein- plesset model for an aniline- water system", Langmuir **22**, 4190–4197 (2006).

[76] D. Lohse and X. Zhang, "Surface nanobubbles and nanodroplets", Reviews of Modern Physics **87**, 981 (2015).

[77] R. Platford, "The octanol-water partitioning of some hydrophobic and hydrophilic compounds", Chemosphere **12**, 1107–1111 (1983).

[78] J. Jiang, A. T. Poortinga, Y. Liao, T. Kamperman, C. H. Venner, and C. W. Visser, "High-throughput fabrication of size-controlled pickering emulsions, colloidosomes, and air-coated particles via clog-free jetting of suspensions", Advanced Materials **35**, 2208894 (2023).

[79] M.-J. Thoraval, Y. Li, and S. T. Thoroddsen, "Vortex-ring-induced large bubble entrainment during drop impact", Physical Review E **93**, 033128 (2016).

[80] J. Westerweel, G. E. Elsinga, and R. J. Adrian, "Particle image velocimetry for complex and turbulent flows", Annual Review of Fluid Mechanics **45**, 409–436 (2013).

[81] A. Schröder and D. Schanz, "3D Lagrangian particle tracking in fluid mechanics", Annual Review of Fluid Mechanics **55**, 511–540 (2023).

[82] A. V. Nguyen and H. J. Schulze, *Colloidal science of flotation*, volume 118 of *Surfactant sciences*, 1st edition (CRC Press, Boca Raton) (2004).

[83] K. Kooiman, M. R. Böhmer, M. Emmer, H. J. Vos, C. Chlon, W. T. Shi, C. S. Hall, S. H. de Winter, K. Schroën, M. Versluis, N. de Jong, and A. van Wamel, "Oil-filled polymer microcapsules for ultrasound-mediated delivery of lipophilic drugs", Journal of Controlled Release **133**, 109–118 (2009).

[84] M. Bhatia, "A review on application of encapsulation in agricultural processes", Encapsulation of Active Molecules and Their Delivery System 131–140 (2020).

[85] D. Jiménez-Arias, S. Morales-Sierra, P. Silva, H. Carrêlo, A. Gonçalves, J. F. T. Ganança, N. Nunes, C. S. Gouveia, S. Alves, J. P. Borges, and Â. A. P. de Carvalho, "Encapsulation with natural polymers to improve the properties of biostimulants in agriculture", Plants **12**, 55 (2022).

[86] S. K. S. Cheng, T. Li, S. S. Meena, Q. Cao, B. Li, B. K. Kosgei, T. Cheng, P. Luo, Q. Liu, G. Zhu, Q. Liu, and R. P. Han, "Advances in microfluidic technologies for energy storage and release systems", Advanced Energy and Sustainability Research **3**, 2200060 (2022).

[87] S. L. Anna, N. Bontoux, and H. A. Stone, "Formation of dispersions using "flow focusing" in microchannels", Applied Physics Letters **82**, 364–366 (2003).

[88] J. M. Zhang, E. Q. Li, A. A. Aguirre-Pablo, and S. T. Thoroddsen, "A simple and low-cost fully 3d-printed non-planar emulsion generator", RSC advances **6**, 2793–2799 (2016).

[89] G. Lajoinie, T. van Rooij, I. Skachkov, E. Blazejewski, G. Veldhuis, N. de Jong, K. Kooiman, and M. Versluis, "Laser-activated polymeric microcapsules for ultrasound imaging and therapy: in vitro feasibility", Biophysical Journal **112**, 1894–1907 (2017).

[90] S. Zhang, K. Wang, and G. Luo, "High-throughput generation of uniform droplets from parallel microchannel droplet generators and the preparation of polystyrene microsphere material", Particuology **77**, 136–145 (2023).

[91] C. W. Visser, T. Kamperman, L. P. Karbaat, D. Lohse, and M. Karperien, "In-air microfluidics enables rapid fabrication of emulsions, suspensions, and 3D modular (bio)materials", Science Advances **4**, eaao1175 (2018).

[92] I. Kobayashi, M. Nakajima, K. Chun, Y. Kikuchi, and H. Fujita, "Silicon array of elongated through-holes for monodisperse emulsion droplets", AIChE Journal **48**, 1639–1644 (2002).

[93] J. K. Nunes, S. S. H. Tsai, J. Wan, and H. A. Stone, "Dripping and jetting in microfluidic multiphase flows applied to particle and fibre synthesis", Journal of Physics D: Applied Physics **46**, 114002 (2013).

[94] E. Castro-Hernández, M. P. Kok, M. Versluis, and D. Fernandez Rivas, "Study of the geometry in a 3D flow-focusing device", Microfluidics and Nanofluidics **20**, 40 (2016).

[95] L. Yobas, S. Martens, W.-L. Ong, and N. Ranganathan, "High-performance flow-focusing geometry for spontaneous generation of monodispersed droplets", Lab on a Chip **6**, 1073–1079 (2006).

[96] R. Amin, S. Knowlton, A. Hart, B. Yenilmez, F. Ghaderinezhad, S. Katebifar, M. Messina, A. Khademhosseini, and S. Tasoglu, "3D-printed microfluidic devices", Biofabrication **8**, 022001 (2016), publisher: IOP Publishing.

[97] A. V. Nielsen, M. J. Beauchamp, G. P. Nordin, and A. T. Woolley, "3D printed microfluidics", Annual Review of Analytical Chemistry **13**, 45–65 (2020).

[98] A. I. Shallan, P. Smejkal, M. Corban, R. M. Guijt, and M. C. Breadmore, "Cost-effective three-dimensional printing of visibly transparent microchips within minutes", Analytical Chemistry **86**, 3124–3130 (2014).

[99] K. C. Bhargava, B. Thompson, and N. Malmstadt, "Discrete elements for 3D microfluidics", Proceedings of the National Academy of Sciences **111**, 15013–15018 (2014).

[100] L. Donvito, L. Galluccio, A. Lombardo, G. Morabito, A. Nicolosi, and M. Reno, "Experimental validation of a simple, low-cost, T-junction droplet generator fabricated through 3D printing", Journal of Micromechanics and Microengineering **25**, 035013 (2015).

[101] A. Dewandre, J. Rivero-Rodriguez, Y. Vitry, B. Sobac, and B. Scheid, "Microfluidic droplet generation based on non-embedded co-flow-focusing using 3D printed nozzle", Scientific Reports **10**, 21616 (2020).

[102] R. Song, M. S. Abbasi, and J. Lee, "Fabrication of 3D printed modular microfluidic system for generating and manipulating complex emulsion droplets", Microfluidics and Nanofluidics **23**, 92 (2019).

[103] A. Loxley and B. Vincent, "Preparation of poly(methylmethacrylate) microcapsules with Liquid Cores", Journal of Colloid and Interface Science **208**, 49–62 (1998).

[104] M. Miezner, S. Shaik, and I. Jacobi, "Custom density fluorescent tracer fabrication via microfluidics", Experiments in Fluids **62**, 88 (2021).

[105] M. S. Saleem, J. Jiang, M. Versluis, C. W. Visser, and G. Lajoinie, "Dissolution and vaporization of a water-filled microcapsule on exposure to a temperature ramp", submitted for publication (2024).

[106] J. Guerrero, Y.-W. Chang, A. A. Fragkopoulos, and A. Fernandez-Nieves, "Capillary-based microfluidics—coflow, flow-focusing, electrocoflow, drops, jets, and instabilities", Small **16**, 1904344 (2020).

[107] X. Li, L. He, Y. He, H. Gu, and M. Liu, "Numerical study of droplet formation in the ordinary and modified t-junctions", Physics of Fluids **31** (2019).

Summary

Intumescent coatings form a family of specialized paints used in modern architecture for fire protection. When exposed to heat, they greatly expand through bubble generation, i.e., intumesce, and subsequently act as a thermal barrier that delays structural collapse. Current intumescence technology relies on melamine as a chemical source of gas for bubble generation (blowing agent). However, melamine's carcinogenic nature and its tendency to create uncontrolled bubbles limit the coating's effectiveness and impacts both people's health and the environment. It is therefore on the upcoming list of restricted substances. Fire protection technologies are thus in dire need of a new paradigm for bubble generation. Furthermore, a novel concept for bubble generation may prove invaluable to improve the coating's mechanical resistance and insulation properties, provided that it also allows control over the intumescence process. In this thesis, we explore the possibility of using physical means rather than chemical reactions to generate bubbles in coatings. More specifically, we aim at designing liquid precursors and exploiting controlled vaporization as a source of intumescence.

In the **introduction**, we demonstrate the intumescence of a coating, which we use to outline the problem: intumescence in a coating is a multistep process that encompasses precursor design and fabrication, controlled vaporization, and complex viscoelastic interactions upon embedding within a polymeric resin. At the heart of it all, however, lays the problem of understanding the vaporization of a single precursor.

The **second** chapter investigates the vaporization of a water droplet in an organic liquid when this droplet is subjected to a slow temperature ramp as is the case during the growth of a fire. We introduce a model utilizing a Rayleigh-Plesset-type equation to capture bubble dynamics, which includes heat transfer through the convection-diffusion equation and subsequent phase change. Our results show that the mechanism driving vaporization, specifically inertia or thermal diffusion, varies depending on the size of the droplet and

the degree of superheat.
In the **third** chapter, we conduct experiments on the vaporization of isolated water droplets immersed in oil and subjected to a gradual temperature increase. We observe a significant increase in the solubility of water in the oil phase as the droplets approach their boiling point. We quantify dissolution using a semi-empirical form of the Epstein-Plesset equation and show that applying a temperature ramp leads to the existence of a minimum droplet size below which vaporization cannot occur. Furthermore, we show that droplet vaporization is, in practice, limited by the retraction of the liquid sheet around the bubble. The model developed in the second chapter is adapted to account for these essential and asymmetric fluid dynamic processes.
In the **fourth** chapter, we coat droplets with a composite shell consisting of polylactic acid and nanoparticles. These coated droplets are exposed to a temperature ramp. We show that the shells partly shield the droplets against dissolution until the shell itself reaches its melting point. We develop a theoretical model that accounts for the temperature-dependent saturation concentration, which provides deeper insight into the dissolution process and allows for evaluating key properties of the liquids pertaining to droplet dissolution and stability. Furthermore, we show that, if nucleation is achieved, vapor bubble dynamics are similar to those of uncoated droplets.
In the **fifth** chapter, we develop a microfluidic system to create monodisperse, water-filled microcapsules. This process utilizes a 3D-printed chip whose 3D geometry is capable of generating both single and double emulsions, and of handling fluids with a broad range of wetting properties. To demonstrate its potential, we produce droplets and double emulsions consisting of curable epoxy resin with melamine, which we solidify post-production into particles and capsules. We quantify the operating range of the chip, as well as the size distributions and properties of the particles and capsules produced.
Finally, in the **conclusion**, we discuss the relevance of these findings to intumescent coatings as well as the promising future directions that this research could take.

Summary (Dutch)

Staalconstructies van moderne gebouwen moeten zijn voorzien van brandwerende of brandvertragende maatregelen. Een intumescerende, ook opzwellende, coating is een gespecialiseerde verf die als deklaag op het staal wordt gebruikt voor brandbeveiliging. De coating zet uit wanneer het aan hoge temperatuur wordt blootgesteld en fungeert zo als thermische isolatie om aantasting van de dragende constructie en daarmee instortingsgevaar te voorkomen. De huidige coatings gebruiken melamine als schuimmiddel, dat bellen vormt als het aan hitte wordt blootgesteld. Echter, deze chemische belvorming gebeurt weinig gecontroleerd wat een efficiënte werking van de coating niet ten goede komt. Bovendien vormt melamine een belasting voor het milieu en is het mogelijk kankerverwekkend. Mede vanuit de industrie is er dan ook een dringende vraag naar een beter presterend en duurzamer alternatief voor de huidige generatie brandwerende coatings.

Dit proefschrift beschrijft een uitgebreide studie naar de haalbaarheid van een nieuwe, fysische manier van belvorming in brandvertragende verf door polymere microcapsules gevuld met water toe te voegen aan de coating. Bij hoge temperatuur verdampt dan het water en vormt het bellen. De microcapsules zijn allemaal even groot en dat bevordert de controle over het verdampingsproces. Bovendien komt de resulterende uniforme belgrootteverdeling de stabiliteit van de opgezwollen coating ten goede.

We gebruiken een top-down benadering om het idee systematisch te evalueren. In het **eerste** hoofdstuk schetsen we de probleemstelling en testen we de polymeer-gecoate druppels in plaats van de traditionele melamine. De eerste testen lieten zien dat deze nieuwe methode wat betreft opzwelling minder presteerde dan de huidige producten en daarom is in eerste instantie besloten de studie te starten met een onderzoek aan de verdamping van een enkele ongecoate druppel.

In het **tweede** hoofdstuk is een model ontwikkeld om het verdampingsproces

van een enkele druppel in een verhitte vloeistof te beschrijven. Het model gebruikt een Rayleigh-Plesset-type vergelijking voor de beldynamica, met daaraan gekoppeld de convectie-diffusievergelijking om de thermodynamische faseovergang en warmteoverdracht te beschrijven. Vergeleken met het conventionele model laten deze resultaten zien dat het onderliggende mechanisme van verdamping, in het bijzonder de thermische inertie (het warmte-absorberend vermogen) of de thermische diffusie, varieert afhankelijk van de grootte van de druppel en de mate van oververhitting.

Het **derde** hoofdstuk beschrijft experimenten van de verdamping van enkele waterdruppels (nog steeds zonder coating) in olie die zijn onderworpen aan een gecontroleerde temperatuurstijging. We zien een aanzienlijke toename van de oplosbaarheid van water in de niet-mengende oliefase naarmate de druppels hun kookpunt naderen, bij een temperatuur van ca. 90^oC. Dit proces hebben we kunnen kwantificeren met behulp van een semi-empirische vorm van de Epstein-Plesset-type vergelijking. Bovendien worden de verdampende druppels in hun groei beperkt door de terugtrekking van een vlies over het oppervlak van de bel. Het model, dat in het tweede hoofdstuk is ontwikkeld, hebben we aangepast om deze beldynamica te kunnen beschrijven.

In het **vierde** hoofdstuk hebben we druppels gecoat met een composietschil bestaande uit polymelkzuur en nanodeeltjes. Deze capsules werden ook blootgesteld aan een gecontroleerde temperatuurstijging. De composietschil bleek de versnelde oplosbaarheid uit te stellen tot een punt waarbij de schil zijn smelttemperatuur van ongeveer 150 ^oC bereikte. Daarboven losten ook de capsules versneld op in de olie en gedroegen ze zich verder hetzelfde als de ongecoate druppels. Sommige capsules losten zelfs volledig op zonder een faseverandering te ondergaan. We hebben een Epstein-Plesset-type model ontwikkeld met een lineaire toename van de verzadigingsconcentratie aan het oppervlak om het oplosgedrag van zowel microdruppels als microcapsules te reproduceren. We zien dat de experimenteel gemeten beldynamica vergelijkbaar is met die van de ongecoate druppels.

In het **vijfde** hoofdstuk hebben we een proces ontwikkeld om monodisperse, met water gevulde microcapsules te creëren. Dit proces gebruikt een microfluïdische chip die enkele, alsook dubbele emulsies in dezelfde microkanalen kan genereren, voor vloeistoffen met verschillende bevochtigingseigenschappen. Druppels en de ingekapselde fasen van dubbele emulsies bestaan uit hars van epoxy met melamine, die na productie uitharden tot deeltjes en capsules. Tot slot bespreken we in het laatste hoofdstuk de relevantie van deze studies met betrekking tot intumescerende coatings en in het licht van mogelijk

toekomstige richtingen.

Acknowledgements

In this final section, I extend my gratitude to everyone who supported me throughout my PhD journey. **Michel**, your masterclass in Xi'an inspired me to pursue my PhD under your guidance. Your supervision has been invaluable and facilitated significant growth both personally and professionally. The feedback you provided on my first manuscript deepened my understanding of scientific writing. **Guillaume**, Marie-Jean introduced you as a challenging person with lots of growth opportunities, the experience indeed lived up to those expectations. While meeting your high standards has been tough, your constant support has been essential. Initially, keeping up with your quick thinking was challenging, but I adapted. The opportunity you and Michel have given me has allowed me to develop skills in modeling, simulation, and experimentation. I deeply appreciate both of you for your support.

Marie-Jean, you were the reason I chose to pursue a PhD. I deeply admire your patience and commitment to helping your students learn and grow. Your guidance during my Master's degree and your assistance in securing the PhD position at PoF has been invaluable.

Claas Willem, you have inspired me greatly since our first meeting in Xi'an and further when you assisted with my PhD application at PoF. Our brief conversation at JMBC led to what Guillaume describes as the best chapter of my PhD. I must also thank **Jieke** for the collaboration in exploring different microcapsule samples together.

My journey at PoF started during the challenging times of COVID-19, which made it quite difficult, but Ali, Benjamin, Nathan, and Dawid, you were always there for me. **Ali**, thank you for organizing all those trips, especially the one you paid for because you wanted to drive around the Netherlands. I have adored every moment we spent together, whether in Groningen, at the gym, or in the lab with Persian songs. You are not just a great colleague but also my best friend, the first person I turn to at the first sign of trouble. **Nathan**, thank you not only for your help in organizing trips but also for

being a good friend since our days in Xi'an back in 2018. Following you to PoF, sharing the office, and exploring Enschede together at the beginning made for a fantastic start. You have been there whenever I needed someone with Dutch language skills. **Benjamin**, I could easily write a chapter filled with stories about our time together. Working with you in the lab was always fun. Our shared sense of humor defined the last four years. At first, your habit of eating peanut butter sandwiches seemed strange, until I found myself doing the same later in my PhD! Your support during the crucial last three months was invaluable, helping me secure a defense date and consistently checking on my writing progress. You truly earned the role of my paranymph right up to the end. **Dawid**, our discussions ranged from cavitation meetings to extended talks about politics, world views, and your passion for guitar, all of which were deeply enriching. You have been a great friend. The meals your mom cooked, always reminding me of home, were incredibly delicious, and I am truly grateful for her kindness. All of you helped me tackle scientific challenges I could not have faced alone. This PhD would not have been possible without your support.

Ahmed, you have also been the person I turn to at the first sign of a problem; the time we spent together before your marriage, along with Taha, Bakht, Zain, and Hamza, was truly special. All those delicious meals were memorable, and the food your wife prepared later was even more delicious. I am so grateful for those moments. It was a difficult decision to choose you among others as my paranymph. Thank you for accepting.

Yogesh, you were the person to whom I came for senior advice, which has always been invaluable, whether discussing experiments or writing papers. Our discussions typically covered every topic imaginable by the end. **Charu**, I have had many opportunities to engage in deep conversations with you on a variety of topics, which has always been a pleasure, especially when discussing Chintu. **Utkarsh**, I remember our first conversation at the coffee corner late at night; you were working on your experiments, and it inspired me to also put in extra hours at the lab. **Lijun**, sharing a room with you at the European Fluid Mechanics Conference and during the PoF outing was great, especially the daal you cooked. You have always been incredibly helpful whenever I needed assistance with lab equipment.

Timothy, thank you for being an excellent collaborator on the final chapter and always supporting my ideas. It all began when you started exploring 3D printing for microfluidics, which reignited my motivation for the topic after so many failed attempts. This also includes special thanks to **Dominik** for

supervision and support throughout the project.
Jochem, I truly appreciate all the great conversations we have shared. You have been a supportive presence during the stressful times of my PhD and a fantastic colleague. Your advice has been invaluable, and I am deeply grateful for your support.
Mandeep, our discussions have been incredible, and it's nice to know I am not alone in my perspectives. Thank you for being there and sharing your insights. **Cayan**, talking with you about everything happening in our lives and sharing non-European experiences has always been a pleasure. **Minkhus**, thank you for taking my Punjabi insults, and for explaining the Urdu poetry in Nusrat's songs to me.
Special thanks to **Gert-Wim**, **Bas**, **Thomas**, **Martin**, **Dennis**, and **Joanitha** for always being there to assist. **Martin**, it was great having you around not only for assistance in the lab but also for our conversations about everything in the Netherlands.
Having French supervisors for both my master's and PhD, along with French colleagues **Pierre**, **Vincent**, **Quentin**, and **Raphael**, has been a fantastic experience. Big thumbs up to all of you for being wonderful colleagues. **Fleur**, sharing the lab with you during your master's was nice. I wish you the best of luck with your PhD, and the same goes for **Hermen** and **Rink**.
I have shared wonderful moments and conversations with so many incredible people, too many to list comprehensively here, but I want to acknowledge each one of you: **Kim**, **Sander**, **Diana**, **Maike**, **Palav**, **Edgar**, **Simon**, **Yibo**, **Yoan**, **Farzan**, **Horan**, **Daniel**, **Pim**, **Vanshu**, **Peter**, **Ellis**, **Marvin**, **Hermjan**, **Qi**, **Lingfeng**, **Subhani**, **Hadi**, **Charlotte**, **Tolga**, **Luuk**, **Duarte**, **Aleksandr**, **Chris**, **Marco**, **Youssef**, **Alexandros**, **Bingling**, **Xiaoli**, **Ayush**, **Jnandeep**, **Parshant**, **Duco**, **Udo**, **Macy**, **Yaxing**,and **Sarah**. If I have missed anyone, please forgive the oversight.
In closing, I want to extend heartfelt thanks to my family: **Papa**, my late **Mama**, **Appa**, **Ammi**, and my siblings for always being there. Without the support of Papa and Mama, I could not have reached where I am today. I am deeply grateful to my wife, **Eman**, for being such a wonderful partner. You came into my life during an incredibly tough period, and things only grew more challenging, but your patience and support have been invaluable. While I admit I may not always be the best husband, your incredible qualities as a wife help bring balance to our lives. I look forward to spending the rest of our lives together.

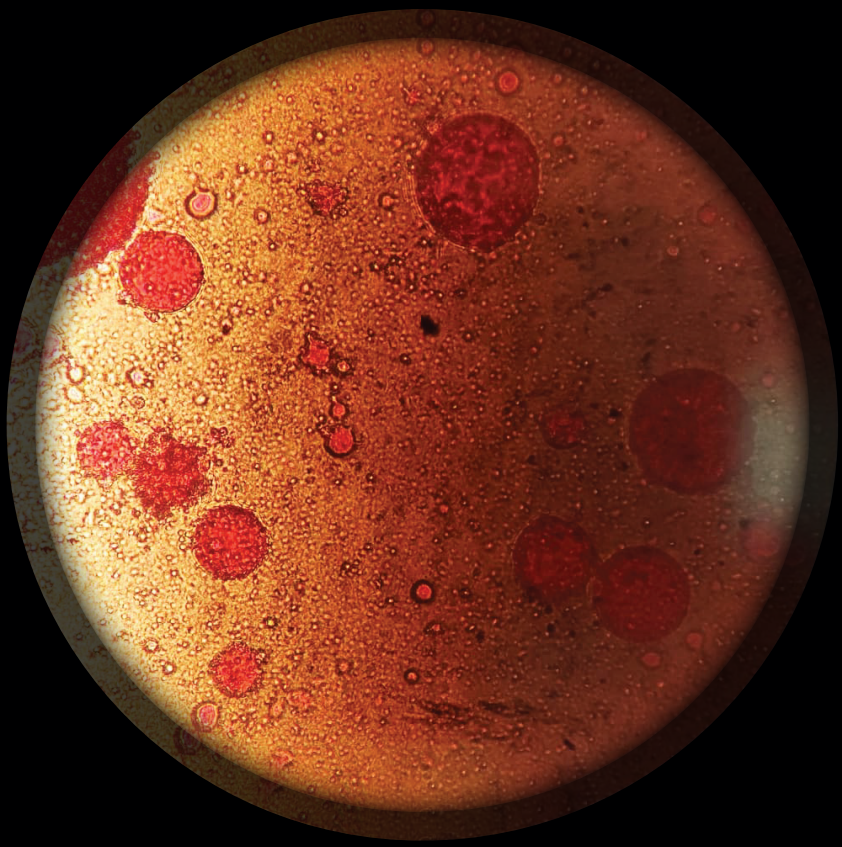

UNIVERSITY OF TWENTE.